

Development of a Primary Solidification Mode Diagram for Austenitic Stainless Steel
Weld Metals Using CALPHAD-Based Modeling

Dissertation

Presented in Partial Fulfillment of the Requirements for the Degree Doctor of Philosophy
in the Graduate School of The Ohio State University

By

Benjamin J. Sutton

Graduate Program in Materials Science and Engineering

The Ohio State University

2021

Dissertation Committee

Dr. Antonio Ramirez, Advisor

Dr. Jenifer Locke

Dr. Alan Luo

Dr. Jeffrey Sowards

Copyrighted by
Benjamin J. Sutton
2021

Abstract

The primary solidification mode of austenitic stainless steel weld metals strongly dictates solidification cracking susceptibility. Provided that primary solidification mode selection is highly dependent on chemical composition, predictive tools such as the WRC-1992 diagram are often used to assess risk and/or design around potential solidification cracking concerns. In recent years, solidification simulations are becoming more commonplace with the advent and ever-growing adoption of CALPHAD methodologies, providing an additional avenue to predict primary solidification mode in austenitic stainless steels.

In this work, high-throughput computational thermodynamic calculations have been used to develop a diagram to predict primary solidification mode for austenitic stainless steel weld metals. By simulating the stable and metastable liquidus temperatures for randomly generated austenitic stainless steel chemistries, a new set of nickel and chromium equivalency relationships have been developed that provide a sharp delineation between primary austenite and primary ferrite solidification modes under equilibrium conditions. Comparisons between legacy experimental data and computational thermodynamic calculations suggest that undercooling at the solid-liquid interface promotes metastable primary austenite solidification in stainless steel chemistries that fall near the equilibrium austenite-ferrite transition during conventional arc welding

solidification conditions. Multicomponent dendrite growth theory has also been applied to help rationalize the occurrence of metastable primary austenite solidification. Using this information, a correction scheme has been established to modify the new primary solidification mode diagram to account for dendrite growth kinetics. A series of controlled gas tungsten arc spot welds have been performed on various arc-cast alloy chemistries that fall near the austenite-ferrite transition to assist with validation of the new primary solidification mode diagram. Validation efforts highlight that the location of the metastable austenite-ferrite transition is sensitive to both alloy chemistry and solidification conditions. An overview of the computational thermodynamic simulation framework, diagram construction, and experimental validation will be provided.

While the new primary solidification mode diagram was constructed using a chemical composition range that covers many common austenitic stainless steel grades, the methodology developed here can be used to generate similar diagrams in the future and greatly reduce experimental burden. Examples where this methodology can be applied include cases where the chemical compositions and/or solidification conditions of interest differ from those explored here, or when increased resolution is needed within a narrow chemical composition range.

Dedication

This work is dedicated to my wife (Liz), my family, and friends for their constant support and encouragement.

Acknowledgments

First and foremost, I would like to thank my advisor, Dr. Antonio Ramirez. You took a gamble by bringing a 29 (almost 30) year old guy from industry into your research group and I will forever be grateful for that opportunity. I could not have asked for a better mentor. It has been a pleasure working together over the past four years and I look forward to continuing that in the future.

Next, I would like to thank my co-advisor, Dr. Jenifer Locke. My project has taken some twists and turns along the way, partly in thanks to COVID-19, and you have been supportive of me and those changes even though it meant deviating from some corrosion testing that we had planned.

I also thank Dr. Alan Luo for participating on my dissertation defense committee. Although we have not had the opportunity to work together, I hope that we can find some common research interests to explore in the future.

I thank Dr. Jeffrey Sowards for joining my dissertation defense committee as an external member. Your insights on my dissertation work have been invaluable. I have always appreciated our discussions, dating back to when we originally crossed paths when I was a “green” undergraduate research assistant and you were finishing up your PhD.

Next, I thank Dr. John Lippold for his continued support over the years. Thank you for taking the time to participate in portions of my PhD process and providing valuable advice on my research and career.

I thank the members of the Ramirez research group, past and present, for insightful discussions and comradery. I am especially appreciative Nathan Daubenmier and Braden Schwallie. It has been great working with you guys. Keep up the good work.

I owe a huge thank you to my colleagues at EPRI, especially the members of the Welding and Repair Technology Center. I wouldn't be where I am today without your support and encouragement.

I thank Dr. Damian Kotecki, Dr. John Vitek, Dr. Jeff Rodelas, Dr. Adam Hope, and Dr. Jim Rule for thought-provoking discussions related to stainless steel solidification. Your insights have been very beneficial.

Last, but not least, I thank my family. Your unwavering support has motivated me to always push forward, pursue my passions, and make myself a better person every day.

Vita

June 2011 B.S., Welding Engineering, The Ohio State University
June 2013 M.S., Welding Engineering, The Ohio State University
July 2013 to present Engineer and Technical Leader, EPRI
September 2017 to present.....Graduate Research Associate, The Ohio State University

Publications

1. Giorjao, R., B. Sutton, and A. Ramirez, New Composition Based Technique for Solidification Cracking Resistance Evaluation. *Metallurgical and Materials Transactions A: Physical Metallurgy and Materials Science*, 2021. 52(6): p. 2512-2521.
2. Zhong, W., et al., Microstructure, Hardness, and Residual Stress of the Dissimilar Metal Weldments of SA508-309L/308L-304L. *Metallurgical and Materials Transactions A: Physical Metallurgy and Materials Science*, 2021. 52(5): p. 1927-1938.
3. Li, Z., et al., Modified Microstructures in Proton Irradiated Dual Phase 308L Weldment Filler Material. *Journal of Nuclear Materials*, 2021. 548.
4. Sutton, B., et al., Heat Treatment of Alloy 718 Made by Additive Manufacturing for Oil and Gas Applications. *JOM*, 2019. 71(3): p. 1134-1143.
5. Freyer, P.D., et al. Hot Cell Pulsed Laser Welding of Neutron Irradiated Type 304 Stainless Steel with a Maximum Damage Dose of 28 DPa. in *American Society of Mechanical Engineers, PVP*. 2019.
6. Tang, W., et al. Friction Stir Welding and Preliminary Characterization of Irradiated 304 Stainless Steel. in *American Society of Mechanical Engineers, Pressure Vessels and Piping Division PVP*. 2019.

7. Chen, J., et al. Auxiliary Beam Stress Improved Laser Welding for Repair of Irradiated Light Water Reactor Components. in American Society of Mechanical Engineers, Pressure Vessels and Piping Division PVP. 2019.
8. Sutton, B., et al., Friction Stir Processing of Degraded Austenitic Stainless Steel Nuclear Fuel Dry Cask Storage System Canisters, in Minerals, Metals and Materials Series. 2017. p. 343-351.
9. Ross, K., et al., Development of Friction Stir Processing for Repair of Nuclear Dry Cask Storage System Canisters, in Minerals, Metals and Materials Series. 2017. p. 39-46.
10. Sutton, B. and D. Gandy. Assessment of Powder Metallurgy-Hot Isostatic Pressed Nozzle-to-Safe End Transition Joints. in American Society of Mechanical Engineers, Pressure Vessels and Piping Division PVP. 2017.
11. McCracken, S.L. and B. Sutton. Qualification of Temper Bead Welding by an Alternative Hardness Testing Approach. in American Society of Mechanical Engineers, Pressure Vessels and Piping Division PVP. 2015.
12. Sutton, B.J. and J.C. Lippold. Effect of Alloying Additions on the Solidification Cracking Susceptibility of High Manganese Steel Weld Metals. in Proceedings of the International Offshore and Polar Engineering Conference. 2013.
13. Alexandrov, B.T., et al. Susceptibility to Solidification Cracking in High Chromium Nickel-Base Filler Metals for Nuclear Power Applications. in ASM Proceedings of the International Conference: Trends in Welding Research. 2013.

Fields of Study

Major Field: Materials Science and Engineering

Table of Contents

Abstract.....	ii
Dedication.....	iv
Acknowledgments.....	v
Vita.....	vii
Table of Contents.....	ix
List of Tables.....	xii
List of Figures.....	xiii
Chapter 1. Introduction.....	1
Motivation.....	1
Research Objectives.....	5
Organization of Dissertation.....	6
Chapter 2. Background.....	8
Austenitic Stainless Steels.....	8
Austenitic Stainless Steel Solidification Behavior.....	9
Influence of Primary Solidification Mode on Solidification Cracking Susceptibility..	14
Equivalency Relationships.....	21
Modeling of Austenitic Stainless Steel Solidification – Solute Segregation.....	24
Modeling of Austenitic Stainless Steel Solidification – Kinetics.....	32
Calculation of Phase Diagrams (CALPHAD).....	45
Chapter 3. Development of CALPHAD-Based Equivalency Relationships for Austenitic Stainless Steel Weld Metals.....	47
Introduction.....	47
Equilibrium Assessment of WRC-1988 Database.....	49
Expansion to Randomly Generated Austenitic Stainless Steel Chemistries.....	52
Computational Framework.....	59
Scheil Simulations.....	59
Stable and Metastable Equilibria.....	62
Formulating New Equivalencies.....	64
Results and Discussion.....	65
Scheil Simulations.....	65

Stable and Metastable Equilibria	72
Comparison of Cr_{eq}/Ni_{eq}	87
Conclusions.....	92
Chapter 4. Development of a CALPHAD-Based Primary Solidification Mode Diagram for Austenitic Stainless Steel Weld Metals.....	95
Introduction.....	95
Dendrite Growth Theory.....	96
Development of a Primary Solidification Mode Diagram.....	99
Classification of Alloy Types	107
Use of the Solidification Mode Diagram	110
Conclusions.....	122
Chapter 5. Experimental Investigation of Newly Developed Primary Solidification Mode Diagram.....	124
Introduction.....	124
Experimental Procedures	125
Materials	125
Spot Welding Procedure Development.....	128
Sample Characterization	130
Thermodynamic Calculations and Dendrite Growth Simulations.....	131
Thermodynamic Calculations	131
Dendrite Growth Simulations	132
Results and Discussion	133
Solidification Front Velocity	133
Microstructure Analysis.....	134
Chemical Analysis and Measurement Uncertainty.....	142
Dendrite Growth Kinetics.....	147
Conclusions.....	151
Chapter 6. Concluding Remarks and Opportunities for Future Work	154
Summary.....	154
Future Research Opportunities	158
References.....	164
Appendix A. Certified Material Test Reports for Stainless Steel Filler Materials	171
Appendix B. Chemical Analysis Results for Experimental Ingots.....	178

Appendix C. Micrographs of Experimental Alloys 180

List of Tables

Table 1: Austenitic stainless steel concentration limits for the published WRC-1988 diagram, WRC Appendix I database, WRC Appendix II database, and Theoretical WRC database.....	55
Table 2: Parameters to construct linear boundaries for various K values for the $\Delta T_{L,2}$ and ΔT_L equivalencies	112
Table 3: Hypothetical stainless steel chemistry and standard deviation values used to perform Monte Carlo sampling for various chemical analysis test cases.....	115

List of Figures

Figure 1: WRC-1992 diagram [6].....	4
Figure 2: Phase equilibria from the Fe-Ni-Cr system; a) liquidus projection [10]; b) solidus projection [10]; c) region of three phase equilibrium at high temperature [10]; d) calculated isopleth at 70 wt.% Fe (calculated using Thermo-Calc).....	10
Figure 3: Schematic representation of solidification modes observed in austenitic stainless steel weld metals [19].....	13
Figure 4: Typical austenitic stainless steel weld metal microstructures resulting from a) A-mode solidification, b) AF-mode solidification, c) FA-mode solidification with a skeletal (vermicular) ferrite structure, d) FA-mode solidification with a lathy (lacy) ferrite structure, e) F-mode solidification [3]	14
Figure 5: Solidification crack along a solidification grain boundary in a gas tungsten arc spot weld that exhibited AF-mode solidification.....	17
Figure 6: Suutala diagram showing the relationship between composition and solidification cracking susceptibility for austenitic stainless steels [25]	19
Figure 7: Weldability diagram presented by Lienert and Lippold showing the relationship between composition, solidification mode, and solidification cracking susceptibility for austenitic stainless steel pulsed laser welds [27]	21
Figure 8: Schematic comparison of free energy changes related to homogenous, heterogeneous, and fusion welding nucleation [39]	35
Figure 9: Schematic representation of constitutional supercooling; a) the steady state composition profile at a planar solidification front; b) temperature conditions at the solidification front which promote planar growth; c) temperature conditions at the solidification front which promote breakdown of planar growth due to undercooling [54]	37
Figure 10: Steady-state dendrite tip temperature solutions for ferrite (T_{δ}^*) and austenite (T_{γ}^*) in a Fe-Ni-Cr-C austenitic stainless steel alloy showing metastable austenite growth at high growth velocities; $G=400$ °K/mm [59, 60]	40
Figure 11: a) Equilibrium liquidus temperatures (T_L) and dendrite tip temperatures (T_d) for austenite (γ) and ferrite (δ) as a function of solidification velocity; b) fractional contributions of solutal (ΔT_S) and curvature (ΔT_R) undercooling as a function of solidification velocity for both phases	44
Figure 12: a) Original solidification mode data plotted onto the WRC-1988 diagram to construct solidification mode boundaries; b) Calculated stable solid phase at the nominal liquidus temperature for each sample	51

Figure 13: Calculated stable solid phase at the nominal liquidus temperature for each alloy in the Theoretical WRC database plotted on the WRC-1988 equivalency space....	58
Figure 14: Example Δf_s calculations from the ternary Fe-Ni-Cr system.....	61
Figure 15: Example ΔT_L calculation from the ternary Fe-Ni-Cr system; a) equilibrium phase diagram of the 70 wt.% Fe isopleth from the Fe-Ni-Cr system; b) phase diagram of the same system with the stable and metastable liquidus and solidus boundaries plotted	63
Figure 16: Regression analysis parameters as a function of sample size for the randomized Δf_s data; a) regression coefficients; b) p-values; c) adjusted R^2 ; d) root mean square error	68
Figure 17: Regression analysis parameters as a function of sample size for the sorted Δf_s data; a) regression coefficients; b) p-values; c) adjusted R^2 ; d) root mean square error ..	69
Figure 18: Histogram of the regression residuals for 10%, 50%, and 100% of the Δf_s data; a) randomized sampling; b) sorted sampling	71
Figure 19: Regression analysis parameters as a function of sample size for the randomized ΔT_L data; a) regression coefficients; b) p-values; c) adjusted R^2 ; d) root mean square error	74
Figure 20: Regression analysis parameters as a function of sample size for the sorted ΔT_L data; a) regression coefficients; b) p-values; c) adjusted R^2 ; d) root mean square error ..	75
Figure 21: Partial residuals plots for the regression model that was constructed using 100% of the ΔT_L data; a) Cr; b) Ni	78
Figure 22: Histogram of the regression residuals for 10%, 50%, and 100% of the ΔT_L data; a) randomized sampling; b) sorted sampling	78
Figure 23: Regression analysis parameters as a function of sample size for the randomized ΔT_L data with squared terms for Cr and Ni; a) regression coefficients; b) p-values; c) adjusted R^2 ; d) root mean square error	81
Figure 24: Regression analysis parameters as a function of sample size for the sorted ΔT_L data with squared terms for Cr and Ni; a) regression coefficients; b) p-values; c) adjusted R^2 ; d) root mean square error.....	82
Figure 25: Partial residuals plots for the regression model that was constructed using 100% of the ΔT_L data with squared terms for Cr and Ni; a) Cr; b) Ni	83
Figure 26: Histogram of the regression residuals for 10%, 50%, and 100% of the ΔT_L data with squared terms for Cr and Ni; a) randomized sampling; b) sorted sampling	84
Figure 27: Cr_{eq}/Ni_{eq} distributions for primary austenite, mixed mode, and primary ferrite solidification using the WRC, Hammar and Svensson, Δf_s , ΔT_L , and $\Delta T_{L,2}$ equivalencies	88
Figure 28: Calculated stable solid phase at the nominal liquidus temperature for each alloy in the Theoretical WRC database; a) plotted with the ΔT_L equivalency expressions; b) plotted with the $\Delta T_{L,2}$ equivalency expressions	100
Figure 29: a) Equilibrium phase diagram predictions for the primary solidification mode of each sample in the WRC Appendix II database plotted on the WRC-1988 diagram; b) corresponding ΔT_L histogram for the full data set; c) ΔT_L histogram for samples where the equilibrium phase diagram predictions matched the experimentally observed solidification mode; d) ΔT_L histogram for samples where the equilibrium phase diagram predictions did not match the experimentally observed solidification mode	104

Figure 30: Theoretical WRC database plotted onto the $\Delta T_{L,2}$ equivalency space with data points colorized between $-13^{\circ}\text{C} \leq \Delta T_L \leq 0^{\circ}\text{C}$; the upper boundary represents $K = 0^{\circ}\text{C}$ and the lower boundary represents $K = -13^{\circ}\text{C}$	106
Figure 31: Final primary solidification mode diagram using the $\Delta T_{L,2}$ equivalency expressions	107
Figure 32: Schematic representation of austenitic stainless steel alloy classifications based on the liquidus temperatures (T_L) and dendrite tip temperatures (T_d) of austenite (γ) and ferrite (δ) as a function of solidification velocity; a) Type 1 alloys showing stable austenite growth; b) Type 2 alloy showing stable austenite growth; c) Type 3 alloy showing stable ferrite growth below a critical solidification velocity (V_c) and metastable austenite growth above V_c ; d) Type 4 alloy showing stable ferrite growth.....	110
Figure 33: Monte Carlo sampling results showing the effect of random measurement error on the position of chemical compositions projected onto the $\Delta T_{L,2}$ equivalency space; the average chemical composition sits along the boundary between (A or F) and F solidification; a) Case 1 (1x variance); b) Case 2 (2x variance); c) Case 3 (3x variance)	117
Figure 34: Chemical analysis data from laboratories that participated in an IIW round robin study to measure the chemical composition of five different stainless steel weldments plotted on the $\Delta T_{L,2}$ equivalency space; symbol shapes/colors identify each weldment; matching symbols indicate the reported chemistry values from different laboratories [91]	120
Figure 35: The effect of chemical analysis variability on Cr_{eq} and Ni_{eq} for 304 and 316 stainless steel samples ($\Delta T_{L,2}$ equivalencies); a) single laboratory testing; b) interlaboratory testing; error bars represent the 95% confidence intervals for each sample; 304 chemistry: Fe-18.65Cr-9.63Ni-0.765Mn-0.55Si-0.316Mo-0.33Cu-0.014C-0.096N (wt.%); 316 chemistry: Fe-17.48Cr-12.54Ni-1.66Mn-0.72Si-2.44Mo-0.24Cu-0.014C-0.096N (wt.%).....	121
Figure 36: Flowchart for comparing experimental and predicted solidification mode behavior.....	125
Figure 37: Targeted experimental stainless steel compositions plotted on the a) WRC-1992 diagram, and b) new primary solidification mode diagram ($\Delta T_{L,2}$ equivalencies)	127
Figure 38: a) Arc melting furnace with integrated tilt casting system; b) water-cooled Cu crucible for melting material with casting mold attachment; c) finished 25 mm dia. x 6.4 mm thick stainless steel samples.....	128
Figure 39: a) spot welding fixture and gas tungsten arc welding torch; b) welding camera positioned to monitor weld pool motion.....	129
Figure 40: GTAW spot weld solidification front velocity analysis; a) weld pool radius as a function of time; b) image of weld pool immediately after the arc was extinguished; c) image of partially solidified weld pool; d) image of fully solidified weld pool	134
Figure 41: Representative GTAW spot weld microstructure from a 304L test specimen	135
Figure 42: Sample 8L30F13 spot weld; a) plan view micrograph showing MMZ region, localized primary austenite growth along the fusion boundary, and ROI for solidification mode analysis; b) cross section view showing subsurface localized austenite growth	

along the fusion boundary and the typical columnar and equiaxed grain morphologies that were at the center of each spot weld within the MMZ	139
Figure 43: Micrographs from sample 16L30F5 that solidified as primary austenite; a) low magnification; b) high magnification.....	140
Figure 44: Micrographs from sample 16L30F10 that exhibited mixed mode solidification; a) low magnification; b) high magnification	140
Figure 45: Micrographs from sample 16L30F13 that solidified as primary ferrite; a) low magnification; b) high magnification.....	141
Figure 46: Experimentally determined solidification mode for each sample plotted using the target chemical composition data on the a) WRC-1992 diagram; and b) new primary solidification mode diagram ($\Delta T_{L,2}$ equivalencies)	141
Figure 47: Monte Carlo sampling results showing the effect of chemical analysis uncertainty propagation for each experimental composition on the a) WRC-1992 diagram; and b) new primary solidification mode diagram ($\Delta T_{L,2}$ equivalencies).....	143
Figure 48: Experimentally determined solidification mode for each sample plotted using average experimental chemical analysis data on the a) WRC-1992 diagram; and b) new primary solidification mode diagram ($\Delta T_{L,2}$ equivalencies).....	143
Figure 49: Experimentally determined solidification mode for each sample plotted using experimental chemical analysis data on the new primary solidification mode diagram with various K values ($\Delta T_{L,2}$ equivalencies).....	147
Figure 50: Dendrite growth temperature solutions and experimentally observed solidification modes for the experimental alloys	148
Figure 51: Average experimental compositions plotted on the new primary solidification mode diagram with a variable K correction for the lower growth mode transition boundary	151
Figure 52: Growth restriction factors for austenite (FCC) and ferrite (BCC) for various solutes in austenitic stainless steels.....	163
Figure 53: ER308L material test report	171
Figure 54: ER308LSi material test report.....	172
Figure 55: ER309L material test report	173
Figure 56: ER309LSi material test report.....	174
Figure 57: ER316L material test report	175
Figure 58: ER316LSi material test report.....	176
Figure 59: ER330 material test report.....	177
Figure 60:ER308L-ER330 alloys: a) 8L30A1; b) 8L30F2; c) 8L30F5; d) 8L30F10; e) 8L30F13	181
Figure 61: ER308LSi-ER330 alloys: a) 8LSi30A1; b) 8LSi30F2; c) 8LSi30F5; d) 8LSi30F10; e) 8LSi30F13	182
Figure 62: ER309L-ER330 alloys: a) 9L30A1; b) 9L30F2; c) 9L30F5; d) 9L30F10; e) 9L30F13.....	183
Figure 63: ER309LSi-ER330 alloys: a) 9LSi30A1; b) 9LSi30F2; c) 9LSi30F5; d) 9LSi30F10; e) 9LSi30F13	184
Figure 64: ER316L-ER330 alloys: a) 16L30A1; b) 16L30F2; c) 16L30F5; d) 16L30F10; e) 16L30F13.....	185

Figure 65: ER316LSi-ER330 alloys: a) 16LSi30A1; b) 16LSi30F2; c) 16LSi30F5; d)
16LSi30F10..... 186

Chapter 1. Introduction

Motivation

Austenitic stainless steels are widely used across most industrial sectors. As a testament to the widespread use of austenitic stainless steels, the International Stainless Steel Forum reported that melt shop production of stainless steel and heat resisting steel exceeded 52 Mt in 2019 [1]. Of the 52 Mt of stainless and heat resisting steels, over 50% of that production was associated with 300-series (mostly austenitic) stainless steels.

The selection of austenitic stainless steels for a given application is often driven by corrosion resistance, but factors such as high toughness at cryogenic temperatures, good oxidation resistance at elevated temperatures, and lack of a ferromagnetic response in fully austenitic grades promote their use [2]. Austenitic stainless steels are also generally considered weldable if precautions are taken to avoid common issues. Some common, and well documented, examples of weldability issues associated with austenitic stainless steels include solidification cracking, heat affected zone (HAZ) sensitization, liquation cracking (both weld metal and HAZ), and ductility dip cracking, reheat cracking (mostly in stabilized grades), and copper contamination cracking [3]. Of particular importance for this manuscript, solidification cracking is often encountered in austenitic stainless steel weld metals.

300-series austenitic stainless steel weld metals find their basis in the ternary Fe-Ni-Cr system. Within the range of typical austenitic stainless steel weld metal chemistries, a liquidus trough bisects the Fe-Ni-Cr composition space into regions where either face-centered cubic (FCC) austenite (γ) or body-centered cubic (BCC) ferrite (δ) are expected to form first during solidification (i.e. primary solidification mode). It has been well established that austenitic stainless steel weld metals which exhibit austenitic solidification are much more susceptible to solidification crack formation than those that solidify with ferrite as the primary phase.

While typical austenitic stainless steel chemistries are based on the ternary Fe-Ni-Cr system, most alloys of practical importance contain other alloying additions. The presence of alloying additions in austenitic stainless steel weld metals can drastically alter whether austenite or ferrite first form from the liquid during solidification. As such, considerable effort has been devoted to: a) establishing the effect of various alloying additions on the stability of austenite and ferrite during solidification; and b) developing engineering tools that can forecast austenite and ferrite stability for a given austenitic stainless steel weld metal.

One of the most widely adopted methods to predict aspects of austenitic stainless steel solidification is to use nickel and chromium equivalency (Ni_{eq} and Cr_{eq} , respectively) relationships. Historically, Ni_{eq} and Cr_{eq} relationships have been developed by experimentally characterizing the solidification sequence and/or room temperature ferrite content of as-solidified austenitic stainless steels. By varying the chemical composition of the austenitic stainless steels under investigation, multiple regression can be used to

generate a predictive formula to describe ferrite content or aspects of the solidification sequence as a function of chemical composition. The resulting multiple regression formula can then be rearranged to group terms that behave similarly with respect to austenite or ferrite stability. Terms from the multiple regression formula which promote austenite are grouped to form a Ni_{eq} relationship, while those that promote ferrite are grouped into a Cr_{eq} relationship. The Ni_{eq} and Cr_{eq} relationships can then be used as axes on a predictive diagram, where boundaries within the diagram are drawn to indicate certain aspects of stainless steel solidification behavior. If the chemical composition of a given austenitic stainless steel weld metal is known, the concentrations of various elements can be plugged into the Ni_{eq} and Cr_{eq} relationships to provide the x and y coordinates for a data point on the diagram. Depending on where the data point falls within the diagram in relation to the boundaries that were previously drawn, aspects of the stainless steel solidification behavior can be predicted.

One predictive diagram that is of particular importance for austenitic stainless steel weld metals was developed by the Welding Research Council (WRC) in the late 1980s and early 1990s [4-6]. The WRC-1992 diagram is the most recent version of the WRC diagram and is presented in Figure 1. The WRC-1992 diagram contains two sets of boundaries that are used to predict the room temperature ferrite content and solidification mode of stainless steel weld metals within the austenitic, duplex, and ferritic composition space of commercially available alloys. Ferrite content is predicted via a series of linear ferrite number (FN) lines on the diagram, where FN is a quantity that is based on the ferromagnetic response of ferrite and provides an indication for the amount of ferrite in the

microstructure. The FN scale was originally developed to overcome experimental variability associated with metallographic determination of ferrite percentage [7]. In addition to the iso-FN lines, the WRC-1992 diagram includes linear boundaries that separate the A, AF, FA, and F solidification modes. A and AF solidification modes describe primary austenite solidification and primary austenite with eutectic ferrite solidification, respectively. FA and F solidification modes describe primary ferrite with eutectic/peritectic austenite and primary ferrite solidification, respectively. Therefore, the active solidification mode and FN can be predicted for a stainless steel weld metal composition by calculating Cr_{eq} and Ni_{eq} .

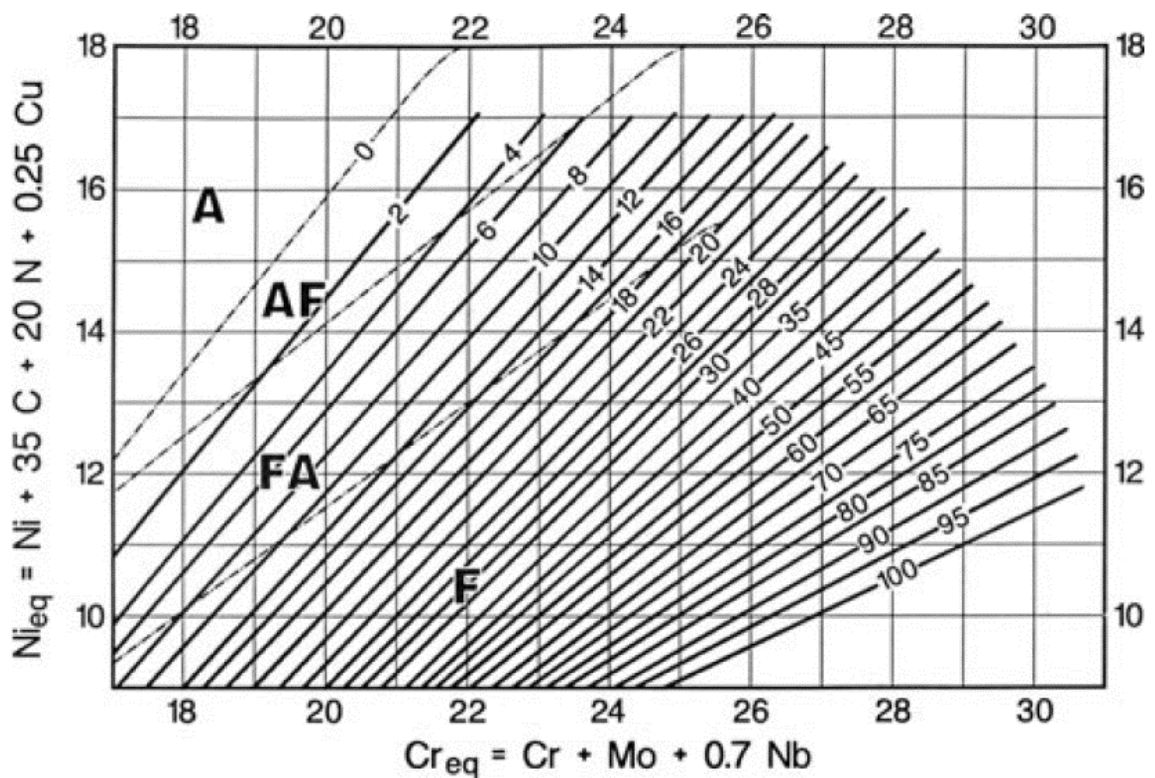


Figure 1: WRC-1992 diagram [6]

More recently, the ever-growing adoption of CALculation of PHase Diagram (CALPHAD) methodologies has enabled researchers to simulate, among other things, phase stability during the solidification process. The CALPHAD approach utilizes computational methods to model the thermodynamic properties of various phases within a system [8, 9]. Most often, this is achieved by developing model descriptions of the Gibbs free energy for various phases as functions of temperature, pressure, and chemical composition. These Gibbs free energy models can then be used to construct phase diagrams and compute phase equilibria. Using CALPHAD-based calculations, information such as the equilibrium solidification path, the non-equilibrium solidification path, solute segregation profiles, and phase fractions at various temperatures can readily be modeled for complex multicomponent systems. The application of CALPHAD-based tools to simulate aspects of stainless steel solidification is becoming more prevalent. There has not been, however, a comprehensive investigation on the use of CALPHAD calculations to determine the primary solidification mode of austenitic stainless steels. As such, this work seeks to explore the use of CALPHAD calculations to determine the primary solidification mode of austenitic stainless steel weld metals. The following research objectives will be explored.

Research Objectives

1. Compare legacy experimental data and CALPHAD solidification mode calculations. This includes developing high-throughput simulation strategies and exploring discrepancies between legacy experimental primary solidification mode

data and CALPHAD calculations. The WRC-1992 diagram will be the focus of this effort because it is the most used diagram in the literature today.

2. Create CALPHAD-based composition equivalency relationships and a primary solidification mode diagram for austenitic stainless steel weld metals.
3. Develop a high-throughput CALPHAD methodology for generating similar primary solidification mode diagrams in the future. For example, three scenarios where this may be applicable include when: a) the chemical compositions of stainless steels differ significantly from those explored here; b) increased resolution is needed within a narrow chemical composition window; c) solidification conditions (i.e., growth rate and temperature gradient) differ significantly from those seen during conventional fusion welding applications.
4. Discuss potential sources of error and how they can influence the use of a predictive solidification mode diagram and/or CALPHAD calculations.

Organization of Dissertation

This manuscript aims to address the described research objectives through a combination of CALPHAD-based modeling and controlled solidification experiments.

The content is broken into the following sections:

- Chapter 2 presents relevant background information related to stainless steel solidification, predictive tools to forecast primary solidification mode, modeling of stainless steel weld metal solidification, and CALPHAD
- Chapter 3 presents potential CALPHAD-based simulation and analysis strategies to develop composition equivalency relationships for austenitic stainless steel weld

metals; this effort includes comparing legacy experimentally derived relationships with new relationships that have been developed using a CALPHAD-based approach

- Chapter 4 addresses the construction and use of an adjustable CALPHAD-based primary solidification mode diagram for austenitic stainless steel weld metals that is connected to dendrite growth theory; this includes considerations for chemical analysis uncertainty and its effect on such a diagram; a new classification scheme for austenitic stainless steel weld metals is also presented
- Chapter 5 covers an experimental assessment of the diagram that was developed in Chapter 4 using controlled gas tungsten arc spot welding experiments on stainless steel weld metal mixtures that span the primary austenite / primary ferrite transition; dendrite growth model calculations were also performed to supplement the experimental investigation
- Chapter 6 will review conclusions from this work and provide perspectives on future areas of research

Chapter 2. Background

Austenitic Stainless Steels

Austenitic stainless steels are widely used across most industrial sectors. Most often, austenitic stainless steels are selected for a given application due to their good corrosion resistance in many service environments. The corrosion resistance of stainless steel alloys originates from the formation of a passive Cr-rich oxide film which forms on the surface and protects the underlying material. The passive Cr-rich oxide film can form on the surface of steels when Cr concentrations exceed approximately 11 wt. %. While Cr is added to promote corrosion resistance, austenite-stabilizing elements such as Ni, Mn, and N are added to promote an austenitic microstructure across a wide temperature range. The AISI 300 series of austenitic stainless steels are the most common and are based on the Fe-Ni-Cr system, with typical Ni concentrations ranging from 8-20 wt.% and Cr concentrations ranging from 16-25 wt.% [3]. Other alloying elements such as C, Si, Mo, Ti, and Nb are frequently added to achieve a balance between phase stability, corrosion resistance, mechanical performance, and manufacturability.

Welding is often required during the fabrication of stainless steel components. As such, the welding metallurgy and weldability of stainless steels has received considerable attention over the past 70+ years. Regarding the welding metallurgy and weldability of

austenitic stainless steels, two of the most important, and intricately related, topics include microstructure evolution during solidification and solidification cracking susceptibility.

Austenitic Stainless Steel Solidification Behavior

Provided that the majority of austenitic stainless steels are based on the ternary Fe-Ni-Cr system, considering the Fe-Ni-Cr equilibrium phase diagram serves as a useful starting point to understand solidification behavior. Figure 2 presents the equilibrium liquidus projection, solidus projection, and region of three phase equilibrium for the Fe-Ni-Cr system as presented by Hillert [10]. As can be seen, the liquidus surfaces for γ -austenite and δ -ferrite converge to form a monovariant line that begins in the Fe-rich corner of the ternary system and nearly splits the diagram in half as it terminates near 50 wt.% Ni-50 wt.% Cr. The monovariant line originates from the peritectic reaction in the Fe-rich corner of the Fe-Ni system and terminates at the eutectic reaction in the Ni-Cr system. As such, solidification sequences which reach the monovariant line are often termed peritectic/eutectic because the expected nature of the given reaction is composition dependent within the Fe-Ni-Cr system. An isopleth from the Fe-Ni-Cr system at 70 wt.% Fe is also presented in Figure 2. The 70 wt.% Fe isopleth was selected for presentation as this vertical section of the equilibrium Fe-Ni-Cr diagram is close in composition to many of the common 300 series austenitic stainless steel grades. As can be seen in Figure 2, compositions with a low Cr/Ni ratio should favor austenite solidification, while compositions with a high Cr/Ni ratio should favor ferrite solidification.

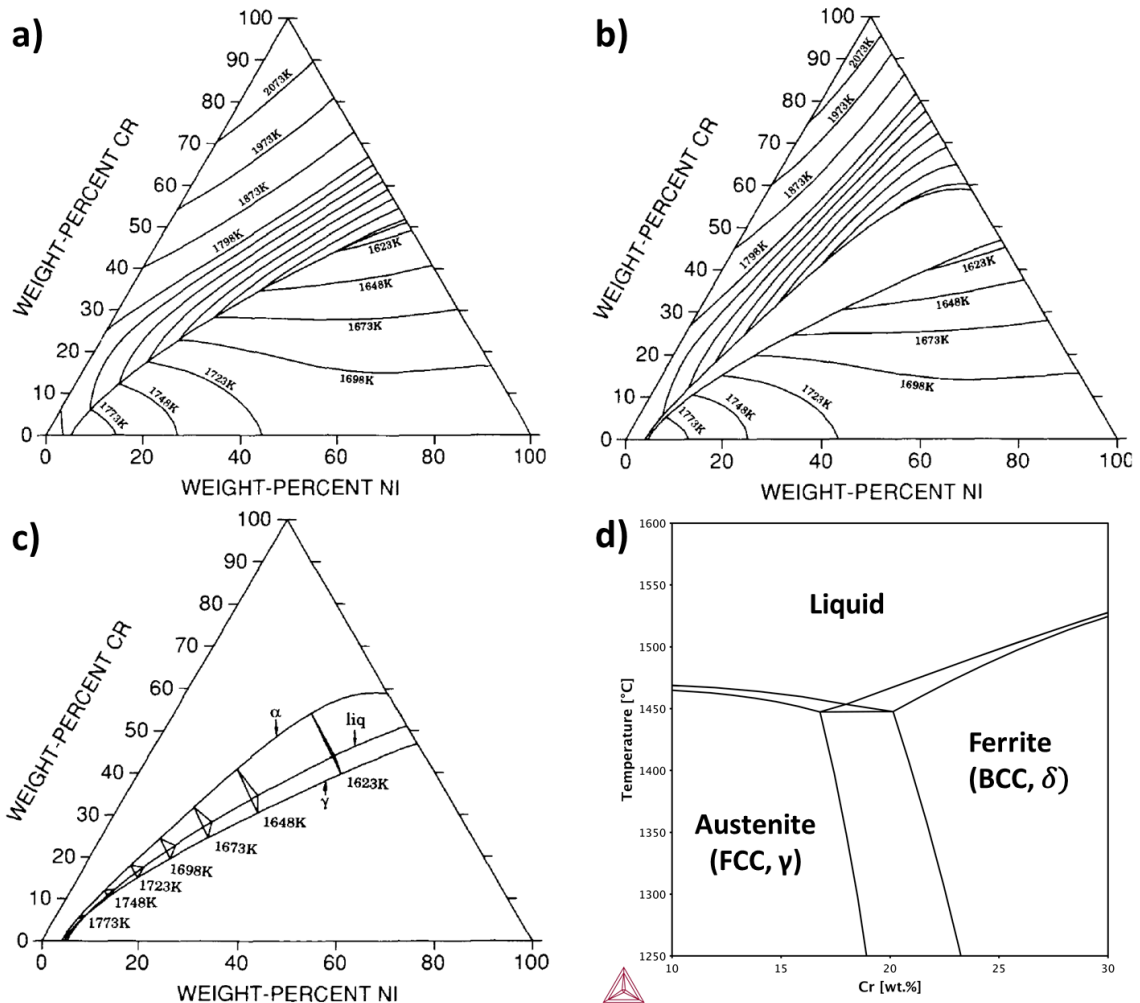


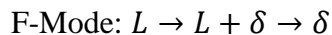
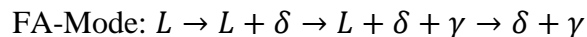
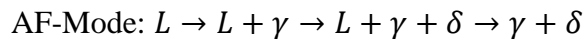
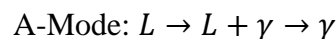
Figure 2: Phase equilibria from the Fe-Ni-Cr system; a) liquidus projection [10]; b) solidus projection [10]; c) region of three phase equilibrium at high temperature [10]; d) calculated isopleth at 70 wt.% Fe (calculated using Thermo-Calc)

Austenitic stainless steel weld metal microstructures are highly dependent on chemical composition and the solidification conditions (growth velocity, temperature gradient, and cooling rate) experienced during welding [11-15]. Shifts in the concentrations of ferrite stabilizing elements (such as Cr, Mo, Si, Nb, Ti) and austenite stabilizing elements (such as Ni, Mn, C, N, Cu) can cause significant changes to the weld metal

microstructure, resulting in microstructures that range from fully austenitic to a duplex austenitic/ferritic mixture.

Additionally, the cooling rate experienced during solidification and subsequent cooling can influence solute segregation and solid-state transformations which may occur [13, 15-17]. Cooling rates considered here will be restricted to those which are typical during conventional arc welding processes and can range from $10\text{-}10^3$ °C/s [13].

Austenitic stainless steel weld metal microstructures are generally classified by one of four modes that describe the solidification sequence and subsequent solid-state phase transformations from which they originate [3, 11]. Namely, solidification modes can be classified as austenitic (A), austenitic-ferritic (AF), ferritic-austenitic (FA), or ferritic (F). A- and AF-mode microstructures originate from primary austenite solidification, while FA- and F-mode microstructures are associated with primary ferrite solidification. Note that these four solidification modes are the typical classifications that are used to describe the weld metal microstructures that occur during conventional fusion welding conditions. The solidification reaction sequences involving liquid (L), austenite (γ), and ferrite (δ) for each solidification mode are as follows:



Deviations from this classification scheme can occur during high energy density welding processes where solidification rates can be quite high [13, 14, 18].

A-mode microstructures are those which form from fully austenitic solidification and contain no residual ferrite. AF-mode microstructures are formed when solidification initiates as austenite but ferrite forms at the end of solidification along cell and dendrite boundaries due to a eutectic reaction. The ferrite which forms at the end of AF-mode solidification is generally quite stable because it is enriched in ferrite-stabilizing elements which have segregated to the liquid along solidification grain and subgrain boundaries. FA-mode microstructures are formed when solidification initiates as ferrite and austenite forms at the end of solidification due to a peritectic-eutectic reaction. Further sub-solidus cooling of the FA microstructure results in ferrite instability, causing the ferrite to transform into austenite through a solid-state reaction at the ferrite-austenite interface. The resulting FA microstructure will contain some balance of austenite and remnant ferrite which did not transform during cooling. FA microstructures are generally subdivided based on the morphology of the remnant ferrite and can be classified as either skeletal (vermicular) or lathy (lacy). F-mode solidification microstructures are those which are fully ferritic at the end of solidification and partially transform to austenite in the solid-state during cooling. For primary ferrite solidification modes (FA and F), the residual ferrite content in the room temperature microstructure is dependent on the cooling rate of the weld since the solid-state ferrite-to-austenite phase transformation is diffusion controlled. Each of these modes presents a unique combination of solute segregation and microstructure morphology that can be sensitive to weld metal chemistry, solidification conditions, and cooling conditions. Schematic examples of the microstructure evolution of various solidification modes as

presented by Brooks can be found in Figure 3 [19]. Example weld metal microstructures arising from each solidification mode can be found in Figure 4.

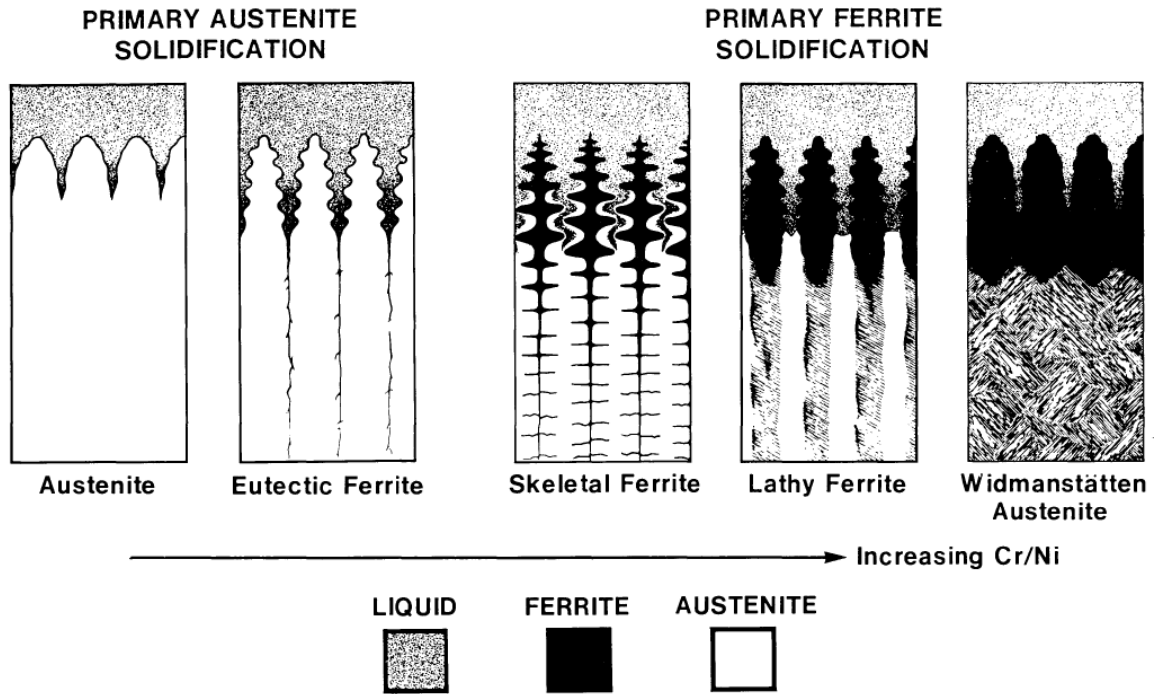


Figure 3: Schematic representation of solidification modes observed in austenitic stainless steel weld metals [19]

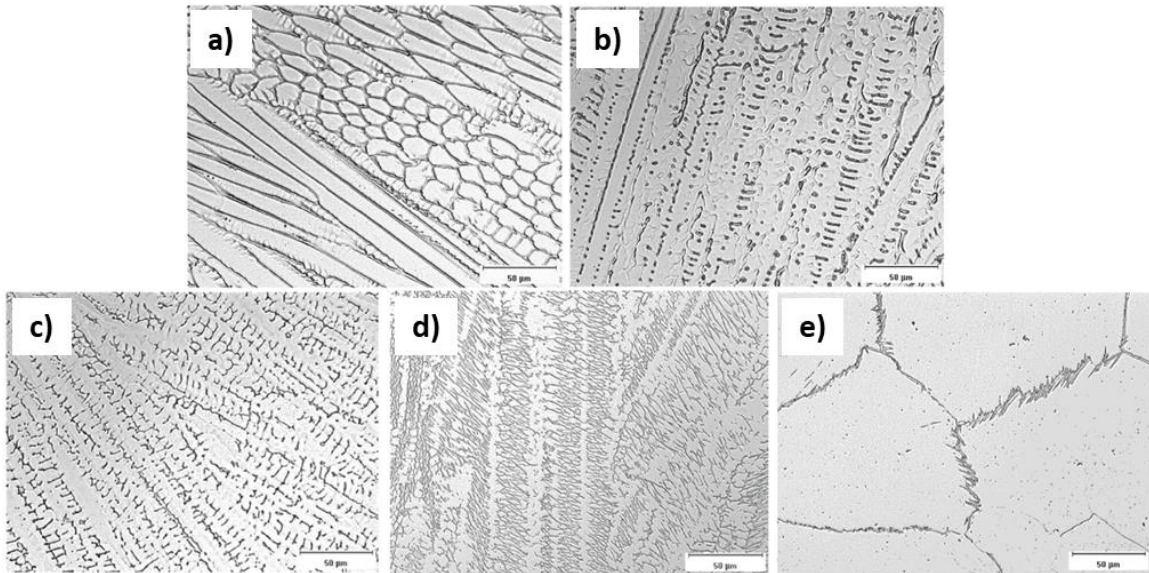


Figure 4: Typical austenitic stainless steel weld metal microstructures resulting from a) A-mode solidification, b) AF-mode solidification, c) FA-mode solidification with a skeletal (vermicular) ferrite structure, d) FA-mode solidification with a lathy (lacy) ferrite structure, e) F-mode solidification [3]

Influence of Primary Solidification Mode on Solidification Cracking Susceptibility

Solidification cracking is a phenomenon that occurs along solidification grain and/or subgrain boundaries in weld deposits (although the phenomenon is not unique to welding). During solidification of a welded alloy, a semisolid region commonly referred to as the mushy zone forms behind the solidification front. The mushy zone extends from the tip of dendrites or cells in contact with the fully liquid weld pool to the base of solidifying grains where solidification is complete. Within this semisolid region, solidification cracks form when intergranular liquid films present at the terminal stages of

solidification rupture due to thermal contraction and solidification shrinkage. For example, Nagira et.al. recently performed in-situ synchrotron imaging studies to observe centerline solidification cracking in P-doped 310S and 316L stainless steel gas tungsten arc welds [20]. It was found that the solidification crack tip velocity propagated at a solid fraction ranging from approximately 0.7 to 0.9 along interdendritic liquid films where segregation locally depressed the solidus temperature.

The circumstances which lead to solidification crack formation can be mechanical or metallurgical in character [21-23]. Mechanical factors include the extent of restraint and thermal contraction that cause strain to accumulate across the solidifying grain network. Metallurgical factors are related to the alloy chemistry and include factors such as the crystal structure of the solidifying grains, the amount and distribution of liquid along the solidification boundaries, the solidification temperature interval, viscosity of the liquid, and surface tension. Note that many of the factors involved with solidification crack formation can be sensitive to the temperature distribution and heat dissipation within and around the mushy zone.

Regarding austenitic stainless steel weld metal solidification, it has been well established that primary austenite solidification is much more prone to solidification crack formation when compared to primary ferrite solidification [24, 25]. Solidification cracking in austenitic stainless steel weld metals is most typically associated with the segregation of impurity elements (mainly S and P) along solidification grain boundaries. Impurity elements strongly partition to the liquid during solidification and form low melting point liquid films. These liquid films can then rupture at the later stages of solidification. This

cracking behavior readily occurs along austenite-austenite solidification boundaries that evolve during primary austenite solidification, whereas the nature of primary ferrite solidification (particularly FA-mode) offers much more resistance to solidification crack formation. As summarized by Brooks, the two primary beneficial effects of primary ferrite solidification include: a) less grain boundary liquid wetting along ferrite-ferrite and ferrite-austenite boundaries compared to austenite-austenite boundaries; and b) the inherent grain boundary tortuosity associated with FA-mode solidification that helps to resist solidification crack propagation [19]. Less pronounced effects include a higher solubility for impurity elements within ferrite and less solute partitioning during primary ferrite solidification. As a result of these factors, a drastic reduction in solidification cracking susceptibility can be realized by shifting from primary austenite to primary ferrite solidification. An example of a solidification crack that formed in a gas tungsten arc spot weld of an austenitic stainless steel which exhibited primary austenite (AF-mode) solidification can be found in Figure 5. The solidification crack extends along the relatively straight interdendritic region between the primary austenite grains where very little ferrite is present.

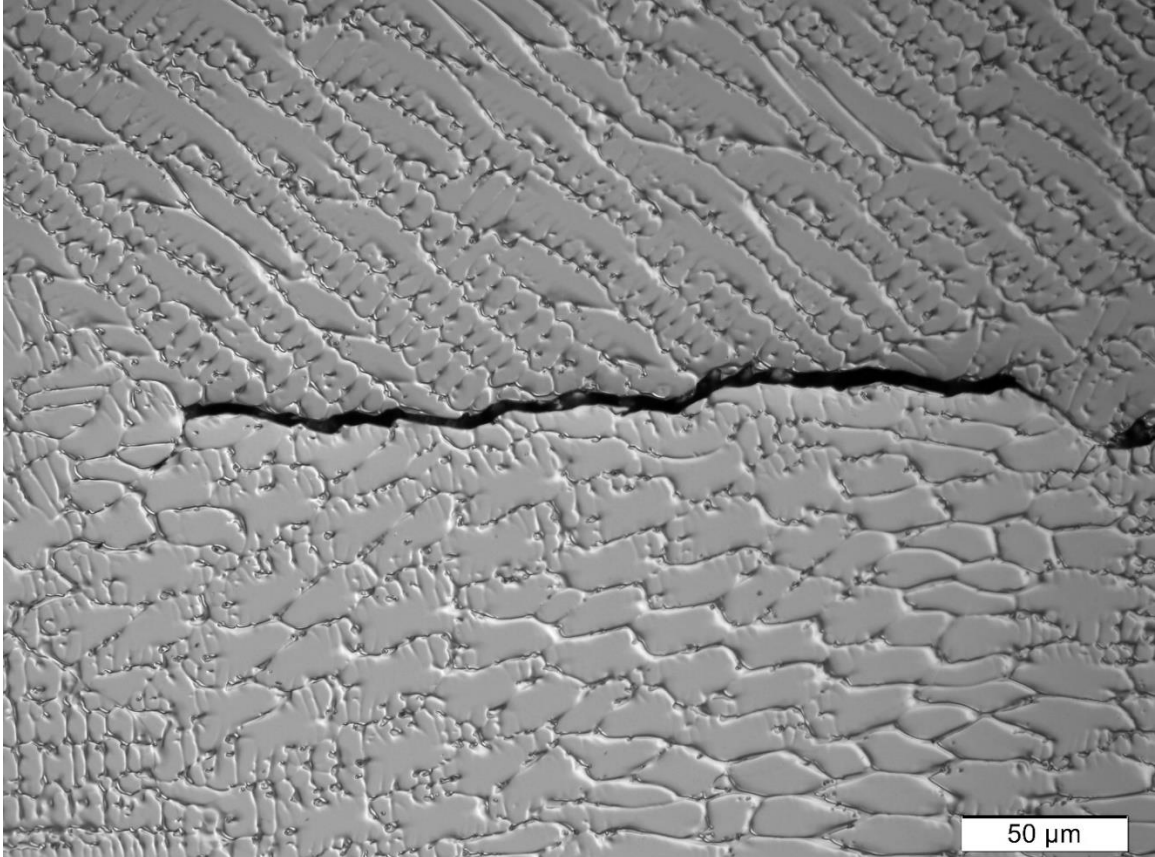


Figure 5: Solidification crack along a solidification grain boundary in a gas tungsten arc spot weld that exhibited AF-mode solidification

One of the most well-known presentations of the beneficial effect of primary ferrite solidification with respect to solidification cracking susceptibility was presented by Kujanpaa et.al. in 1979 [25]. Their diagram, commonly referred to as the Suutala diagram, is presented in Figure 6. The Suutala diagram presents an aggregation of solidification cracking test data for various stainless steel weld metals as a function of chemical composition for conventional fusion welding processes. The horizontal axis represents the relative stability of ferrite during the weld metal solidification sequence due to alloying additions (in terms of Cr_{eq}/Ni_{eq} using the equivalencies of Schaeffler [26]), and the vertical

axis represents the concentration of impurity elements in the weld metal. Each data point on the Suutala diagram represents a single weld metal composition and is shaded based on its solidification cracking susceptibility. There are two primary features on the Suutala diagram that are noteworthy. First, a fairly sharp transition in solidification cracking susceptibility is observed at a C_{req}/Ni_{eq} of approximately 1.49. This abrupt change in solidification cracking susceptibility is associated with the primary solidification mode of the stainless steel compositions that were analyzed. Most of the data points with $C_{req}/Ni_{eq} < 1.49$ exhibited primary austenite solidification and most of the data points with $C_{req}/Ni_{eq} > 1.49$ exhibited primary ferrite solidification. Secondly, the Suutala diagram shows that solidification cracking susceptibility decreases for primary austenite solidification if impurity concentrations are kept sufficiently low.

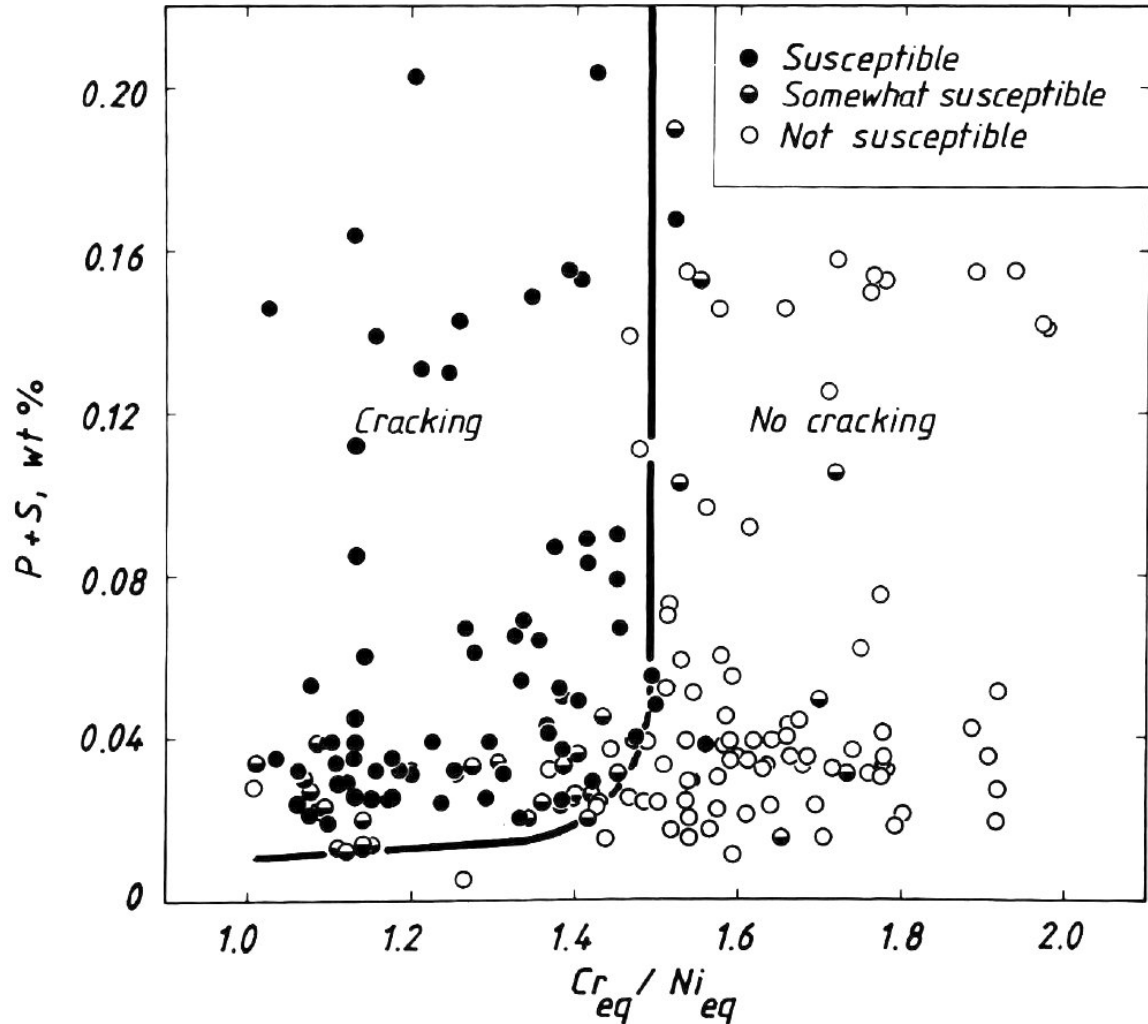


Figure 6: Suutala diagram showing the relationship between composition and solidification cracking susceptibility for austenitic stainless steels [25]

Similar to the Suutala diagram, Lienert and Lippold presented a weldability diagram for austenitic stainless steel pulsed laser welds using a $\text{Cr}_{eq}/\text{Ni}_{eq}-(P+S)$ composition space [27]. Note that the equivalency relationships differ slightly between the two diagrams as Lienert and Lippold used the so-called Hammar & Svensson equivalencies as opposed to the Schaeffler equivalencies that were used in the original Suutala diagram

[26, 28, 29]. A version of the Suutala diagram was presented by Kujanpaa and Moisio in 1983 that used the same equivalency relationships that were later used by Lienert and Lippold [30]. The Lienert and Lippold weldability diagram is presented in Figure 7. As can be seen, the general shape of the Suutala and Lienert/Lippold diagrams are quite similar, where regions separating solidification cracking susceptibility can clearly be seen. Two key differences exist between the Suutala diagram and Lienert diagram. First, rather than a single boundary that separates solidification cracking susceptibility as a function of Cr_{eq}/Ni_{eq} , two separate vertical boundaries are presented. The vertical boundaries bracket compositions which separate austenitic solidification (high cracking susceptibility), dual (commonly called mixed mode) and ferritic solidification (variable cracking susceptibility), and ferritic solidification (low cracking susceptibility). Additionally, the vertical boundary which separates fully austenitic solidification from other solidification modes is shifted to a higher Cr_{eq}/Ni_{eq} value than was defined in the Suutala diagram. While the edge of fully austenitic solidification was defined at $Cr_{eq}/Ni_{eq}=1.49$ in the Suutala diagram, the Lienert weldability diagram presents the boundary at a $Cr_{eq}/Ni_{eq}=1.59$. The position of the primary austenite solidification boundary is attributed to undercooling at the solidification front, where stainless steel weld metals that solidify as primary ferrite under conventional welding conditions can solidify as primary austenite when the solidification front velocity increases [12, 18].

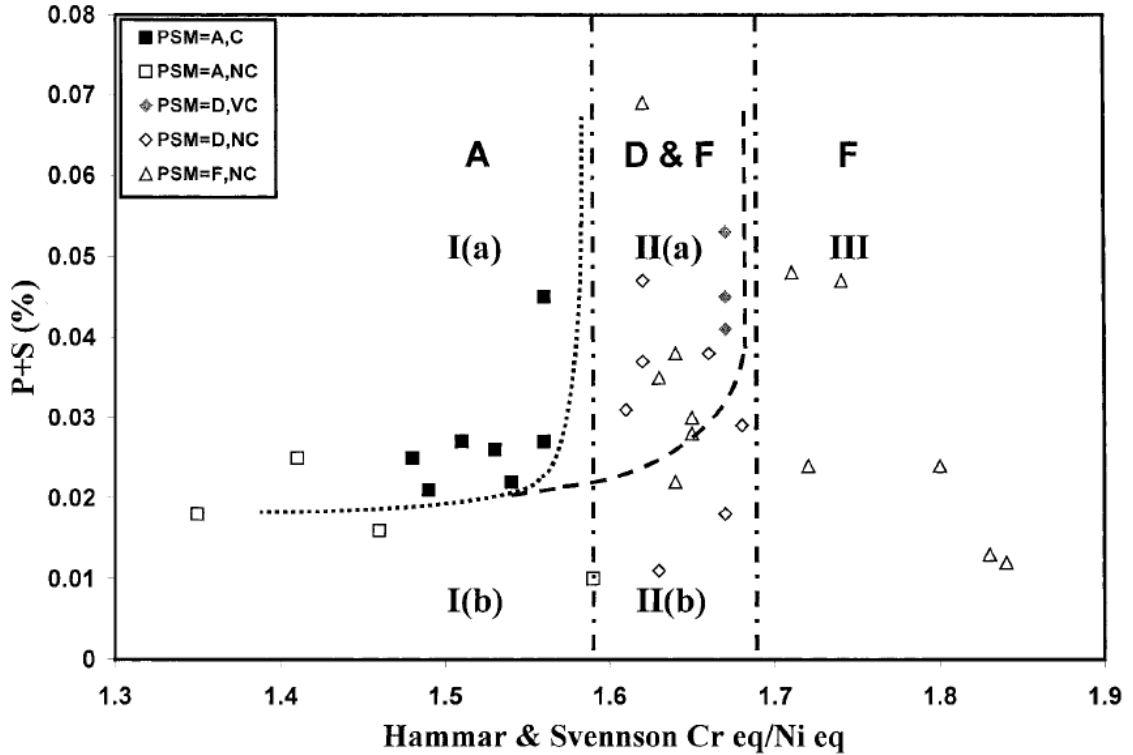


Figure 7: Weldability diagram presented by Lienert and Lippold showing the relationship between composition, solidification mode, and solidification cracking susceptibility for austenitic stainless steel pulsed laser welds [27]

Equivalency Relationships

As demonstrated in the previous section, the concept of equivalency relationships provides an avenue to reduce multicomponent alloy chemistries down to a more usable form to forecast aspects of stainless steel solidification. Their utility arises from the fact that chemical composition plays such a dominant role in determining the solidification behavior of austenitic stainless steels. Equivalency relationships are empirically derived (generally linear) expressions which group elements by their tendency to stabilize either

austenite or ferrite in the microstructure. Given that Ni is a primary alloying addition in austenitic stainless steels and promotes the formation of austenite in the microstructure, elements which stabilize austenite are grouped into a Ni equivalency (Ni_{eq}) equation. Similarly, ferrite-stabilizing elements are grouped into a Cr equivalency (Cr_{eq}) equation. Coefficients for each chemical element in the Cr_{eq} and Ni_{eq} equations then indicate the relative potency for stabilizing austenite or ferrite. Knowing the chemical composition of a given material, the concentration of each element (in wt.%) can be multiplied by its respective coefficient within the equivalency relationships. Comprehensive summaries of various Cr_{eq} and Ni_{eq} relationships that are relevant to austenitic stainless steel weld metal solidification can be found in the works of Olson and Bermejo [31, 32].

The concept of equivalency relationships for stainless steels is quite mature and dates to the early 1900s. As such, there are numerous versions of Cr_{eq} and Ni_{eq} formulas that have evolved over time. These equations have historically been developed using two data types. The first data type involves assessing the room temperature ferrite content of stainless steels after solidification. Ferrite characterization is typically achieved by magnetic response measurements or metallographic analysis to provide values in terms of volume% ferrite or ferrite number (FN) [32]. Once the ferrite content is characterized for a series of austenitic stainless steel solidification structures with varying chemical compositions, a predictive equation that relates ferrite content to stainless steel chemistry can be developed using multiple regression [4, 6]. An example of a predictive multiple regression equation that relates FN to the chemical composition of austenitic stainless steel weld metals was published by Siewert et.al. [4]. Similarly, the second data type involves

characterizing some characteristic parameter that relates to the solidification sequence of stainless steels. Hammar and Svensson used this approach by characterizing the solidification mode and solidification temperature interval of a series of austenitic stainless steels during furnace solidification experiments [29]. The measured solidification temperature interval was then used as the dependent variable in their multiple regression equation to relate the solidification mode to chemical composition. Once a multiple regression equation is developed, covariates and their coefficients which behave similarly are grouped together to define the Cr_{eq} and Ni_{eq} relationships. The general process for developing such relationships is presented below.

A generic multiple regression model can be written as [33]:

$$Y_i = b_0 + b_1X_{1i} + b_2X_{2i} + \dots + e_i \quad (i = 1, \dots, n)$$

where Y is the dependent response variable, (X_1, X_2, \dots) are the covariates, b_0 is a constant, (b_1, b_2, \dots) are partial coefficients, and e is an error term. To determine estimates for the unknowns in the regression equation, an estimated regression model can then be written as:

$$Y_i = \hat{Y}_i + \hat{e}_i \quad (i = 1, \dots, n)$$

$$Y_i = \hat{b}_0 + \hat{b}_1X_{1i} + \hat{b}_2X_{2i} + \dots + \hat{e}_i \quad (i = 1, \dots, n)$$

Values for the estimated partial coefficients $(\hat{b}_0, \hat{b}_1, \hat{b}_2, \dots)$ can then be determined by minimizing the residual sum of squares (RSS):

$$RSS = \sum_{i=1}^n \hat{e}_i^2 = \sum_{i=1}^n (Y_i - \hat{Y}_i)^2 = \sum_{i=1}^n (Y_i - \hat{b}_0 + \hat{b}_1X_{1i} + \hat{b}_2X_{2i} + \dots)^2$$

Using a nonspecific example of FN as a linear function of stainless steel chemistry, the final regression equation will have the form:

$$FN = b_0 + b_{Cr}(Cr_{eq}) + b_{Ni}(Ni_{eq})$$

where the Cr_{eq} and Ni_{eq} terms represent the linear combinations of estimated coefficient and covariate (concentration of a given element in this case) pairs that share the same sign as Cr and Ni, respectively. Multiple regression formulas that are generated using a characteristic parameter to describe the solidification mode will have the same general form.

Modeling of Austenitic Stainless Steel Solidification – Solute Segregation

Modeling of austenitic stainless steel weld metal solidification has been performed using a variety of methods in the literature. The models and methods considered in this section will be restricted to those which predict phase evolution on a microscopic scale during solidification. Considering solidification models on the microscopic scale are necessary to describe solute redistribution during the solidification process, which is intimately tied to phase evolution. Each of the models presented below assume that the solid/liquid interface is planar and that local interfacial equilibrium is maintained.

The most basic type of solidification model considers equilibrium solidification. In this case, solute diffusion is complete in both the solid and liquid phases throughout the solidification process. This type of model can simply be interpreted using available equilibrium phase diagrams for binary or ternary systems. Calculations for

multicomponent alloys can be considered through the use of computational thermodynamics and the CALPHAD method [9]. The utility of equilibrium solidification calculations is often reduced for weld metal solidification when considering that cooling rates are not sufficiently slow enough to prevent solute partitioning in the solid and liquid phases.

Assuming complete solute mixing in the liquid and no solid-state diffusion gives an extreme case of solute segregation during solidification. This methodology was refined by Scheil in the 1940s to describe non-equilibrium solidification [34]. Using this approach, the liquid continuously enriches in elements which tend to segregate away from the solid during solidification until a eutectic reaction is reached. The propensity and direction for an element to segregate can be defined by its solidification partition coefficient (k), where k is simply the ratio of the concentration in the liquid to the concentration in the solid for an element at a given temperature and is generally treated as constant. Elements with partition coefficients less than one naturally segregate to the liquid as solidification progresses, and the intensity of segregation increases as k approaches zero. The Scheil equation was originally developed for binary alloy systems and its extension to higher order systems requires special treatment [35].

The extension of Scheil solidification conditions to multicomponent alloys can be realized using the CALPHAD method [9]. The Scheil calculation scheme using the CALPHAD method is performed by iteratively calculating the equilibrium solid and liquid compositions at the solid-liquid interface, mole fraction of solid phases formed, and the resulting liquidus temperature of the segregated liquid across small temperature steps

through the solidification temperature range. Scheil simulations tend to overestimate solute segregation profiles as solidification continues until either a preset solid fraction or terminal invariant reaction is reached by the simulation. An example of such behavior was presented by Chen for low alloy steels where multicomponent Scheil simulations predicted the formation of several minor phases at the end of solidification that were not experimentally observed [36].

Researchers often compensate for overpredictions in the Scheil approach by assuming that solidification in real welds closely matches Scheil models at a solid fraction of less than one. For example, Kadoi recently assumed that terminal solidification was achieved at 0.95 fraction solid in Scheil simulations of 304L and 347 stainless steel base metals welded with 310 stainless steel, Invar, and various Ni-based filler materials [37]. It was found that the simulated solidification temperature range (STR) scaled reasonably well with the brittle temperature range (BTR) during solidification. Ueda recently used a similar approach to study the influence of Nb, Ti, and Zr additions on the solidification cracking susceptibility of fully austenitic Fe-24Cr-26Ni (wt.%) stainless steel [38]. Like Kadoi, Ueda used Scheil solidification simulations terminated at 0.95 fraction solid to evaluate STR and compare the results back to the BTR.

The solidification behavior of multicomponent alloy fusion welds falls somewhere between the bounding cases presented by equilibrium and Scheil models. Most notably, the treatment of solid-state diffusion results in model inaccuracies in both cases. Solid-state diffusion is generally neither complete (equilibrium assumption) nor negligible (Scheil assumption) for all solutes during solidification [39]. This is particularly true when

considering the diffusivities of substitutional solutes versus those of interstitial solutes. For example, the diffusion coefficients for Cr, Ni, and C have been calculated using the preexponential factors and activation energies recently presented by Ogura for austenitic stainless steel solidification simulations [40]. Near the solidus (~ 1400 °C for austenitic stainless steels), the respective diffusion coefficients (D_i^δ in units of m^2/s) for each element (i) in ferrite (δ) were: $D_{Cr}^\delta = 2 \times 10^{-12}$, $D_{Ni}^\delta = 6 \times 10^{-13}$, $D_C^\delta = 5 \times 10^{-10}$. The diffusivities of substitutional solutes (Cr and Ni) are two to three orders of magnitude lower than interstitial C. Considering simple $(Dt)^{1/2}$ calculations to estimate the diffusion distance of the solutes reveals that interstitials would diffuse 15-30 times further than substitutional solutes for a given time increment (t). Therefore, it is unreasonable to assume that interstitial solutes will behave similarly to substitutional solutes with respect to solid-state diffusion during fusion weld solidification.

Various researchers have developed models to account for solid-state diffusion while still assuming complete solute mixing in the liquid during the solidification process. The Brody-Flemings and Clyne-Kurz models have been two of the most popular and widely implemented in weld metal solidification literature [41, 42]. Brody and Flemings derived an expression similar to Scheil's, however they introduced a dimensionless parameter (α) to account for solid-state diffusion by considering solid solute diffusivity (D_s), local solidification time (t_f), and a characteristic length (L – taken as $\frac{1}{2}$ of the dendrite spacing) over which diffusion can take place during solidification. Clyne and Kurz slightly modified the Brody-Flemings model through their introduction of a dimensionless parameter ($\Omega(\alpha)$) that is a function of Brody and Fleming's α parameter. The Clyne-Kurz

approach simplifies to the equilibrium model when α approaches infinity and the Scheil model when α approaches zero. Similar to the Scheil case, the Brody-Flemings and Clyne-Kurz models were originally derived for binary alloy systems and their application to multicomponent alloy solidification requires special treatment. An example multicomponent calculation scheme that accounts for solid-state diffusion was presented by Yamada [43].

CALPHAD-based solidification models have been developed to account for solute back-diffusion in the solid and complete mixing in the liquid. Yamada developed such an approach by recognizing that the original Scheil and Clyne-Kurz equations deviate by the introduction of the $\Omega(\alpha)$ back-diffusion parameter [43]. The multicomponent Scheil scheme was modified such that the $\Omega(\alpha)$ parameter was included to adjust the liquid composition at each temperature step in the simulation. Similar to the binary Clyne-Kurz approach described previously, the Yamada model requires inputs for solute diffusivity in the solid, local solidification time, and dendrite spacing. The model was demonstrated for solidification of a 21Cr-11Ni (wt.%) stainless steel to demonstrate its functionality.

Chen described a model where solid-state diffusion was included in Scheil solidification models by imposing partial-equilibrium conditions [44]. In this model, Chen assumes infinitely fast diffusion of interstitial elements in the solid, no diffusion of substitutional elements in the solid, and complete mixing in the liquid for all solute elements. This was achieved by forcing the chemical potential for a given interstitial solute to equalize in all phases after each sequential temperature step in a multicomponent Scheil simulation. As a result, the interstitial concentration is constantly adjusted throughout the

system while substitutional solute redistribution and solid-state transformations are not considered.

Koseki developed a computational method where stainless steel solidification was simulated by coupling multicomponent computational thermodynamics software with the finite difference method [45]. Local thermodynamic equilibrium was assumed at all phase interfaces, complete mixing was assumed in the liquid, and diffusion coefficients were considered constant with respect to composition. Koseki's model utilizes an iterative finite difference approach to numerically solve for diffusion in the solid-state during solidification and subsequent cooling. Additionally, the Koseki model accounts for solid-state transformation of ferrite to austenite during FA-mode solidification through integration with computational thermodynamic software. A-mode, AF-mode, and FA-mode solidification structures have been simulated using this approach that match experimentally measured weld metal composition profiles quite well. The model also predicts the final ferrite content of welds reasonably well, although underpredictions were noted as experimentally measured ferrite contents increased.

The final solidification modeling approach which will be considered here is a coupled thermodynamic and kinetic (T/K) simulation where diffusion is accounted for in the solid and liquid phases by numerically solving a moving boundary diffusion problem [36, 46]. This approach is similar to that of Koseki but drops the assumption of complete mixing in the liquid. Local thermodynamic equilibrium is assumed at all interfaces and diffusion to/from each interface is solved numerically at small time steps under prescribed cooling conditions. For multicomponent alloys this is handled by using databases that

contain the necessary thermodynamic (Gibbs energy description) and kinetic (mobility/diffusivity) parameters that are needed to solve equilibrium and diffusion conditions within the simulation cell. Additionally, coupling thermodynamic and kinetic databases avoids the assumption that diffusivities are concentration independent.

Lee used a T/K simulation strategy to study the solidification behavior of 304 stainless steel and compare the results to those obtained during directional solidification experiments from another study [47]. The simulations were conducted using the ThermoCalc and DICTRA software packages. Lee simulated the 304 solidification behavior by setting up a 1-dimensional liquid cell with ferrite and austenite at opposite ends of the liquid, and stepped the temperature of the cell from the liquidus temperature to 1000 °C at cooling rates of 0.3 and 1 °C/s. The simulation cell size was determined by using an empirically derived relationship for secondary dendrite arm spacing as a function of cooling rate for the given cooling conditions. Simplifications had to be made with respect to the chemical composition of the stainless steel due to limitations with the available databases at the time by either neglecting certain elements or by reducing the number of elements through Schaeffler's Ni and Cr equivalency relationships [26]. Simulations predicted approximately 20% ferrite in the final structure, whereas experiments showed approximately 10%. Lee attributed the discrepancy to experimental errors in cooling rate measurements, phase fraction measurements, and/or database limitations. Hillert later performed an independent assessment of the simulations and concluded that database limitations and temperature measurement errors were unlikely, but that the cell size and/or chemical composition assumptions used by Lee could account for the observed

inconsistencies [48]. Furthermore, Hillert pointed out that the simulation cell structure was consistent with eutectic solidification, whereas peritectic solidification was expected for 304 stainless steel. Later, Baldissin essentially duplicated Lee's work and found that the simulation results converged with experimental findings when the full composition was considered [49].

Bermejo and Wessman recently used Thermo-Calc and DICTRA to simulate the solidification of various austenitic stainless steel weld metals with varying solidification modes and ferrite balances and compared them to experimental results [50]. The researchers compared four different stainless steels and used a matrix of simulation conditions (varying cell size and reaction scheme) to test the predictive accuracy of the models for ferrite content at a fixed cooling rate of 10 °C/s. It was concluded that AF solidification was best modeled with a eutectic scheme, and FA solidification was best modeled with a peritectic scheme. They also found that the final ferrite balance of an F-mode alloy could be predicted by considering solid-state diffusion only and starting the simulation at the nominal alloy composition just below the equilibrium solidus temperature.

The limitation of using T/K simulations that account for diffusion in all phases is threefold. Simulations of this type are computationally intensive, and simulation times scale non-linearly with the number of chemical components included. Fortunately, advances in computational capacity and multi-core processing make executing these simulations faster than ever before. Secondly, similar to all of the modeling approaches that require use of kinetic and/or thermodynamic databases, information must be

sufficiently populated for the phases and components in the simulation. Fortunately, databases are readily available that cover the composition space for austenitic stainless steels such as the Thermo-Calc® TCFE and MOBFE databases [51]. Lastly, properly developing a simulation cell requires knowledge about the length scale, solidification mode, and cooling rate of the system to be modeled.

A commonality amongst all of the presented solidification models that describe solute redistribution and local interface equilibrium is that the first solid phase to form during solidification (i.e. the primary solidification mode) will be that which is thermodynamically stable at the liquidus temperature for a given alloy composition. In other words, the primary solidification mode can be determined by assessing equilibrium phase diagrams.

Modeling of Austenitic Stainless Steel Solidification – Kinetics

The solidification process can be broken into two parts [52]. First, nucleation of new grains is necessary as the liquid cools from above the liquidus temperature of the alloy. An energy barrier for nucleation arises from the difference between the volume free energy and interfacial energy associated with forming the new solid. The free energy change for homogeneous nucleation (ΔG_{hom}) can be written as:

$$\Delta G_{hom} = -V_S \Delta G_V + A_{SL} \gamma_{SL}$$

where V_S is the volume of the solid nucleus, ΔG_V is the volumetric change in free energy associated with forming the solid nucleus, A_{SL} is the solid-liquid surface area, and γ_{SL} is

the solid-liquid interfacial energy. For a spherical nucleus of radius r , the free energy change for homogenous nucleation can be written as:

$$\Delta G_{hom} = -\frac{4}{3}\pi r^3 \Delta G_V + 4\pi r^2 \gamma_{SL}$$

At small radii the interfacial energy term dominates, while at large radii the volume term dominates. As such, there is a critical nucleus size and corresponding energy barrier that the system must overcome in order to stabilize solid nuclei, known as the activation energy. The activation energy is overcome by undercooling the liquid.

During heterogeneous nucleation, a substrate is present (referred to as the mold here) that serves as a nucleation site for the solid nucleus. The free energy change for heterogeneous nucleation (ΔG_{het}) can be written as:

$$\Delta G_{het} = -V_S \Delta G_V + A_{SL} \gamma_{SL} + A_{SM} (\gamma_{SM} - \gamma_{LM})$$

where terms are added to the homogenous nucleation case for the surface area of the solid-mold interface (A_{SM}), solid-mold interfacial energy (γ_{SM}), and liquid-mold interfacial energy (γ_{LM}). In the heterogeneous nucleation case, the nucleus takes the form of a spherical cap of radius r , and the free energy change for heterogeneous nucleation can be rewritten as:

$$\Delta G_{het} = \left(-\frac{4}{3}\pi r^3 \Delta G_V + 4\pi r^2 \gamma_{SL} \right) \left[(2 + \cos\theta) \frac{(1 - \cos\theta)^2}{4} \right]$$

$$\Delta G_{het} = \Delta G_{hom} \left[(2 + \cos\theta) \frac{(1 - \cos\theta)^2}{4} \right]$$

where θ is the wetting angle formed at the intersection of the solid-liquid and solid-mold interfaces. Inspection of the expression for ΔG_{het} reveals that for wetting angles $<180^\circ$, the free energy change for heterogeneous nucleation is less than the free energy change for homogeneous nucleation. Similar to the homogeneous case, there is a critical nucleus size and energy barrier to stabilize nucleation. While the critical radius remains the same between the homogeneous and heterogeneous nucleation cases, the activation energy is reduced for heterogeneous nucleation due to the wetting angle of the solid nucleus.

Fusion weld solidification presents a case where the nucleation of grains occurs heterogeneously from the edge of the fusion boundary where the molten liquid is in contact with the solid substrate in the partially melted zone. Given that the solid in the partially melted zone is fully wetted by the liquid weld metal (i.e. θ approaches zero in the ΔG_{het} expression for nominally similar substrate and weld metal compositions), there is little-to-no energy barrier for nucleation at the solid-liquid interface. Nominally similar substrate and weld metal compositions in this context refers to either autogenous fusion welding where no filler metal is used, or when the filler metal and substrate compositions are comparable. Comparisons of the free energy change associated with homogeneous, heterogeneous, and fusion welding nucleation are schematically shown in Figure 8. In the figure, r^* represents the critical radius of the solid nucleus, ΔG_{hom}^* is the activation energy for homogeneous nucleation, ΔG_{het}^* is the activation energy for heterogeneous nucleation, and ΔG_{fw} is the free energy change associated with fusion welding. Since the activation energy for nucleation during typical fusion welding conditions is essentially zero when the substrate and weld metal are nominally similar, weld metal solidification is generally

limited by growth kinetics rather than nucleation kinetics. Weld metal grains can easily grow in this case at temperatures near the liquidus temperature of the alloy since nucleation is not necessary.

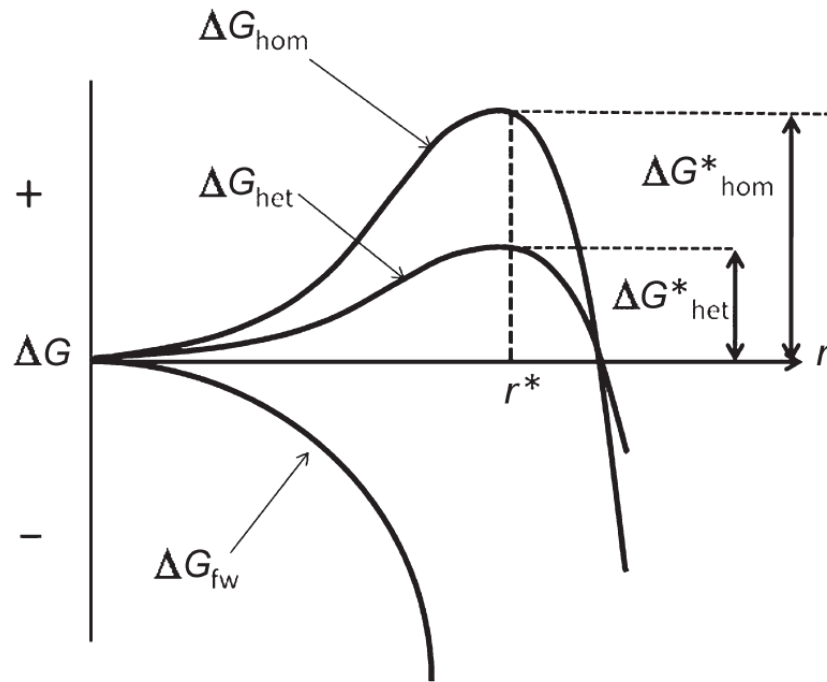


Figure 8: Schematic comparison of free energy changes related to homogenous, heterogeneous, and fusion welding nucleation [39]

Growth of grains into the weld pool occurs by a process called epitaxial growth when the weld metal and substrate are similar [53]. During epitaxial growth, the newly formed solid at the fusion boundary assumes the crystallographic orientation of the grains within the partially melted zone. Growth continues along preferred $\langle 100 \rangle$ growth directions for cubic structures (BCC and FCC metals). Newly solidifying grains which

have their $\langle 100 \rangle$ growth direction aligned parallel with the direction of heat flow will tend to stifle the growth of grains which are not favorably oriented with respect to the heat flow direction. This process is known as competitive growth.

Various growth morphologies are possible during fusion weld solidification including planar, cellular, columnar dendritic, and equiaxed dendritic [54]. The active growth morphology for a solidification front is controlled primarily by the velocity of the solid-liquid interface and temperature gradient in the liquid at the solid-liquid interface for a given alloy. The breakdown of a planar solidification front into other solidification morphologies is most often described using the concept of constitutional supercooling, although a more complex morphological stability analysis of the solid-liquid interface has also been developed [55, 56].

Most solute elements tend to segregate to the liquid and locally depress the liquidus temperature at the solid-liquid interface. Far away from the solid-liquid interface in the bulk weld metal, the liquidus temperature matches that of the nominal alloy composition. The temperature gradient in the liquid at the solid-liquid interface is positive during welding, where the temperature increases from the solid-liquid interface in the direction of the heat source. This condition is known as constrained growth. When the local liquidus temperature falls below the local temperature imposed by the welding process, the liquid is undercooled at the interface and leads to interface instability. As the extent of constitutional supercooling increases, the growth morphology shifts between the bounding cases of planar and equiaxed dendritic solidification. Planar growth occurs when the temperature gradient is sufficiently steep to avoid breakdown of the solid-liquid interface.

In the case of equiaxed dendritic solidification, the liquid is sufficiently undercooled to promote nucleation of new grains ahead of the solid. Cellular and columnar dendritic growth morphologies represent intermediate levels of undercooling between the bounding cases of planar and equiaxed dendritic growth. The concept of constitutional supercooling is presented schematically in Figure 9.

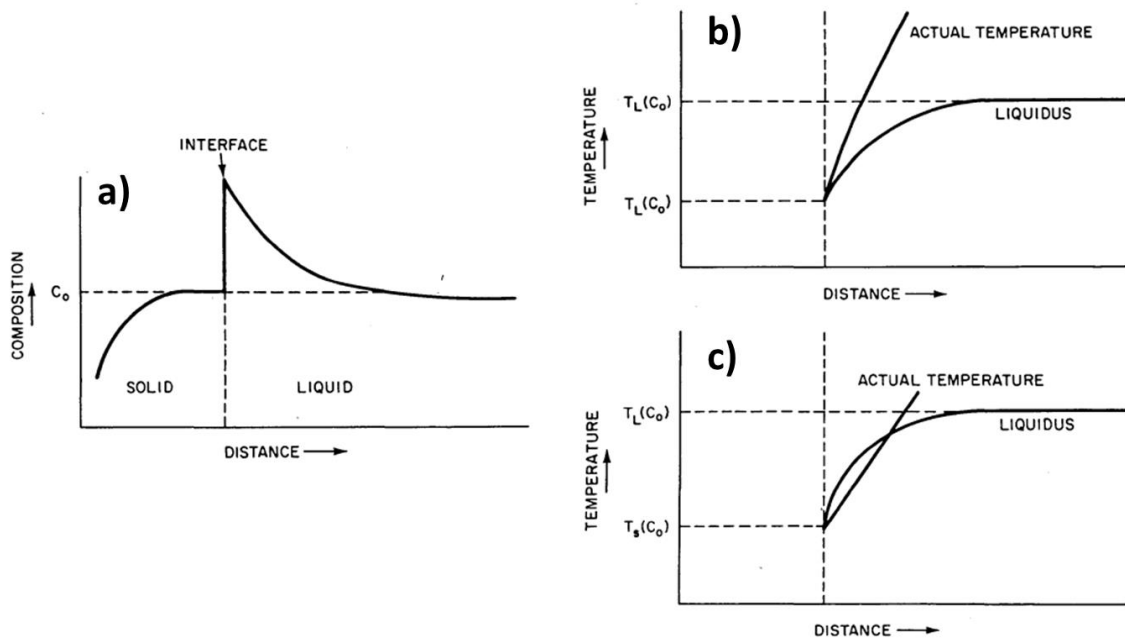


Figure 9: Schematic representation of constitutional supercooling; a) the steady state composition profile at a planar solidification front; b) temperature conditions at the solidification front which promote planar growth; c) temperature conditions at the solidification front which promote breakdown of planar growth due to undercooling [54]

In addition to controlling growth morphologies, the solidification front velocity, liquid temperature gradient, and alloy composition determine phase stability. As such, considerable effort has been devoted to developing and implementing models which can describe the solid-liquid interface response of various phases and solidification morphologies during constrained growth [57]. In such models, solutions are developed for the steady-state interface temperature of various phases, and solidification morphologies of those phases, as functions of solidification rate, temperature gradient, and composition. Phase and morphology selection can then be forecasted through the application of a maximum growth temperature criterion (i.e., the phase/morphology with the highest steady-state temperature will preferentially grow for a given set of solidification conditions) when all relevant interface response models are compared.

An interface response modeling approach that is particularly useful to describe stainless steel solidification during constrained growth is to model the dendrite tip temperature for austenite and ferrite independently [58, 59]. The dendrite tip temperature can be described by assessing the liquidus temperature for a given phase and applying appropriate adjustment terms to account for undercooling at the solid-liquid interface. Dendrite tip temperature solutions are developed for both austenite and ferrite as functions of chemical composition, growth velocity, and temperature gradient. The models generally assume isolated steady-state dendrite growth under constrained thermal conditions. Additionally, it is also assumed that phase selection is not nucleation limited, i.e., nucleation sites are abundant for both phases. Most typically, the austenite and ferrite dendrite tip temperature solutions are presented as functions of growth velocity for a given

steel composition and imposed temperature gradient. An example interface response model for a stainless steel alloy during laser welding conditions is presented in Figure 10. The transition velocity (denoted as v_c^* in Figure 10) separates the predictions for ferrite (T_δ^*) and austenite (T_γ^*) growth at low and high interface velocities, respectively. Figure 10 also shows the stable equilibrium liquidus temperature for ferrite (T_{liq}^δ) and metastable equilibrium liquidus temperature for austenite (T_{liq}^γ) as horizontal lines at higher temperatures than the steady-state dendrite tip temperature solutions. Metastable austenite growth is predicted at high velocities due to differences in the growth kinetics of the ferrite and austenite dendrite tips. That is to say, less undercooling (difference between the liquidus temperature and dendrite tip temperature solution) is observed for austenite as the solidification front velocity increases, promoting metastable growth.

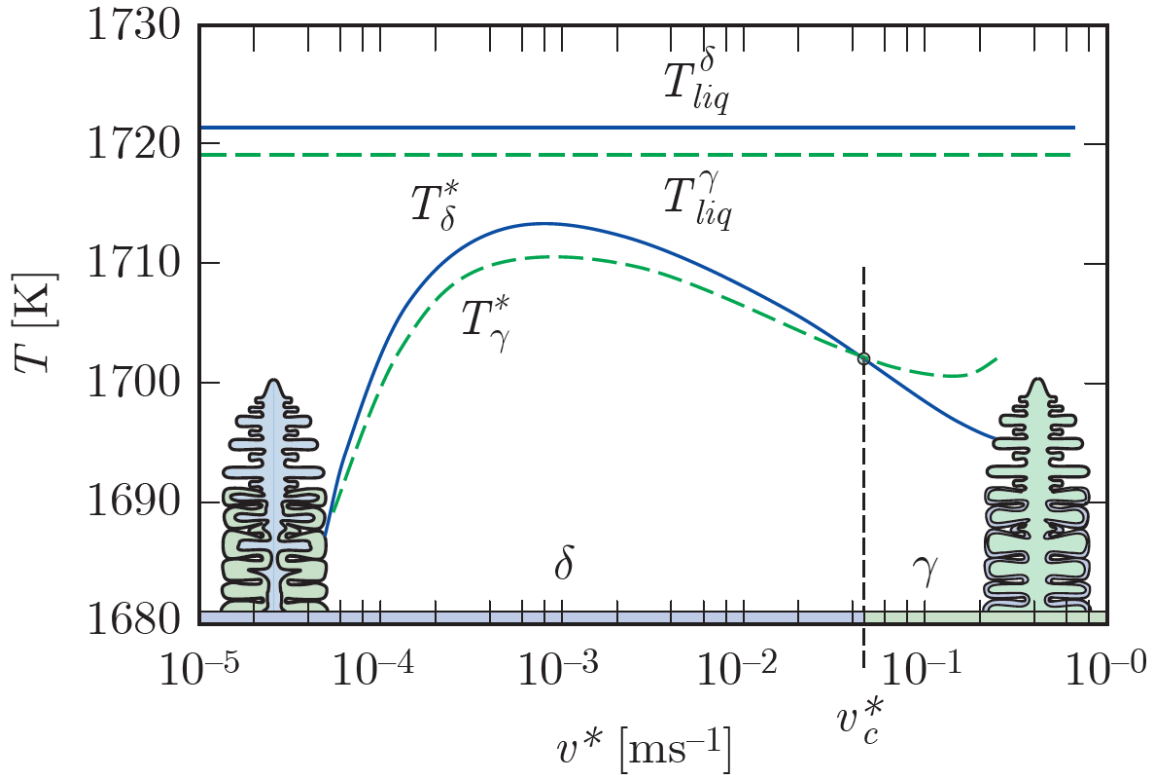


Figure 10: Steady-state dendrite tip temperature solutions for ferrite (T_{δ}^*) and austenite (T_{γ}^*) in a Fe-Ni-Cr-C austenitic stainless steel alloy showing metastable austenite growth at high growth velocities; $G=400$ °K/mm [59, 60]

The interface response approach has been successfully applied to describe phase and morphology selection for a range of stainless steel compositions and constrained solidification conditions [59, 61-66]. These studies include solidification conditions ranging from directional solidification at low growth velocities to high energy density processes such as laser beam and electron beam welding at high growth velocities. Additionally, the composition ranges that were assessed extend from high-purity ternary Fe-Ni-Cr systems to full multicomponent austenitic stainless steel chemistries. As

mentioned previously, the most applicable interface response model that is relevant to austenitic stainless steel weld metal solidification is for dendrite growth (as shown in Figure 10).

For example, a dendrite tip temperature model for a given phase can be constructed for a ternary Fe-Ni-Cr stainless steel chemistry as:

$$T_d = T_L + \Delta T$$

where T_d is the dendrite tip temperature, T_L is the equilibrium liquidus temperature, and ΔT is the total undercooling at the dendrite tip [65, 66]. The total undercooling term can be expanded to the form:

$$\Delta T = \Delta T_S - \Delta T_R$$

where undercooling contributions from solute diffusion at the solid-liquid interface (ΔT_S) and curvature of the dendrite tip (ΔT_R) are introduced. Undercooling due to solute diffusion (often called solutal or constitutional undercooling) arises from the enrichment of solute in the liquid at the dendrite tip. An expression for solutal undercooling can be written as:

$$\Delta T_S = \sum_{i=1}^2 m_i (c_i^* - c_{0,i})$$

where i represents Ni or Cr, m_i is the slope of the equilibrium liquidus surface for each element i , c_i^* is the concentration of element i in the liquid at the dendrite tip, and $c_{0,i}$ is the concentration of element i in the bulk alloy.

Undercooling due to curvature of the dendrite tip occurs because of the additional surface energy related to forming the curved dendrite tip interface. This effect causes the

liquidus temperature to change as a function of the dendrite tip radius. The curvature undercooling term can be expressed as:

$$\Delta T_R = \frac{2\Gamma}{R}$$

where Γ is the Gibbs-Thomson coefficient, and R is the radius of the solidifying dendrite.

The expression for the dendrite tip temperature then takes the form:

$$T_d = T_L + \sum_{i=1}^2 m_i (c_i^* - c_{0,i}) - \frac{2\Gamma}{R}$$

A dendrite tip radius selection criterion must be included in the analysis along with a description of the solute diffusion field around the dendrite tip. This is achieved by combining the Ivantsov solution to the solute transport problem with marginal stability analysis to find the dendrite radius [57, 67]. Using this approach, a solution is obtained that relates the dendrite tip temperature and radius to solidification growth variables (growth velocity and temperature gradient) and alloy composition. In this case where local interface equilibrium is assumed, the dendrite tip temperature relates to a position on the liquidus surface of the stable (or metastable) phase diagram that has been adjusted away from the nominal liquidus temperature due to solute segregation and curvature.

Beyond the dendritic Fe-Ni-Cr case with local interface equilibrium presented above, more complex constrained growth models have also been developed to describe larger multicomponent systems and/or non-equilibrium conditions [68-70]. Fukumoto presented such a growth equation to describe metastable austenite growth in austenitic

stainless steel laser welds that should solidify as primary ferrite based on phase diagram predictions [59]. Fukumoto's growth equation can be written as:

$$T_d = T_L + \sum (m_{v,i}c_i^* - m_{0,i}c_{0,i}) - \frac{2\Gamma}{R} - \frac{V}{\mu} - \frac{GD}{V}$$

This dendrite growth model is often referred to as multicomponent KGT theory. There are two key differences between the multicomponent KGT case and the ternary case presented previously. First, multicomponent KGT theory considers velocity-dependent partition coefficients and liquidus slopes for all elements [71-73]. Secondly, there are two additional terms in the multicomponent KGT equation. The fourth term on the right-hand side of the equation represents kinetic undercooling. The fifth term on the right-hand side of the equation represents cellular undercooling. Within the dendrite growth regime of practical importance for traditional fusion welding scenarios, their contributions to the total undercooling are generally negligible. Kinetic undercooling only becomes significant at high solidification velocities, and cellular undercooling only becomes significant at low growth velocities in the transition between planar and dendritic growth [74].

Multicomponent KGT theory was applied to an austenitic stainless steel chemistry from the database that was used to construct the original solidification mode boundary lines on the WRC-1988 diagram [5, 24]. The dendrite tip temperature solution and the fractional contributions of solutal and curvature undercooling are shown in Figure 11 as functions of solidification velocity for both austenite and ferrite. This particular weld metal composition was experimentally determined to solidify as primary austenite, while equilibrium thermodynamic calculations suggest that it should solidify as primary ferrite.

There are three key features of Figure 11 that are noteworthy. First, austenite growth is predicted to be dominant across the full range of simulated solidification velocities even though the equilibrium liquidus for ferrite is slightly greater than that for austenite. Secondly, the contributions from solutal and curvature undercooling account for nearly 70% of the total undercooling at 1×10^{-4} m/s, 97% at 1×10^{-3} m/s, and over 99% at 1×10^{-2} m/s. Lastly, the curvature undercooling contributions are quite similar and range from 2% to 18% of the total undercooling within the simulated solidification velocity range. This provides supporting evidence that the dendrite growth kinetics are mostly driven chemical composition.

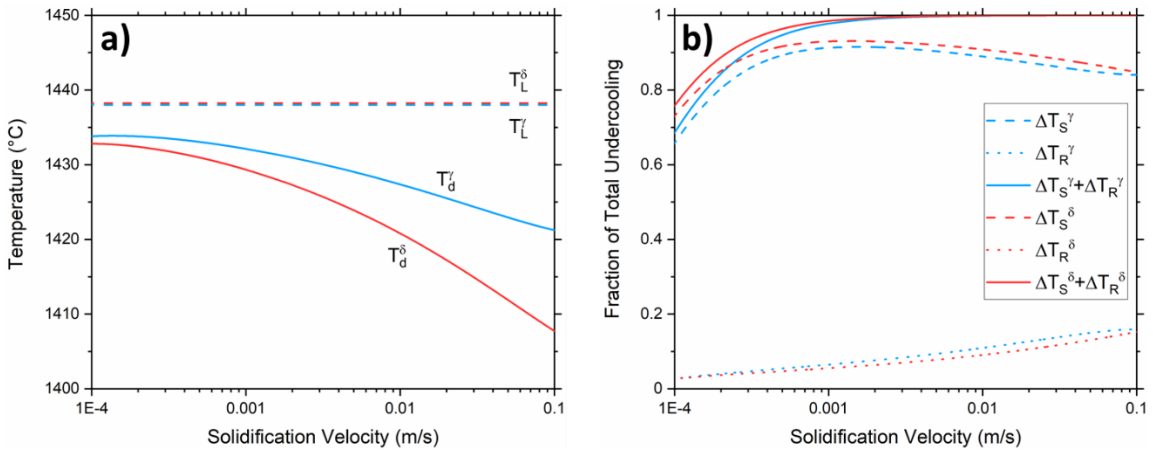


Figure 11: a) Equilibrium liquidus temperatures (T_L) and dendrite tip temperatures (T_d) for austenite (γ) and ferrite (δ) as a function of solidification velocity; b) fractional contributions of solutal (ΔT_S) and curvature (ΔT_R) undercooling as a function of solidification velocity for both phases

Calculation of Phase Diagrams (CALPHAD)

All the multicomponent solidification models presented within the previous sections are either partially or fully reliant on input parameters that are based on thermodynamics. Most typically, this input data is generated using computational thermodynamics and the CALculation of PHase Diagrams (CALPHAD) approach for multicomponent systems [9]. The ever-growing adoption of CALPHAD methodologies has been accelerated in recent years due to the ongoing development and availability of commercial software packages such as Thermo-Calc and PANDAT [51, 75]. Some of the solidification models presented thus far are fully integrated into commercially available platforms such as equilibrium and Scheil solidification conditions. In cases where solidification models are not fully integrated into the software (such as in the multicomponent KGT case), the necessary thermodynamic parameters for the simulations can readily be extracted to support modeling efforts. In the context of solidification modeling, parameters of interest include things like the location of temperature- and composition-dependent phase transition boundaries and equilibrium partition coefficients. An additional benefit of the CALPHAD approach is that it allows for the calculation of metastable states that may be incredibly difficult to study through experiments alone.

CALPHAD is a phase-based modeling approach that is used to describe phase equilibria using thermodynamic concepts. Mathematical models are constructed that describe the Gibbs energy of individual phases as functions of temperature, pressure, and chemical composition. This is enabled by aggregating data from the literature that directly provides or can be used to calculate underlying thermodynamic quantities for a given

phase. Some examples of experimental techniques that can provide useful information include, but are not limited to, differential thermal analysis, calorimetry, and metallographic analysis [9]. A Gibbs energy model can then be constructed with adjustable fitting parameters, which allows thermodynamic database developers to optimize model performance to best fit the experimental observations. By referencing an appropriate database that contains the relevant Gibbs energy model data for a given application, computational thermodynamic calculations can be performed for complex multicomponent alloy systems using numerical techniques.

Chapter 3. Development of CALPHAD-Based Equivalency Relationships for Austenitic Stainless Steel Weld Metals

Introduction

Historically, primary solidification mode predictions for stainless steel weld metals have relied on empirically derived diagrams and equivalency relationships. One such diagram of this type, known as the WRC-1988 diagram, was published in 1988 by Siewert, McCowan, and Olson [4]. The axes of the WRC-1988 diagram consist of linear expressions that relate to the potency for certain elements to either stabilize ferrite or austenite in the weld metal microstructure. Ferrite stabilizing elements are grouped into a chromium equivalent (Cr_{eq}) expression on the horizontal axis. Conversely, austenite stabilizing elements are grouped into a nickel equivalent (Ni_{eq}) expression on the vertical axis. Two sets of linear features are contained within the WRC-1988 diagram. The first set of lines represent iso-ferrite number (FN) projections, where FN is related to the amount of ferrite present within a weld deposit. The second set of lines provide boundaries between the various solidification modes that are typically encountered during arc welding of austenitic stainless steel weld metals. These include primary austenite (A and AF) and primary ferrite (FA and F) solidification modes. Knowing the chemical composition of a given stainless steel weld metal, Cr_{eq} and Ni_{eq} can be calculated to provide a point on the WRC-1988 diagram. The location of that point can then be used to predict FN and

solidification mode. Note that the WRC-1988 equivalencies were developed via multiple linear regression by relating FN and weld metal chemical composition data from over 950 unique weld metal samples provided by various sources. The solidification mode boundary lines were added to the diagram by aggregating experimental data from the open literature. The selected data sets included metallographic and chemical analyses which related solidification mode to chemical composition. That aggregated data was then projected onto the WRC-1988 diagram and boundaries were drawn to delineate regions of similar solidification mode.

The WRC-1988 diagram was later updated by Kotecki and Siewert in 1992 to account for the austenite stabilizing capacity of Cu by adding an additional term in the Ni_{eq} expression [6]. This was primarily added to account for duplex stainless steels that contain Cu additions up to 3 wt.%, which caused the WRC-1988 diagram to overestimate the FN of the weld metal. Known as the WRC-1992 constitutional diagram, the diagram presented by Kotecki and Siewert is one of the most ubiquitous tools available to predict ferrite content and solidification mode for austenitic and duplex stainless steel weld metal chemistries.

Computational thermodynamic calculations based on the CALPHAD method are becoming more commonplace as ease-of-use, database availability, and overall familiarity with commercially available software packages continue to improve. Additionally, computational thermodynamics software packages generally include built-in functionality to perform solidification simulations. Examples include the limiting cases of equilibrium and Scheil solidification simulations to predict solute partitioning behavior and phase

evolution. A natural assumption is that multicomponent computational thermodynamic calculations can provide more accurate solidification behavior predictions than legacy empirically derived tools.

As the welding community reaches the 30-year mark since the introduction of the WRC-1988 and WRC-1992 diagrams, this study aims to explore the possibility of developing a new predictive diagram based on high-throughput computational thermodynamic calculations. Since primary solidification mode is the key characteristic which controls solidification cracking susceptibility in austenitic stainless steel weld metals, focus will be placed on differentiating between primary austenite and primary ferrite solidification modes. All thermodynamic calculations will be performed using Thermo-Calc version 2021a with the TCFE11 Steels/Fe-alloys database.

Equilibrium Assessment of WRC-1988 Database

As mentioned previously, the WRC-1988 diagram was constructed using two separate databases. The first database contained chemical composition and FN data from approximately 950 individual samples. This collection of experimental FN data will be referred to as the WRC Appendix I database. The second database contained chemical composition and solidification mode data that was aggregated from the open literature. This collection of experimental solidification mode data will be referred to as the WRC Appendix II database. These naming conventions reflect the location of the original data tables within the WRC bulletin where the WRC-1988 diagram was presented [5].

The WRC-1988 diagram will be considered here for three reasons. First, the data that was used to construct the original WRC-1988 diagram is readily available in the open literature [5]. Secondly, the modification that was provided in the WRC-1992 Ni_{eq} term was done so to address FN overestimations for duplex stainless steel chemistries that contained significant Cu additions [6]. The rest of the elements that were considered, their coefficients, and the reference lines remained unchanged between the 1988 and 1992 versions of the WRC diagram. Lastly, the composition regime of practical importance for differentiating between primary ferrite and primary austenite solidification covers typical 300 series austenitic stainless steel grades, not duplex stainless steels that may contain significant Cu additions. Outside of a unique dissimilar metal weld scenario that involves alloys with high Cu concentrations, the composition ranges contained within the WRC-1988 database are limiting for applications involving most common austenitic stainless steel grades.

As an initial and somewhat simplistic starting point, equilibrium step calculations were performed on the entire WRC Appendix II database. Liquid, austenite, and ferrite were considered in each calculation. This consisted of calculating phase equilibria from above the liquidus temperature to just below the solidus temperature for each chemical composition in the database. In that sense, this calculation is equivalent to an equilibrium phase diagram at a fixed chemical composition across the equilibrium solidification temperature range. The solid phase in stable thermodynamic equilibrium at the liquidus temperature was recorded for each composition. Figure 12 provides a comparison between the WRC Appendix II solidification mode data and the equilibrium step calculation results

plotted on the WRC-1988 coordinate axes. The original WRC-1988 solidification mode boundaries are also included in Figure 12 for reference.

As observed in Figure 12, a significant discrepancy exists between experimental observations and thermodynamic calculations near the AF/FA transition of the WRC-1988 diagram. Specifically, ferrite is predicted to be thermodynamically stable at the liquidus temperature for many of the stainless steel chemistries that fall above the AF/FA transition of the diagram. Conversely, the primary ferrite experimental data below the AF/FA transition agrees with thermodynamic calculations.

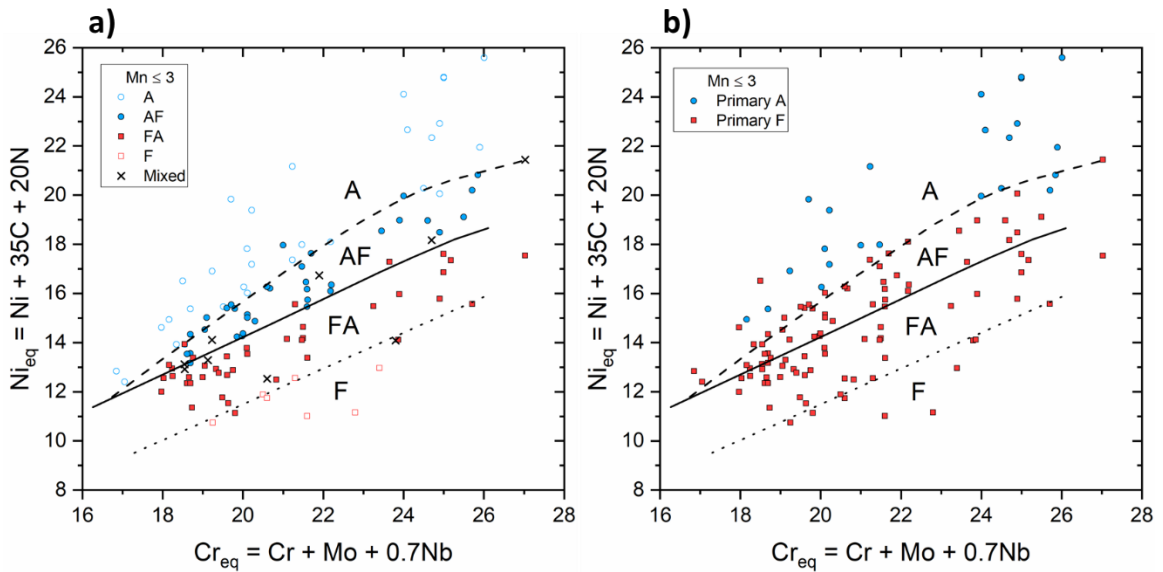


Figure 12: a) Original solidification mode data plotted onto the WRC-1988 diagram to construct solidification mode boundaries; b) Calculated stable solid phase at the nominal liquidus temperature for each sample

Expansion to Randomly Generated Austenitic Stainless Steel Chemistries

To evaluate whether any specific composition trends were related to the discrepancy in Figure 12, a new database of theoretical chemical compositions that fell within the published composition bounds of the WRC-1988 diagram was created. To do so, maximum and minimum concentration limits were set for each element. The maximum and minimum concentration limits for each element were determined by plotting concentration histograms for each element within the WRC Appendix I and WRC Appendix II databases. Limits were set by considering the overall distribution for each element and ignoring obvious outliers that were not representative of the population. The following observations were made when analyzing the concentration histograms for each element:

- Carbon: WRC Appendix I shows a bimodal distribution between 0.008-0.100 wt.%, and very few samples are >0.100 wt.%. WRC Appendix II shows a unimodal distribution between 0.004-0.130 wt.% that is skewed toward low values.
- Manganese: WRC Appendix I shows a multimodal distribution, with most of the data falling between 0.03-3.00 wt.%. Small subpopulations are apparent up to 12.67 wt.% that are associated with high-Mn / low-Ni grades. WRC Appendix II shows a similar distribution for Mn.
- Silicon: WRC Appendix I shows a bimodal distribution ranging between 0.03-1.30. WRC Appendix II shows a similar distribution for Si.

- Chromium: WRC Appendix I shows a bimodal distribution between 14.74-28.60 wt.%. Very few samples fall outside of this range. WRC Appendix II shows a similar distribution for Cr.
- Nickel: WRC Appendix I shows a fairly normal distribution between 4.80-17.20 wt.%. Some outliers are present below and above this range. Low values are associated with high-Mn / low-Ni grades, while some isolated Ni concentrations are nonsensically high with respect to the A/F transition and are separated from the main data population. WRC Appendix II shows a similar distribution for Ni.
- Molybdenum: WRC Appendix I shows a distinct bimodal distribution between 0.01-5.42 wt.%. One large subpopulation corresponding to grades that do not contain Mo as a primary alloying addition appears below approximately 0.5 wt.%. The second subpopulation extends up to 5.42 wt.%. WRC Appendix II shows a similar distribution for Mo.
- Nitrogen: WRC Appendix I shows a bimodal distribution between 0.010-0.250 wt.%. Most of the data falls within a subpopulation below 0.140 wt.%. Very few samples contained above 0.25 wt.%. WRC Appendix II shows a similar distribution, although the minimum and maximum concentrations are lower and higher, respectively.
- Other elements: WRC Appendix I also contains data for Nb, Ti, Cu, V, and Co. However, concentration data for these elements are not reported for all samples within the database. For the values that were reported within WRC Appendix I, most concentrations were quite low. For example, most of the reported Nb data

falls below 0.05 wt.% and Ti data falls below 0.07 wt.%, indicating that the data does not represent stabilized austenitic stainless steel grades. WRC Appendix II does not contain information for Nb, Ti, Cu, V, and Co.

Using the representative concentration limits that were identified through the WRC Appendix I and Appendix II distribution analysis, a database of randomized theoretical chemical compositions was created. The concentration for each element was randomly generated between the maximum and minimum values that were identified for a given theoretical chemical composition. Using this approach, the concentrations for each of the elements were uniformly distributed between their respective concentration limits. Additionally, the database was free of collinearity amongst the alloying elements. That is, there were no systematic trends with an alloying element changing with respect to any other alloying element. A total of 11,000 theoretical chemical compositions were generated. This database of randomized stainless steel chemistries will be referred to as the Theoretical WRC database in the following text.

A comparison of the chemical concentration limits for the published WRC-1988 diagram [4], WRC Appendix I database, WRC Appendix II database, and Theoretical WRC database can be seen in Table 1. Table 1 also provides the number of samples within the WRC Appendix I and Appendix II databases with reported values for a given element. Lastly, the percentage of the WRC Appendix I and Appendix II populations that are captured by the Theoretical WRC database chemical concentration limits are listed for each element.

Table 1: Austenitic stainless steel concentration limits for the published WRC-1988 diagram, WRC Appendix I database, WRC Appendix II database, and Theoretical WRC database

Element	Published Concentration Range for WRC-1988 (wt.%)	WRC Appendix I		WRC Appendix II		Theoretical WRC			
		Concentration Limits (wt.%)	n	Concentration Limits (wt.%)	n	Concentration Limits (wt.%)	n	WRC Appendix I Population Contained within Concentration Limits (%)	WRC Appendix II Population Contained within Concentration Limits (%)
C	0.01-0.15	0.008-0.200	923	0.004-0.180	152	0.008-0.100	11000	99	93
Mn	0.4-12	0.35-12.67		0-9.20		0.03-3.00		91	80
Si	0.1-1.3	0.03-1.30		0.01-1.56		0.03-0.94		95	94
Cr	15-32	14.74-32.00		15.80-26.90		14.74-28.60		99	100
Ni	5-25	1.70-33.50		4.20-27.60		4.80-17.20		97	87
Mo	0-7	0.01-6.85		0-6.24		0.01-5.42		99	84
N	0.03-0.3	0.010-0.300		0.001-0.429		0.010-0.140		89	64
Nb	0-0.9	0-0.88		-		-		0-0.05	97*
Ti	0-0.1	0-0.33	493	-	-	0-0.07		98*	-
Cu	-	0-3.04	623	-	-	0-0.27		95*	-
V	-	0-0.23	448	-	-	0-0.12		99*	-
Co	-	0-0.32	448	-	-	0-0.10	94*	-	

*Missing values counted as 0

Reviewing the percentages of the WRC Appendix I and Appendix II sample populations that are restricted by the Theoretical WRC concentration limits reveals that nearly 90% or more of the elemental populations are represented in most cases. There are, however, certain elements that warrant further discussion.

The published concentration limits for Mn in the WRC-1988 diagram ranged from 0.4-12 wt.%. However, 91% of the WRC Appendix I sample population contained ≤ 3 wt.% Mn. Similarly, 80% of the WRC Appendix II sample population contained ≤ 3 wt.% Mn. The lower percentage of the WRC Appendix II Mn data stems from the fact that a larger proportion of the database was made up of high-Mn / low-Ni austenitic stainless steel grades.

Similarly, the published N concentration limits for the WRC-1988 diagram ranged from 0.03-0.3 wt.%. Nearly 90% of the WRC Appendix I data is bounded by an upper limit of 0.140 wt.%. Of the nearly 10% of the WRC Appendix I data that falls above 0.140 wt.%, most of that data comes from high-Mn and duplex stainless steel chemistries. Additionally, the WRC Appendix II database contained entries from studies that considered high-N stainless steels for cryogenic service, 300-series N grades with elevated N contents, high-Mn / low-Ni grades, and austenitic stainless steel welds where N₂ was added to the shielding gas to intentionally study the effect of N on solidification cracking [24, 76, 77]. A small collection of entries in the WRC Appendix II database also came from relatively pure Fe-Ni-Cr ternary alloys. This explains why only 64% of the WRC Appendix II N data is contained by the Theoretical WRC database limits.

Lastly, the Mo concentration limits of the Theoretical WRC database is limiting for over 99% of the WRC Appendix I data. A smaller percentage of the WRC Appendix II Mo data is contained within the Theoretical WRC database concentration limits. A subpopulation of the WRC Appendix II data was reported as containing 0.00 wt.% Mo within the database. Upon further investigation, the data originated from a study by Ogawa and Koseki where Mo concentrations were not reported by the authors [76]. The data which originated from Ogawa and Koseki therefore fell outside of the Mo concentration limits for the Theoretical WRC database.

Overall, the concentration limits that were defined for the Theoretical WRC database represent the WRC Appendix I and Appendix II data quite well. The concentration ranges can be considered limiting with respect to most common austenitic

stainless steel grades. Obvious omissions include high-Mn grades, stabilized grades, and N grades with particularly high N contents.

Phase equilibria calculations similar to those presented in Figure 12 were repeated on the Theoretical WRC database. The stable solid at the calculated liquidus temperature for each theoretical chemistry is presented on the WRC-1988 coordinate axes in Figure 13. As can be seen, similar behavior to the WRC-1988 Appendix II case is observed where primary ferrite solidification is predicted above the WRC-1988 AF/FA transition line. The chemical compositions of the calculations which exhibited ferrite stability within the primary austenite region of the WRC-1988 diagram were analyzed by plotting elemental concentration distributions and comparing them to the WRC Theoretical database concentration limits. No systematic chemical composition trends were observed through this exercise except for Ni and Cr. The Ni and Cr concentrations that showed ferrite stability above the AF/FA transition line were slightly skewed toward intermediate Ni and low Cr values. This Ni and Cr effect is simply associated with the location of the AF/FA transition on the WRC-1988 diagram and the wide range of Ni and Cr concentrations that were included in the Theoretical WRC database.

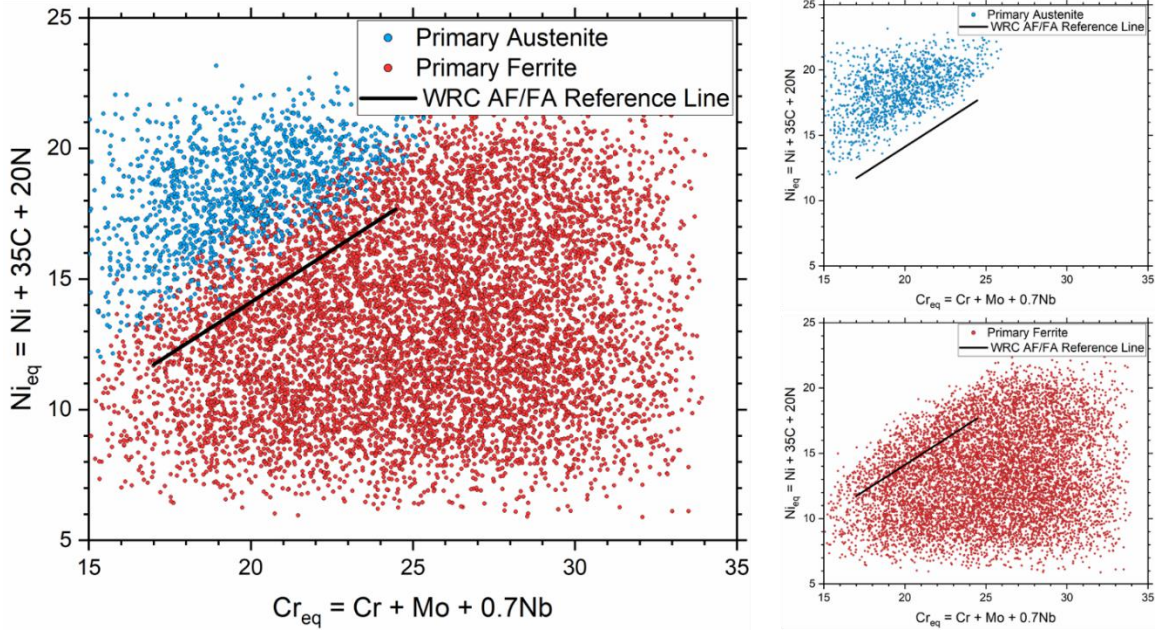


Figure 13: Calculated stable solid phase at the nominal liquidus temperature for each alloy in the Theoretical WRC database plotted on the WRC-1988 equivalency space

Figure 12 and Figure 13 show that, with the exception of a thin region where austenite and ferrite predictions are mixed that runs parallel to the original WRC-1988 AF/FA transition line, the phase equilibria calculations plotted onto the WRC coordinate axes show a fairly linear separation between primary austenite and primary ferrite. Given that the WRC-1988 Cr_{eq} and Ni_{eq} expressions were actually developed using the WRC Appendix I data by relating FN and chemical composition, it is possible that a more sharply defined transition may be achieved by developing new equivalencies that are based on a metric that is directly related to solidification mode, not ferrite content of the weld metal.

To explore this concept, two computational thermodynamic simulation schemes were devised that relate directly to solidification mode predictions. Each scheme provides

a single metric for a single stainless steel chemical composition. By simulating a large population of stainless steel chemical compositions, multiple regression analysis can be used to generate new sets of equivalency relationships. Specifically, multicomponent Scheil and stable/metastable equilibria calculations will be applied to the Theoretical WRC database to develop new equivalencies.

Computational Framework

Scheil Simulations

Scheil solidification simulations represent an extreme case of solute segregation where no solute diffusion is considered in the solid, solute diffusion in the liquid is considered infinitely fast, the solid-liquid interface is at local equilibrium, and no undercooling is considered for nucleation or growth [39]. Considering that the equilibrium solidification partition coefficient ($k = C_S/C_L$) for most solute elements is <1 , the liquid is continuously enriched in solute elements until solidification is complete. For the case of multicomponent Scheil solidification simulations, an iterative process using computational thermodynamics software is used. The general multicomponent Scheil scheme is performed by iteratively calculating the equilibrium solid and liquid compositions at the solid-liquid interface, molar fraction of solid phase(s) formed, and the resulting liquidus temperature of the segregated liquid across small temperature steps through the solidification temperature range. Through this process, solidification begins at the nominal

liquidus temperature of the alloy and proceeds until a terminal invariant reaction or predefined fraction of solid is reached by the system.

In this investigation, the partial equilibrium Scheil model of Chen and Sundman was used to account for back diffusion of C and N during the solidification process [44]. The partial equilibrium Scheil model was used to simulate all 11,000 randomized compositions contained within the Theoretical WRC database. Only liquid, austenite, and ferrite were considered in each simulation. The simulations were terminated at 0.99 fraction solid. The particular data of interest for each simulation consisted of the solid-liquid interface temperature as a function of fraction solid, and the specific fraction solid where austenite and ferrite first appeared during solidification.

A parameter was defined to serve as the solidification metric that relates to primary solidification mode for each stainless steel chemistry. The new parameter, Δf_S , was defined as:

$$\Delta f_S = f_S^{\delta^*} - f_S^{\gamma^*}$$

where $f_S^{\delta^*}$ and $f_S^{\gamma^*}$ are the molar solid fractions where ferrite (δ) and austenite (γ) first form during the solidification sequence. If ferrite or austenite did not form during the solidification sequence, their respective molar solid fractions were set to 0.99. A graphical representation of the Δf_S parameter for a series of ternary alloys from the 70 wt.% Fe isopleth of the Fe-Ni-Cr system are presented in Figure 14.

The significance of selecting ferrite as the first term on the right-hand side of the Δf_S equation is trivial. Rather, it is simply a convention that was adopted that allows the simulation results to span from $-0.99 \leq \Delta f_S \leq 0.99$, where primary austenite alloys are

positive and primary ferrite alloys are negative. The condition of $\Delta f_S = 0$ represents the multicomponent monovariant line that separates the two primary growth modes. The magnitude of a given Δf_S value then provides an indication for how far away a chemical composition sits from the austenite / ferrite transition and accounts for solute segregation during the solidification process. Each simulated Δf_S was recorded for the Theoretical WRC database to support multiple regression analysis.

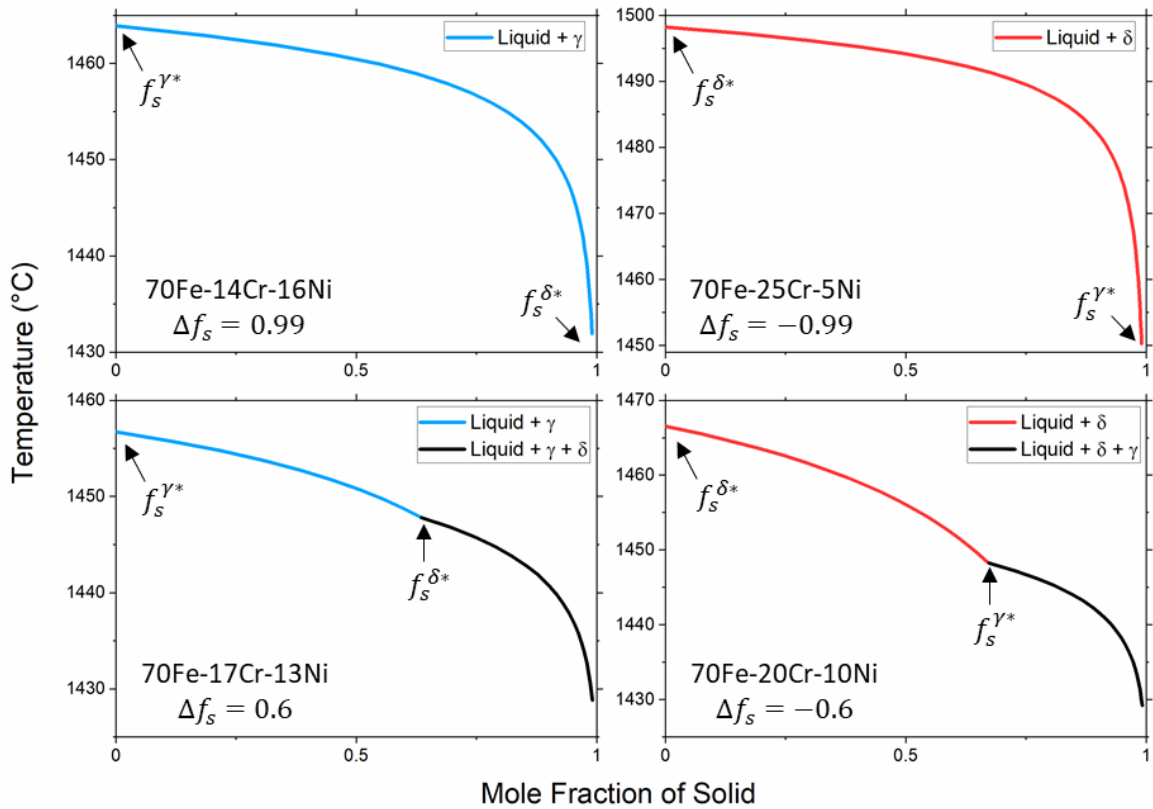


Figure 14: Example Δf_S calculations from the ternary Fe-Ni-Cr system

Stable and Metastable Equilibria

The second scheme explored during this investigation involved calculating the stable and metastable liquidus temperatures for a given chemical composition by independently calculating phase equilibria as a function of temperature for liquid + austenite and liquid + ferrite. The liquidus temperatures for austenite and ferrite were calculated for all 11,000 compositions in the Theoretical WRC database.

Again, a parameter was defined to serve as a metric for the solidification mode for a given chemical composition. The parameter, ΔT_L , was defined as:

$$\Delta T_L = T_L^\gamma - T_L^\delta$$

where T_L^γ is the austenite liquidus temperature and T_L^δ is the ferrite liquidus temperature for a given alloy composition. As a simplified example, a ΔT_L calculation is presented in Figure 15 from the 70 wt.% Fe isopleth of the ternary Fe-Ni-Cr system. The simplified Fe-Ni-Cr system presented in Figure 15 was selected to provide a visual aid since the stable and metastable phase equilibria lines lie in the plane of the Figure. Figure 15 also demonstrates one major utility of computational thermodynamics in that metastable states can readily be simulated.

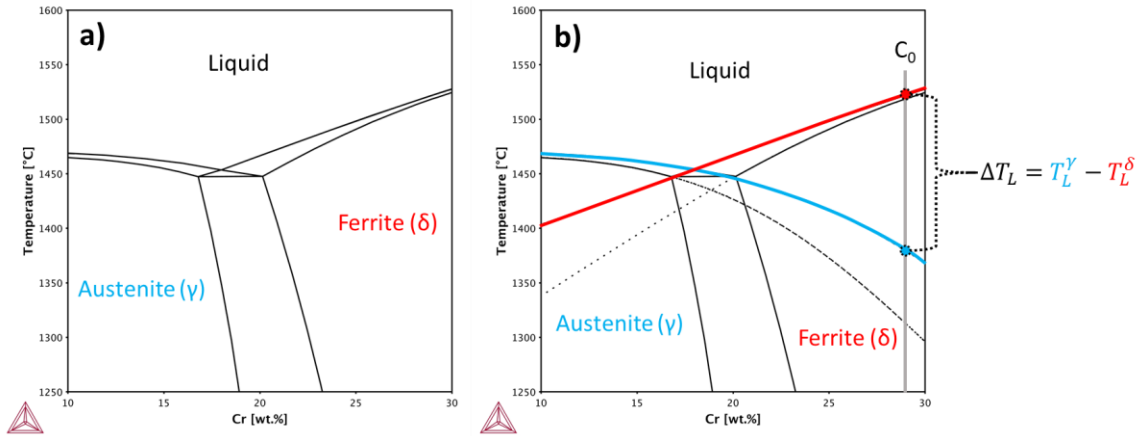


Figure 15: Example ΔT_L calculation from the ternary Fe-Ni-Cr system; a) equilibrium phase diagram of the 70 wt.% Fe isopleth from the Fe-Ni-Cr system; b) phase diagram of the same system with the stable and metastable liquidus and solidus boundaries plotted

Similar to the Δf_S parameter, the selection of austenite as the first term on the right-hand side of the ΔT_L equation is simply a matter of convention. Alloys with a positive ΔT_L represent primary austenite stability and those with a negative ΔT_L represent primary ferrite stability under equilibrium conditions. The condition of $\Delta T_L = 0$ represents the multicomponent monovariant line that separates the two primary growth modes. The magnitude of ΔT_L provides an indication for how far removed a given chemical composition is from the austenite / ferrite transition. The ΔT_L values for the Theoretical WRC database were recorded to support multiple regression analysis.

Formulating New Equivalencies

The development of new Cr_{eq} and Ni_{eq} expressions was performed using backward elimination multiple regression to independently establish relationships between chemical composition and the calculated solidification parameters, Δf_S and ΔT_L . The regression process relied on the method of least squares and was performed using commercially available statistical analysis and graphing software [78, 79]. The multiple regression models had the general form:

$$Y = b_0 + b_1C_1 + b_2C_2 \cdots b_iC_i$$

where Y represents Δf_S or ΔT_L , b_0 is a constant, b_i is the partial regression coefficient for element i , and C_i is the concentration of element i in wt.%. Second order concentration terms were also evaluated in some cases.

All elements contained within the Theoretical WRC database were initially assessed. An iterative process was used to systematically eliminate specific elements that were deemed insignificant through t-tests. An element regression coefficient with the highest p-value would be eliminated and the model would be refit. This process was repeated until all regression coefficients had p-values less than 0.05. Once the final model was fit the regression coefficients, standard errors for those regression coefficients, adjusted R^2 , and root mean square error were recorded. Residuals analysis was also performed to check for systematic trends in model error. Partial residuals plots were also created to assess if model errors had a mean of zero and constant variance with respect to each element.

Once a regression model was constructed, Cr_{eq} and Ni_{eq} were formulated by manipulating the regression model into the form:

$$Y = b_0 - b_{Cr}(Cr_{eq}) + b_{Ni}(Ni_{eq})$$

where like-sign elements and their coefficients were grouped and normalized by b_{Cr} or b_{Ni} for the Cr_{eq} and Ni_{eq} expressions, respectively. The coefficients for austenite stabilizers were always positive (similar to Ni) and ferrite stabilizers were always negative (similar to Cr) due to the conventions that were established for each model type.

The Theoretical WRC database was also partitioned to assess the efficacy of developing regression models on subsets of the Theoretical WRC database and/or evaluate coefficient stability for certain elements.

Results and Discussion

Scheil Simulations

Regression analysis was performed on the Δf_S data using two sampling strategies. The first sampling strategy involved randomizing the database and subsequently analyzing the data as a function of the percentage of the total database population. This randomized sampling strategy was selected to assess regression model stability and determine how sample size influenced the regression results. The second sampling strategy involved sorting the database by $|\Delta f_S|$ in ascending order. Similar to the randomized data, regression iterations were performed as a function of the percentage of the total database population

for the sorted data. The sorted regression strategy was selected to assess if systematic regression model trends occurred based on the proximity of the analyzed data to $\Delta f_S = 0$.

Regression results for the Δf_S randomized and sorted sampling strategies can be seen in Figures Figure 16 and Figure 17, respectively. Specifically, regression coefficients for each element, p-values for each element, adjusted R^2 , and root mean square error for each regression iteration are presented. Note that the data presented in Figures Figure 16 and Figure 17 represent regression results prior to backward elimination, meaning that all elements were considered for each iteration.

In general, the regression coefficients were mostly constant for each element when randomized sampling was used. Conversely, the coefficients for certain elements varied as a function of sample size when sorted sampling was used. For example, the regression coefficient for C ranged from 2-2.2 mole fraction/wt.% during random sampling and 0.2-2.2 mole fraction/wt.% during sorted sampling, suggesting that the C coefficient depends on how closely the data is distributed around $\Delta f_S = 0$. Similar behavior was observed for Cr, Ni, Mo, N, and Cu. The coefficients for Ti, V, and Co also showed variability in their fitted tendency to stabilize austenite or ferrite, where both positive and negative regression coefficients were observed during sorted sampling.

A recurring theme during multiple regression analysis of the Δf_S solidification parameter was that the significance levels for certain elements were unstable. This was particularly true for Nb, Ti, V, and Co, where the p-values varied widely and were statistically insignificant for most regression iterations using the randomized and sorted sampling strategies. Mn and Si were statistically insignificant for all iterations using

randomized sampling, while they were stable for most of the sorted sampling iterations at intermediate sample sizes. The remaining elements (Cr, Mo, Ni, C, N, and Cu) were either always statistically significant or significant for most iterations using both sampling strategies.

The goodness-of-fit for each regression model can be considered by observing the adjusted R^2 values. The adjusted R^2 represents the amount of variance in Δf_S that is explained by the regression model parameters. As can be seen in Figure 16, the adjusted R^2 for the randomized sampling strategy is nearly constant at 0.74 and does not vary as a function of sample size. As seen in Figure 17, the adjusted R^2 during sorted sampling shows a sharp increase when the sample size is increased from 10-30% of the population, stabilizes near 0.8 for 40-80% of the population, and subsequently decreases.

The root mean square error indicates the standard deviation of the residuals for a given regression model. As seen in Figure 16, the root mean square error for randomized sampling of the Δf_S solidification parameter was nearly constant at 0.3 mole fraction. For sorted sampling shown in Figure 17, the root mean square error was approximately linear and ranged from 0.1-0.15 mole fraction/wt.% from 10-80% of the sample population. The root mean square error nearly doubled over the final 20% of the population using the sorted sampling strategy.

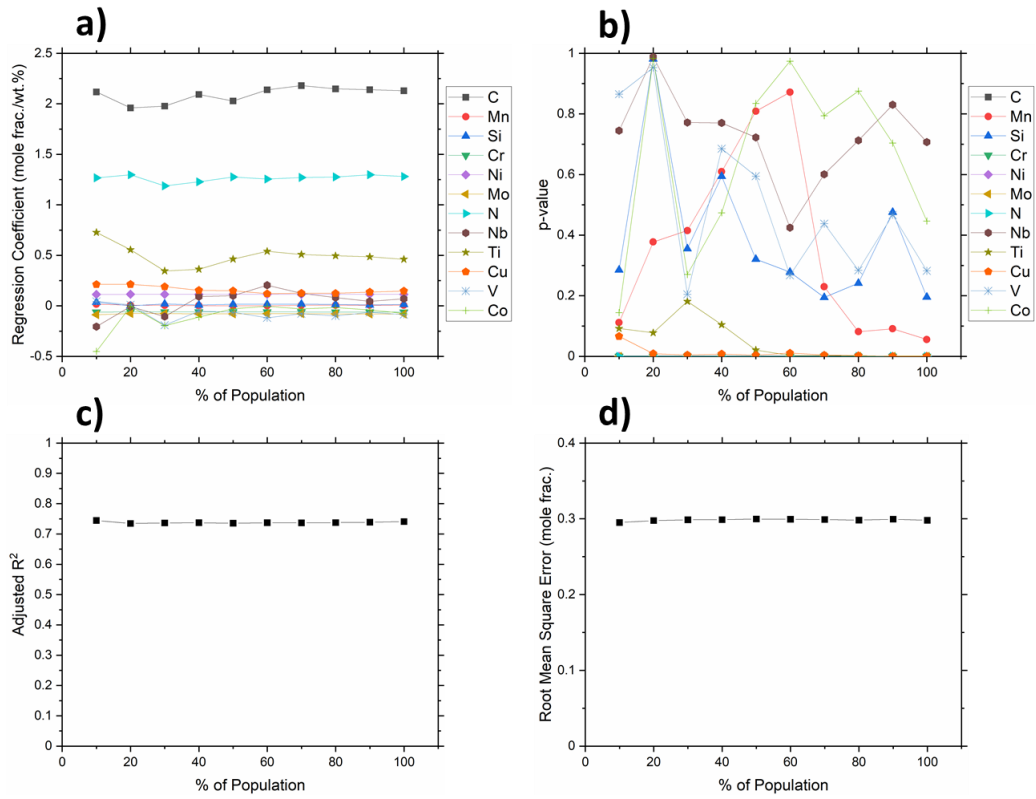


Figure 16: Regression analysis parameters as a function of sample size for the randomized Δf_s data; a) regression coefficients; b) p-values; c) adjusted R^2 ; d) root mean square error

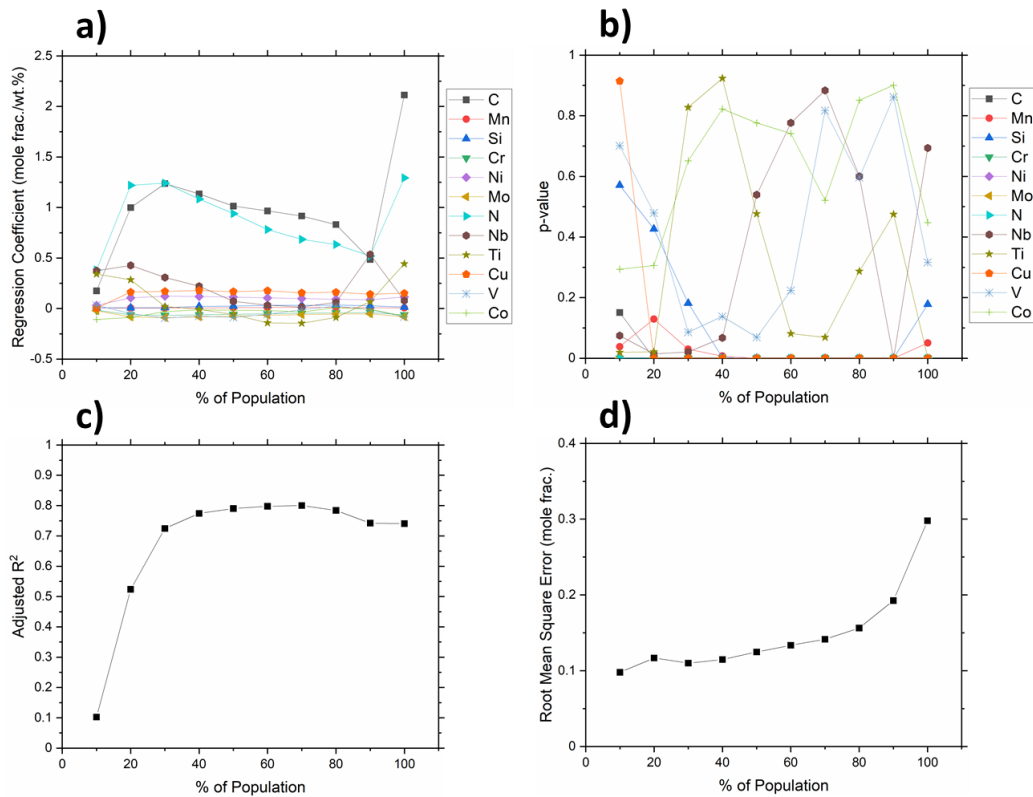


Figure 17: Regression analysis parameters as a function of sample size for the sorted Δf_s data; a) regression coefficients; b) p-values; c) adjusted R²; d) root mean square error

Analysis of the regression residuals revealed that every iteration of randomized regression resulted in a distribution that was not normally distributed. Conversely, sorted regression iterations with less than 100% of the database population showed more normally distributed residuals. This behavior can be seen in Figure 18, where residuals histograms are presented for 10%, 50%, and 100% of the sample population regression models from both the randomized and sorted sampling strategies. The randomized population residuals show nearly identical distributions and are scaled by the number of samples contained

within a given subset of the population. For the sorted regression iterations, the distributions for 10% of the population and 50% of the population are nearly identical and scaled by the number of samples considered. The 100% residuals data for both sampling strategies are identical since they were both constructed using the full database.

Analysis of the 100% population regression model revealed that considerable error was introduced by the inclusion of data points at the far ends of the Δf_S parameter. Given the way in which the Δf_S was defined, fully ferritic solidification resulted in $\Delta f_S = -0.99$ mole fraction and fully austenitic solidification resulted in $\Delta f_S = 0.99$ mole fraction. As a result, instances of single mode solidification result in a scenario where chemical composition can vary but Δf_S is constant. The effect of including single mode solidification in the regression analysis can be seen in Figure 17, where there is a sharp change in some regression coefficients, a decrease in adjusted R^2 , and sharp increase in root mean square error when the full database is considered. Randomized regression results do not show this effect because instances of single mode solidification are randomly distributed throughout each subset of the database. Instead, each iteration of randomized regression showed behavior similar to when 100% of the database was considered.

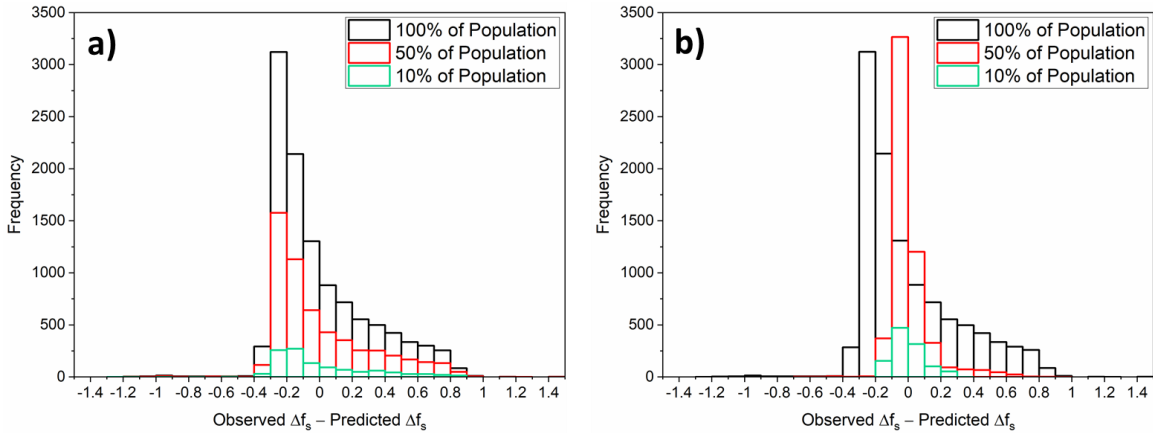


Figure 18: Histogram of the regression residuals for 10%, 50%, and 100% of the Δf_s data; a) randomized sampling; b) sorted sampling

Cr_{eq} and Ni_{eq} expressions were developed using backward elimination multiple regression for each of the iterations discussed previously for the Δf_s parameter. Randomized sampling resulted in nearly constant Cr_{eq} and Ni_{eq} expressions across all iterations. The randomized sampling data will not be considered further due to the errors introduced by single mode solidification. The following observations were made for the Cr_{eq} and Ni_{eq} expressions that were developed using the sorted Δf_s regression data for subsets of the full database:

- Mo was a ferrite stabilizer and had a constant coefficient of 1.3
- C was an austenite stabilizer and had coefficients that were stable around approximately 9
- N was an austenite stabilizer and had coefficients that displayed a dependence on sample size, where higher coefficients were observed closer to $\Delta f_s = 0$; N

coefficients ranged from 12-6 and were most stable at intermediate subsets of the database

- Cu was an austenite stabilizer with consistent coefficients near 1.5
- Mn was a weak austenite stabilizer with a coefficient near 0.1 for most iterations
- Si appears as an austenite stabilizer with a coefficient near 0.2-0.3 for intermediate subsets of the database
- No other elements were considered due to a lack of statistical significance during regression analysis

The final Cr_{eq} and Ni_{eq} expressions based on the Δf_S solidification parameter were extracted from the regression model that was developed using a sorted sampling strategy with 50% of the database population. This regression model was selected because adjusted R^2 was nearly maximized, root mean square error was low, and coefficients within the Cr_{eq} and Ni_{eq} expressions were stable when intermediate subsets of the population were evaluated. The final Cr_{eq} and Ni_{eq} expressions for the Δf_S solidification parameter are presented as:

$$Cr_{eq}^{\Delta f_S} = Cr + 1.3Mo$$

$$Ni_{eq}^{\Delta f_S} = Ni + 9C + 8N + 1.5Cu + 0.1Mn + 0.2Si$$

Stable and Metastable Equilibria

The stable/metastable equilibria ΔT_L model data was processed in the same fashion as the Δf_S data. This included using both randomized and sorted sampling strategies. For

the sorted sampling strategy, the data was arranged by $|\Delta T_L|$ in ascending order and partitioned in 10% increments of the total sample population. Multiple regression iterations were performed as a function of the percentage of the total database population for the randomized and sorted sampling strategies.

Regression results for the randomized and sorted ΔT_L sampling strategies can be seen in Figures Figure 19 and Figure 20, respectively. The regression coefficients for each element, p-values for each element, adjusted R^2 , and root mean square error for each regression iteration are presented. Again, the data presented in Figures Figure 19 and Figure 20 represents regression results prior to backward elimination to observe trends for all elements as functions of sampling strategy and sample size.

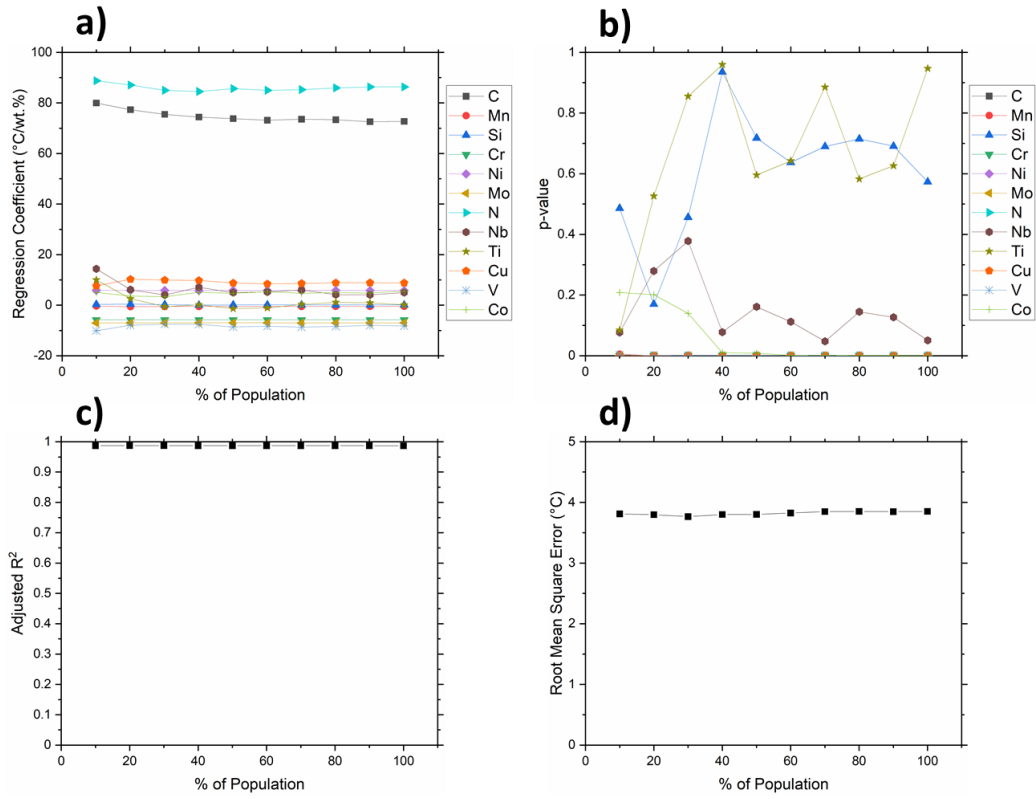


Figure 19: Regression analysis parameters as a function of sample size for the randomized ΔT_L data; a) regression coefficients; b) p-values; c) adjusted R^2 ; d) root mean square error

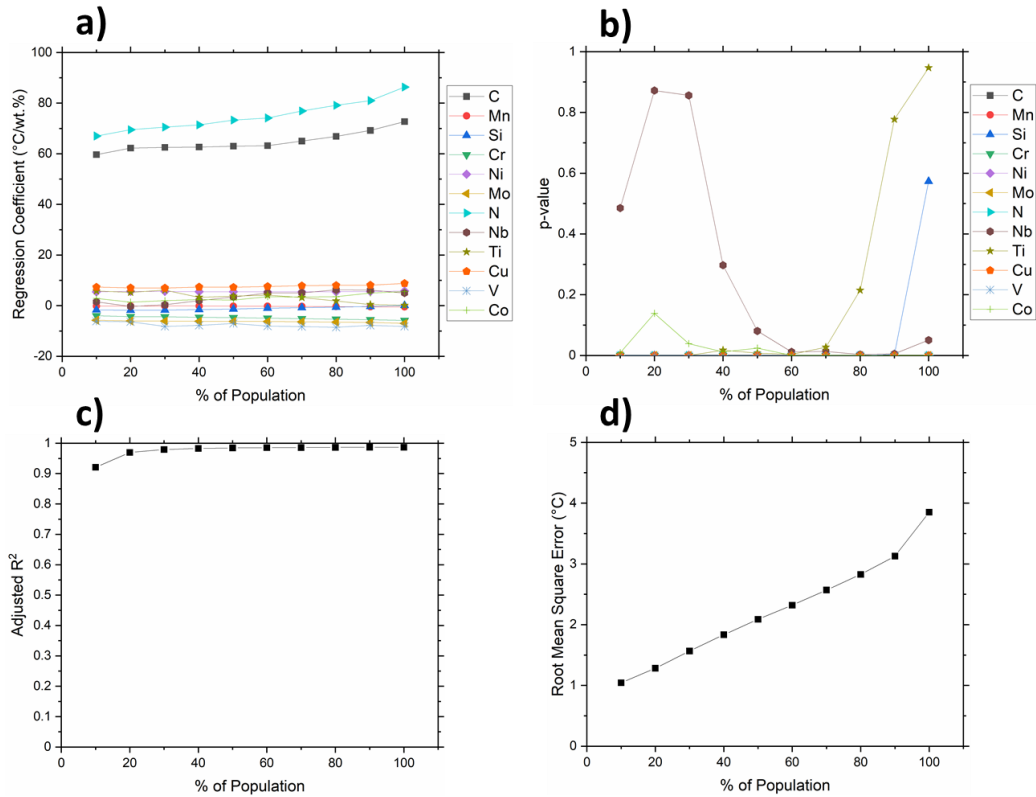


Figure 20: Regression analysis parameters as a function of sample size for the sorted ΔT_L data; a) regression coefficients; b) p-values; c) adjusted R^2 ; d) root mean square error

The regression coefficients for randomized subsets of the ΔT_L population were mostly stable for all iterations and elements. This behavior mimics what was observed during regression analysis of the Δf_S parameter. While a slight decrease in the regression coefficients as a function of sample size can be seen in Figure 19 for C and N, the Ni regression coefficient also decreased proportionally. This indicates that the coefficients for C and N in a Ni_{eq} expression would be constant after normalization for the randomized regression iterations. Unlike the Δf_S case, the sorted regression coefficient results were also quite stable as the percentage of the database that was considered was increased.

Inconsistent behavior was observed for the statistical significance of Nb, Ti, Co, and Si during regression analysis. Ti and Si were never statistically significant with p-values always greater than 0.05 during randomized regression. Ti was also only statistically significant when 70% or less of the database was evaluated during sorted regression. Si was significant for all iterations of sorted regression except for when the full sample population was evaluated. Only one instance of statistical significance was observed for Nb during randomized regression. Nb was also only significant when 60-90% of the sample population was evaluated with the sorted sampling strategy. Co was statistically significant when 40% or more of the randomized sample population was evaluated and for most cases when the database was sorted. All other elements had p-values less than 0.05 for all iterations of randomized and sorted sampling and were therefore statistically significant.

The overall variance explained by each ΔT_L regression model was higher than what was observed with the Δf_S regression models. Comparing the adjusted R^2 values presented in Figures Figure 19 and Figure 20, the adjusted R^2 values for all ΔT_L regression models were above 0.9. A slight increase in adjusted R^2 was observed between 10-30% of the sorted ΔT_L sample population where the value raised from approximately 0.92 to above 0.98. Comparing a similar range of 10-30% for the sorted Δf_S parameter, the adjusted R^2 increased from 0.1-0.72. The adjusted R^2 values suggest that the ΔT_L parameter can be more effectively linearized than the Δf_S parameter.

Similar trends were observed when comparing the root mean square error of ΔT_L and Δf_S regression models. In both cases, randomized sampling resulted in a constant root

mean square error and sorted sampling resulted in an increase in root mean square error with an increase in sample size. For sorted sampling of ΔT_L , the root mean square error was linearly proportional to sample size across 10-90% of the database population and ranged from approximately 1-3°C. A sharp increase was observed from 90-100% of the population where the root mean square error increased from approximately 3°C to 4°C.

Residuals analysis of the ΔT_L regression models revealed that the variance for most elements was constant with an average near zero as a function of concentration regardless of the sampling strategy that was used. Notable exceptions include the partial residuals for Cr and Ni as shown in Figure 21. The apparent bias in variance for Cr and Ni suggests that curvature effects may be significant for these elements with respect to ΔT_L across the concentration ranges that were considered. Histograms of the regression residuals are presented in Figure 22 for 10%, 50%, and 100% of the sample population regression models for both the randomized and sorted sampling strategies. Like the Δf_S regression models, all instances of randomized sampling and the 100% database case resulted in residuals that were not normally distributed or centered on zero. Conversely, when subsets of the database were considered after sorting by $|\Delta T_L|$ the residuals were more normally distributed and centered on zero.

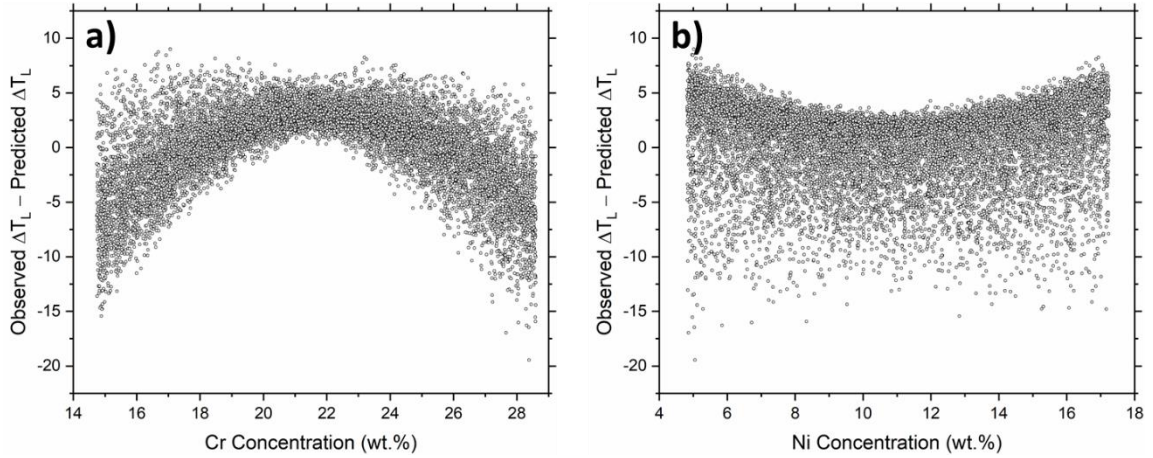


Figure 21: Partial residuals plots for the regression model that was constructed using 100% of the ΔT_L data; a) Cr; b) Ni

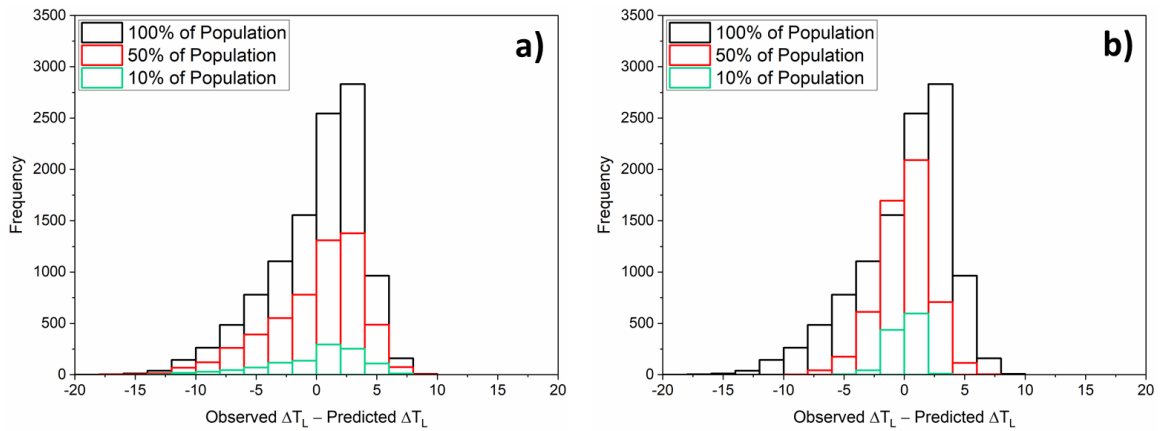


Figure 22: Histogram of the regression residuals for 10%, 50%, and 100% of the ΔT_L data; a) randomized sampling; b) sorted sampling

Cr_{eq} and Ni_{eq} expressions were developed using backward elimination multiple regression for each of the iterations discussed previously for the ΔT_L parameter. Randomized sampling resulted in nearly constant Cr_{eq} and Ni_{eq} expressions across all

iterations. The randomized sampling data will not be considered further due to the errors introduced by single mode solidification. The following observations were made for the Cr_{eq} and Ni_{eq} expressions that were developed using the sorted ΔT_L regression data for subsets of the full database:

- Mo was a ferrite stabilizer with coefficients that ranged from 1.4-1.2 as sample size increased
- Si was a ferrite stabilizer with coefficients that ranged from 0.4-0.1 as sample size increased
- Mn was a weak ferrite stabilizer with coefficients that ranged from 0.03-0.08 as sample size increased
- C was an austenite stabilizer with coefficients that ranged from 11-12 as sample size increased
- N was an austenite stabilizer with coefficients that ranged from 12-15 as sample size increased
- Cu was an austenite stabilizer with coefficients that ranged between 1.2-1.5 as sample size increased
- Nb, Ti, Co, and V were ignored due to inconsistencies with respect to statistical significance in the ΔT_L regression models, large standard errors relative to their regression coefficients, and the fact that their maximum concentrations in the database were quite low

The Cr_{eq} and Ni_{eq} expressions that were derived using 50% of the sorted ΔT_L population were selected to move forward. The 50% expressions were selected because

they represented the approximate average behavior for all the elements that were considered. Additionally, the adjusted R^2 was stable and regression residuals were normally distributed about zero. The ΔT_L Cr_{eq} and Ni_{eq} expressions are presented as:

$$Cr_{eq}^{\Delta T_L} = Cr + 1.3Mo + 0.3Si + 0.04Mn$$

$$Ni_{eq}^{\Delta T_L} = Ni + 12C + 13N + 1.3Cu$$

As mentioned previously, the partial residuals for Cr and Ni during multiple regression of the ΔT_L parameter consistently showed bias that suggested curvature may be important for these elements. As such, regression analysis was repeated using the ΔT_L database with added independent variable terms for Cr^2 and Ni^2 . The same regression process was used where randomized and sorted sampling strategies were implemented.

Regression results for the randomized and sorted ΔT_L sampling strategies including curvature terms for Cr and Ni can be seen in Figures Figure 23 and Figure 24, respectively. The regression coefficients for each element, p-values for each element, adjusted R^2 , and root mean square error for each regression iteration are presented. The data presented in Figures Figure 23 and Figure 24 represent regression results prior to backward elimination.

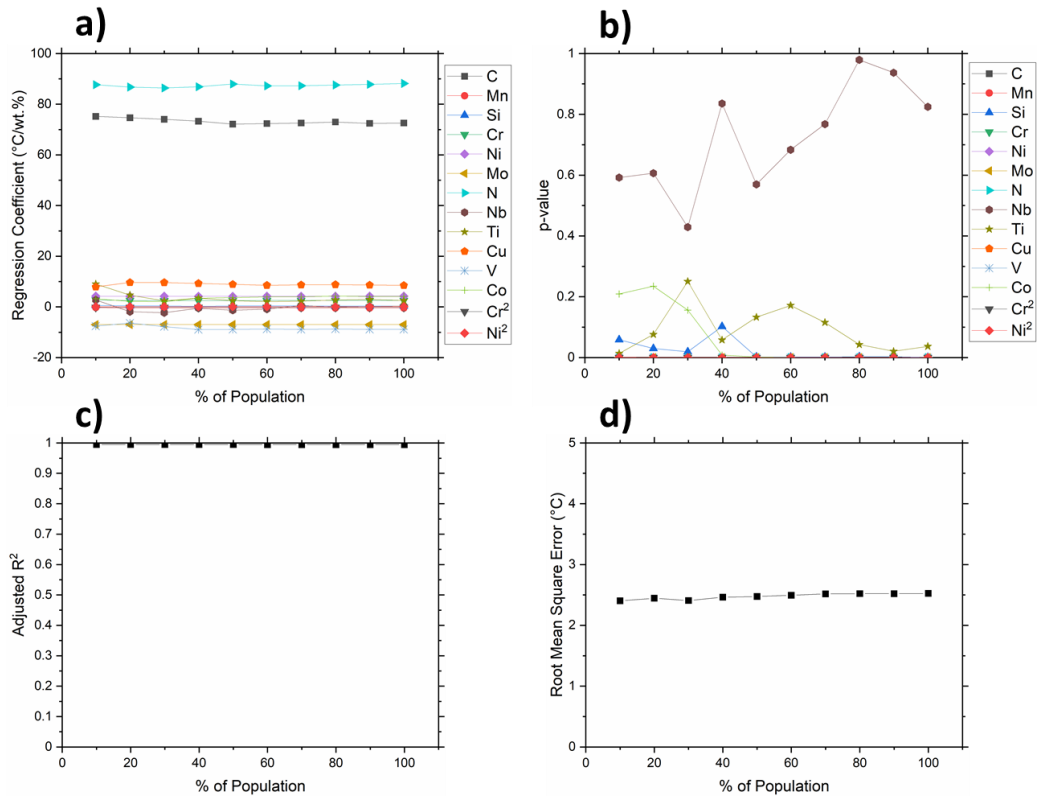


Figure 23: Regression analysis parameters as a function of sample size for the randomized ΔT_L data with squared terms for Cr and Ni; a) regression coefficients; b) p-values; c) adjusted R^2 ; d) root mean square error

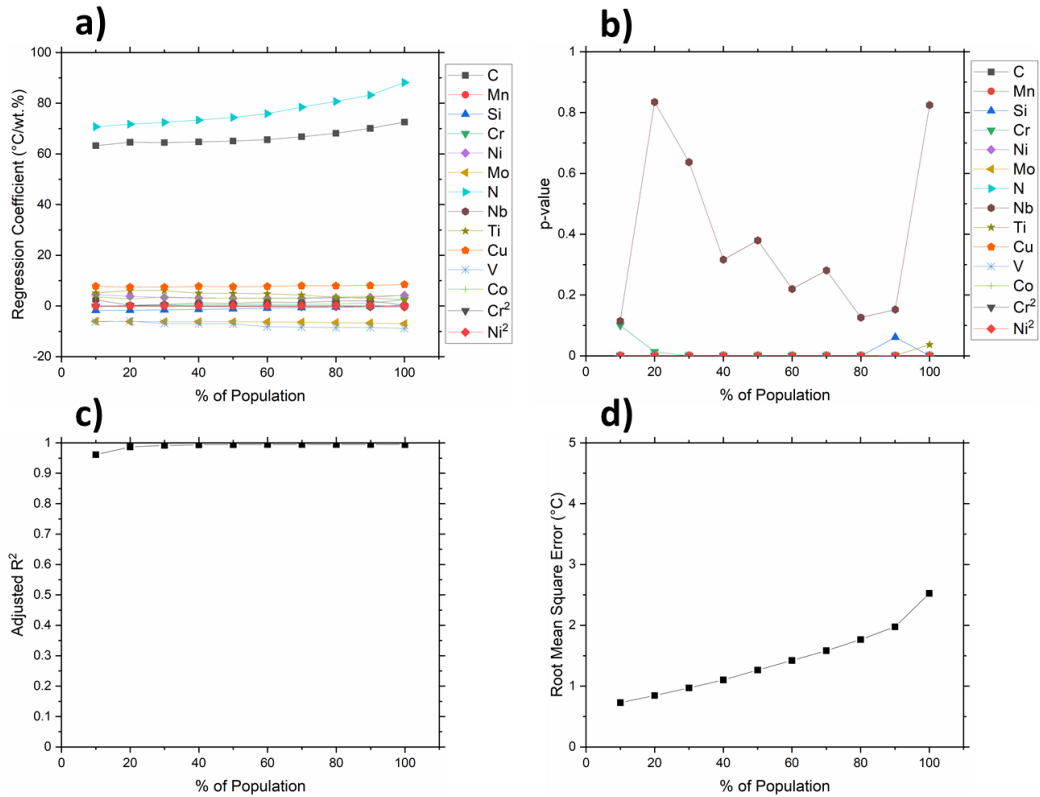


Figure 24: Regression analysis parameters as a function of sample size for the sorted ΔT_L data with squared terms for Cr and Ni; a) regression coefficients; b) p-values; c) adjusted R^2 ; d) root mean square error

In general, the ΔT_L regression results when curvature terms are included for Cr and Ni are similar to those that were developed without the curvature terms. Inconsistencies with respect to the statistical significance of Nb, Ti, Co, and Si were still observed. Additionally, the trends in regression coefficient values were consistent between the analysis with and without square terms. The inclusion of Cr^2 and Ni^2 as independent variables resulted in a consistent decrease in the root mean square error when compared to

the strictly linear ΔT_L regression results. The decrease in root mean square error can be seen by comparing Figure 19 and Figure 23, where the inclusion of square terms reduced the root mean square error by approximately 1.5°C.

The bias in the partial residuals for Cr and Ni were eliminated as seen by comparing Figure 21 and Figure 25. Although the inclusion of square terms eliminated the curvature of the partial residuals plots for Cr and Ni, the variance was still not constant as seen by the bowtie shape in Figure 25, where the largest variance occurs at the far ends of each concentration range. By eliminating curvature of the partial residuals for Cr and Ni, the residuals were also more normally distributed for both the randomized and sorted sampling strategies as seen in Figure 26.

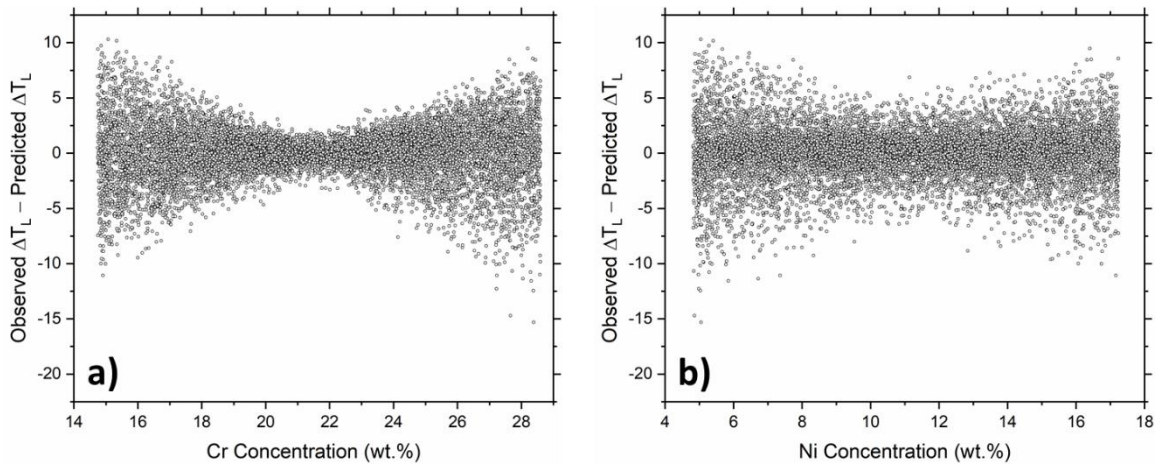


Figure 25: Partial residuals plots for the regression model that was constructed using 100% of the ΔT_L data with squared terms for Cr and Ni; a) Cr; b) Ni

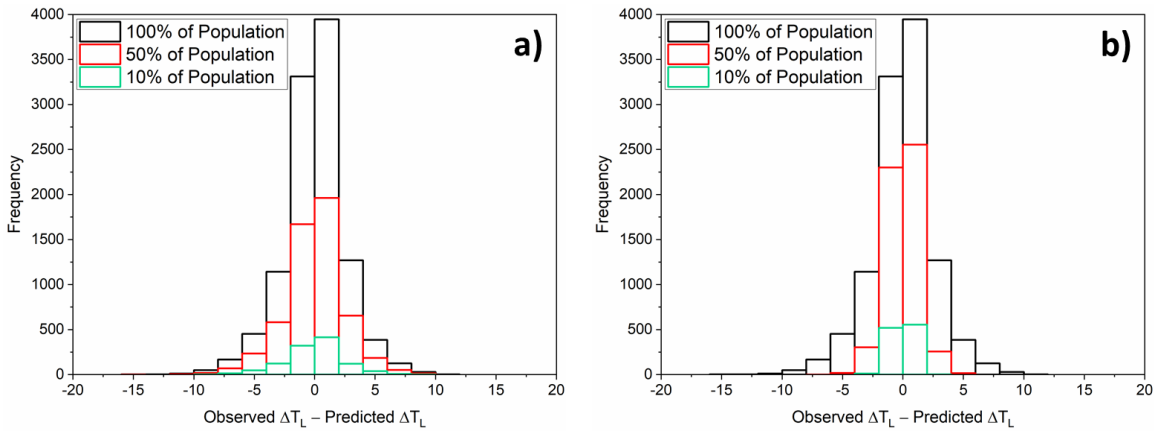


Figure 26: Histogram of the regression residuals for 10%, 50%, and 100% of the ΔT_L data with squared terms for Cr and Ni; a) randomized sampling; b) sorted sampling

Backward elimination regression was used to derive a second set Cr_{eq} and Ni_{eq} expressions based on the ΔT_L parameter that included terms for Cr^2 and Ni^2 . The Cr_{eq} and Ni_{eq} expressions that were developed using a randomized sampling strategy were constant. However, sorted sampling resulted in large changes in the equivalency coefficients as a function of the ΔT_L subpopulation that was considered. This was particularly true for the Cr_{eq} coefficients. The following observations were made for the sorted equivalency coefficients that included second order terms for Cr and Ni for subsets of the ΔT_L database:

- Cr^2 was a ferrite stabilizer with coefficients ranging from 0.5-0.1 as sample size increased
- Mo was a ferrite stabilizer with coefficients ranging from 31-6 as sample size increased
- Si was a ferrite stabilizer when 10-80% of the population was evaluated with coefficients ranging from 9-0.5 as sample size increased

- Mn was a ferrite stabilizer with coefficients ranging from 1-0.4 as sample size increased
- Ni² was an austenite stabilizer with coefficients ranging from 0.01-0.04; a maximum was observed when 70% of the population was evaluated
- C was an austenite stabilizer with coefficients ranging from 14-22; a maximum was observed when 70% of the population was evaluated
- N was an austenite stabilizer with coefficients ranging from 16-26; a maximum was observed when 70% of the population was evaluated
- Cu was an austenite stabilizer with coefficients ranging from 1.7-2.6; a maximum was observed when 70% of the population was evaluated
- Again, Nb, Ti, Co, and V were ignored due to inconsistencies with respect to statistical significance in the ΔT_L regression models, large standard errors relative to their regression coefficients, and the fact that their maximum concentrations in the database were quite low

As seen, the equivalency coefficients for ferrite stabilizers varied widely. Examination of the multiple regression equation results indicated that the variability was associated with the Cr regression coefficient which varied from 0.2-1 °C/wt.% with an increasing sample size. The normalization for Cr_{eq} resulted in large changes for the ferrite stabilizing coefficients. The regression coefficients for Cr² and Mo were generally consistent as indicated by the approximate decrease in their Cr_{eq} coefficients by a factor of 5 due to the 5x increase in the Cr regression coefficient. The Cr_{eq} coefficients for Si and Mn decreased by factors of approximately 18 and 2, respectively, because their regression

coefficients varied as a function of the sorted ΔT_L sample size. Less variability in the Ni_{eq} coefficients was observed, and the changes were reflected by changes in the Ni regression coefficient that was used for normalization. Similar to the equivalencies that were selected for Δf_S and ΔT_L with no curvature terms, the sorted sampling regression equivalencies that included Cr^2 and Ni^2 for 50% of the database population were selected. The 50% equivalencies were selected because they represented the approximate average behavior for all the elements that were considered. The ΔT_L equivalencies that include curvature for Ni and Cr are presented as:

$$Cr_{eq}^{\Delta T_{L,2}} = -Cr + 0.24Cr^2 + 11Mo + 3Si + 0.4Mn$$

$$Ni_{eq}^{\Delta T_{L,2}} = Ni + 0.03Ni^2 + 21C + 24N + 2Cu$$

The above forms of $Cr_{eq}^{\Delta T_{L,2}}$ and $Ni_{eq}^{\Delta T_{L,2}}$ lead to values that are unconventional when compared to strictly linear equivalency expressions. For example, consider a ternary Fe-20Cr-10Ni (wt.%) austenitic stainless steel chemistry. In a strictly linear set of equivalency expressions the Cr and Ni values would relate 1:1 to Cr_{eq} and Ni_{eq} , respectively. Considering the same Fe-20Cr-10Ni alloy in the $Cr_{eq}^{\Delta T_{L,2}}$ and $Ni_{eq}^{\Delta T_{L,2}}$ expressions would result in equivalencies of 76 and 13, respectively. As written, the inclusion of squared terms for Cr and Ni in the equivalency expressions would only provide a 1:1 relationship for two sets of Cr and Ni concentrations. Specifically, they would be equal at Fe-0Ni-0Cr and Fe-0Ni-8.3Cr. Therefore, it seems appropriate to independently scale $Cr_{eq}^{\Delta T_{L,2}}$ and $Ni_{eq}^{\Delta T_{L,2}}$ by constants that will shift the concentrations to a space that is more sensible with

respect to austenitic stainless steel weld metals. For this purpose, scaling $Cr_{eq}^{\Delta T_{L,2}}$ by a factor of 1/3.8 and $Ni_{eq}^{\Delta T_{L,2}}$ by a factor of 1/1.3 shifts the equivalencies so that a Fe-20Cr-10Ni alloy will have equivalencies and concentrations that match 1:1. The adjusted equivalencies after applying these scaling factors can be written as:

$$Cr_{eq}^{\Delta T_{L,2}} = \frac{-Cr + 0.24Cr^2 + 11Mo + 3Si + 0.4Mn}{3.8}$$

$$Ni_{eq}^{\Delta T_{L,2}} = \frac{Ni + 0.03Ni^2 + 21C + 24N + 2Cu}{1.3}$$

Comparison of Cr_{eq}/Ni_{eq}

The new equivalency relationships were applied to a collection of experimental data from the literature to determine their ability to differentiate between primary austenite and primary ferrite solidification. The experimental data consisted of the WRC Appendix II database and data extracted from additional studies that reported chemical composition and solidification mode for a series of stainless steel weld metals [5, 12, 13, 80, 81]. A total of 130 individual samples were included in the analysis. All of the samples fell within the designed concentration limits for the Theoretical WRC database. To assess the effectiveness of each set of equivalencies, Cr_{eq}/Ni_{eq} was calculated for each sample as this is frequently used as an indicator for primary solidification mode in stainless steels. The Cr_{eq}/Ni_{eq} data was then partitioned by the observed solidification mode for each sample, where samples were grouped as primary austenite, mixed, and primary ferrite solidification modes. The Cr_{eq}/Ni_{eq} distributions for each solidification mode were then plotted to assess

how much overlap existed between the solidification mode data sets for a given set of equivalencies. The Cr_{eq}/Ni_{eq} distribution data are presented in Figure 27. Figure 27 contains Cr_{eq}/Ni_{eq} distribution data using the WRC-1988 [4], Hammar and Svensson [29], Δf_S , ΔT_L , and $\Delta T_{L,2}$ with curvature terms for Cr and Ni ($\Delta T_{L,2}$) equivalencies. Each set of equivalency relationships are also presented in Figure 27 for reference.

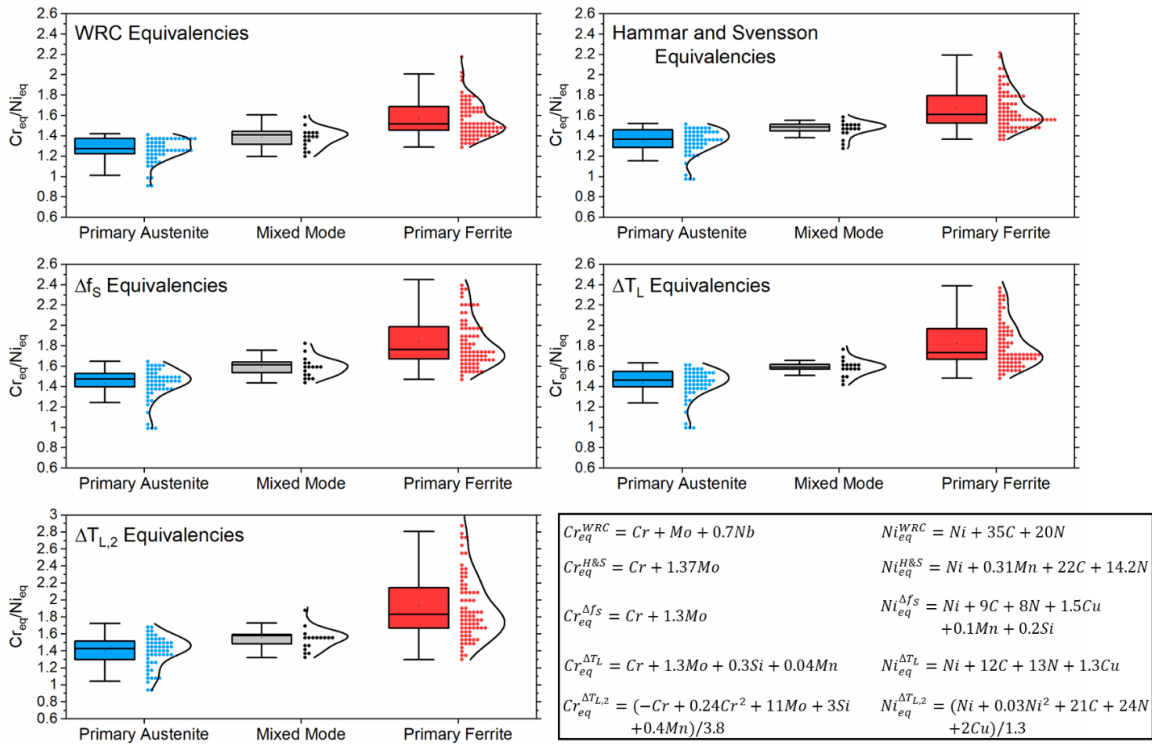


Figure 27: Cr_{eq}/Ni_{eq} distributions for primary austenite, mixed mode, and primary ferrite solidification using the WRC, Hammar and Svensson, Δf_S , ΔT_L , and $\Delta T_{L,2}$ equivalencies

As seen in Figure 27, overlap exists between the primary austenite and primary ferrite Cr_{eq}/Ni_{eq} distributions for each set of equivalencies. The limited number of mixed

mode solidification samples always occurred in the transition between primary austenite and primary ferrite solidification. To quantitatively evaluate the extent of overlap between the Cr_{eq}/Ni_{eq} distributions for primary austenite and primary ferrite solidification, the difference between the maximum austenite Cr_{eq}/Ni_{eq} and minimum ferrite Cr_{eq}/Ni_{eq} was calculated for each set of equivalencies. From the smallest to largest difference between the maximum austenite Cr_{eq}/Ni_{eq} and minimum ferrite Cr_{eq}/Ni_{eq} , the equivalencies ranked as follows: WRC (0.133), ΔT_L (0.149), Hammar and Svensson (0.155), Δf_S (0.177), and $\Delta T_{L,2}$ (0.423). Additionally, the total number of samples that fell within the maximum austenite Cr_{eq}/Ni_{eq} and minimum ferrite Cr_{eq}/Ni_{eq} overlapped region were counted for each set of equivalencies. Ignoring the mixed mode solidification data, the following number of samples fell within the overlapped primary austenite and primary ferrite distributions for each set of equivalencies: WRC (35), ΔT_L (35), Hammar and Svensson (43), Δf_S (39), and $\Delta T_{L,2}$ (56).

Based on the maximum overlap metric, the WRC equivalencies provided the best separation between primary austenite and primary ferrite solidification for the analyzed dataset. However, the number of data points contained within the overlapped distributions was the same using the WRC and ΔT_L equivalencies. This suggests that although the WRC and ΔT_L equivalencies are quite different, especially with respect to C and N, that their ability to differentiate between primary solidification modes is similar for the analyzed data set. Additionally, the high coefficients for C and N in the WRC Ni_{eq} expression have the effect of shifting the Cr_{eq}/Ni_{eq} distributions to lower values. This can be seen by comparing

the location of the primary ferrite and primary austenite distributions along the vertical axis of Figure 27 for the WRC and ΔT_L distributions.

Although the $\Delta T_{L,2}$ equivalencies exhibited the largest range between the maximum austenite Cr_{eq}/Ni_{eq} and minimum ferrite Cr_{eq}/Ni_{eq} , the results are not directly comparable with the strictly linear equivalency relationships. The scaling factors for the $\Delta T_{L,2}$ equivalencies were based on the ternary Fe-20Cr-10Ni stainless steel composition which falls within a range of practical interest for austenitic stainless steel weld metals. Although the $\Delta T_{L,2}$ scaling factors shift Cr_{eq} and Ni_{eq} results toward values that are more familiar to the scientific community, the selection of the Fe-20Cr-10Ni system to define those factors was somewhat arbitrary. Selecting a different chemical composition for the scaling exercise would shift the range between the maximum austenite Cr_{eq}/Ni_{eq} and minimum ferrite Cr_{eq}/Ni_{eq} . Specifically, raising Ni_{eq} values by using a lower scaling factor or lowering Cr_{eq} by using a larger scaling factor would artificially decrease the Cr_{eq}/Ni_{eq} range where the primary austenite and primary ferrite distributions overlap, but the same number of data points would still be contained within the overlapped distributions. Additionally, the inclusion of squared terms for Cr and Ni make the Cr_{eq}/Ni_{eq} ratio quite sensitive to the coefficients for these elements. In the current $\Delta T_{L,2}$ expression, this is particularly true for Cr where the Cr^2 equivalency coefficient causes Cr_{eq} values to nonlinearly “stretch” along the Cr_{eq}/Ni_{eq} axis. Another way to think about this effect is to consider a predictive diagram similar to the WRC-1988 diagram with the $\Delta T_{L,2}$ Cr_{eq} and Ni_{eq} expressions presented on the horizontal and vertical axes, respectively. By preferentially stretching the sample data along the Cr_{eq} axis it will extend the Cr_{eq}/Ni_{eq} values which bracket the transition between

primary austenite and primary ferrite solidification. That's not to say that the $\Delta T_{L,2}$ Cr_{eq} and Ni_{eq} expressions are not capable of differentiating between primary austenite and primary ferrite solidification modes, but rather that the commonly used Cr_{eq}/Ni_{eq} metric is inherently flawed in this analysis when squared terms are included for Cr and Ni.

Although the Δf_S equivalencies provided the widest range of Cr_{eq}/Ni_{eq} across the overlapped primary austenite and primary ferrite distributions, they performed better than the Hammar and Svensson equivalencies with respect to reducing the number of samples contained within that same range. Conversely, the Δf_S equivalencies performed worse than the WRC and ΔT_L equivalencies using the same assessment.

To investigate which particular element / equivalency coefficient pairs were associated with the overlapped distributions in Figure 27, the chemical compositions for each sample within the overlapped primary austenite and primary ferrite Cr_{eq}/Ni_{eq} distributions were analyzed for each set of equivalencies. The trends in the concentration data were quite similar across all equivalencies. The average Mn and Si concentrations in both austenite and ferrite were essentially constant for all equivalencies. This implies that the Mn and Si concentrations had no bearing on the Cr_{eq}/Ni_{eq} distributions for the analyzed dataset, regardless of whether they appeared in the Cr_{eq} expression, Ni_{eq} expression, or were completely omitted. Cu appeared to have little-to-no effect on the predictive ability of the equivalency expressions, although this effect is inconclusive since only nine of the samples had reported values for Cu and their reported concentrations only ranged between 0.13-0.22 wt.% within the primary austenite and primary ferrite datasets. Mo consistently showed an above average concentration for primary austenite and a below average

concentration for primary ferrite. C showed a consistent trend where average austenite concentrations were always lower than average ferrite concentrations. N showed mixed behavior. The WRC equivalencies favored low N concentrations in austenite and high concentrations in ferrite, the Hammar and Svensson and $\Delta T_{L,2}$ equivalencies were neutral with respect to N, and the Δf_S and ΔT_L equivalencies showed high concentrations in austenite and low concentrations in ferrite. Per this analysis, Mo, C and N are the primary elements other than Cr and Ni which controlled the Cr_{eq}/Ni_{eq} distributions for the analyzed dataset.

The data presented in Figure 27 also highlights the fact that a defining a constant Cr_{eq}/Ni_{eq} to differentiate between primary austenite and primary ferrite solidification may not be broadly applicable. First, the Cr_{eq}/Ni_{eq} distributions for the analyzed solidification mode datasets demonstrate that overlap exists between primary austenite and primary ferrite solidification, and that mixed mode solidification can occur within that overlap for each set of equivalencies. Further, Cr_{eq}/Ni_{eq} distributions are sensitive to the equivalencies used, meaning that the transition between primary austenite and primary ferrite shifts depending on which equivalencies are selected.

Conclusions

The following conclusions can be made from efforts to develop composition equivalency relationships for austenitic stainless steel weld metals using CALPHAD-based modeling:

- Computational thermodynamic calculations for the primary solidification mode of austenitic stainless steel weld metals were not in agreement with experimental evidence in all cases. The discrepancies between thermodynamic calculations and experimental results were isolated to chemical compositions near the experimentally determined primary austenite / primary ferrite solidification mode transition. Specifically, computational thermodynamic calculations predicted that alloys near the transition would solidify as primary ferrite, while experimental data showed that alloys solidify as primary austenite.
- Two new solidification model parameters have been explored that relate to the solidification sequence of austenitic stainless steel weld metals. The first parameter, Δf_s , utilized Scheil solidification assumptions to determine the proximity of stainless steel weld metal chemistries to the intersection of the equilibrium austenite and ferrite liquidus surfaces. The second parameter, ΔT_L , utilized stable and metastable liquidus temperature calculations to determine the proximity of stainless steel weld metal chemistries to the intersection of the equilibrium austenite and ferrite liquidus surfaces.
- A process has been established using randomized stainless steel chemistries, high-throughput thermodynamic calculations, and multiple regression to derive new equivalency expressions to predict primary solidification mode in austenitic stainless steels weld metals. It was found that the Δf_s parameter was not well suited for multiple regression analysis when chemical compositions displaying single phase solidification were included in the analysis. The ΔT_L parameter, however,

was more effectively fit using multiple regression. The inclusion of curvature terms for Cr and Ni in the multiple regression analysis of the ΔT_L parameter improved the overall goodness-of-fit and eliminated bias in the regression residuals.

- Certain elements were consistently unstable during regression analysis and displayed a sensitivity to sample size and/or the proximity of the sample set to the equilibrium austenite / ferrite transition. Specifically, Nb, Ti, V, and Co displayed this behavior. The inconsistent behavior for these elements was attributed to their low maximum concentrations within the analyzed database.
- The newly defined linear ΔT_L Cr_{eq} and Ni_{eq} expressions performed similar to experimentally derived relationships from the literature for differentiating primary solidification mode via the Cr_{eq}/Ni_{eq} metric. This suggests that the methods employed here to generate the requisite data and derive equivalencies based on computational thermodynamic calculations can offer an advantage over strictly experimental assessments that are both time consuming and costly.
- The inclusion of curvature terms for Cr and Ni in the ΔT_L Cr_{eq} and Ni_{eq} expressions reduced the ability to differentiate between primary austenite and primary ferrite via the Cr_{eq}/Ni_{eq} metric. Therefore, Cr_{eq}/Ni_{eq} should not be used when curvature terms for Cr and Ni are included in the analysis.

Chapter 4. Development of a CALPHAD-Based Primary Solidification Mode Diagram for Austenitic Stainless Steel Weld Metals

Introduction

In the previous chapter, high-throughput computational thermodynamic calculations and statistical analyses were used to develop new sets of Cr_{eq} and Ni_{eq} expressions to differentiate between primary austenite and primary ferrite solidification modes in austenitic stainless steel weld metals. The new equivalencies performed similar to traditional relationships that were developed solely using experimental data. Although these new equivalency relationships were capable of differentiating between primary solidification modes on the basis of Cr_{eq}/Ni_{eq} , the fact still remains that there is a range of stainless steel chemical compositions where computational thermodynamic calculations and experimental results are not in agreement. The disagreement between computational thermodynamic calculations and experimental observations exists for stainless steel chemistries that sit near the multicomponent austenite and ferrite liquidus surfaces. This behavior is exclusive to chemistries where equilibrium thermodynamics predicts that primary ferrite should be the active solidification mode.

Previous work has demonstrated that dendrite growth kinetics can cause metastable primary phase selection in steels [59, 64-66, 82]. Specifically, undercooling at the solidification front can stabilize austenite growth even when ferrite should form per equilibrium phase diagram predictions. Most commonly, this behavior is discussed for

solidification conditions where high growth velocities and high temperature gradients exist such as during laser or electron beam welding [62, 66, 83]. Work by Bobadilla has demonstrated that metastable austenite growth is not unique to high solidification velocities and temperature gradients, where metastable austenite selection was observed during controlled growth experiments at low solidification velocities in ternary Fe-Ni-Cr alloys [63, 64].

To build upon the predictive ability of the newly developed Cr_{eq} and Ni_{eq} expressions that were presented in the previous chapter, dendrite growth theory has been applied to develop a new predictive diagram for primary solidification mode in austenitic stainless steel weld metals. This effort provides a fundamental basis for constructing such a diagram rather than simply overlaying experimental solidification mode data onto a Cr_{eq} - Ni_{eq} chemistry space and manually drawing a primary austenite / primary ferrite boundary. Additionally, following this approach allows for modifications of the diagram to be made when dendrite growth kinetics change for a given application.

Dendrite Growth Theory

According to dendrite growth theory [68], the dendrite tip temperature can be written as:

$$T_d = T_L + \Delta T$$

where T_d is the dendrite tip temperature, T_L is the equilibrium liquidus temperature for the alloy, and ΔT is the amount of undercooling that occurs at the dendrite tip. The equilibrium

liquidus temperature term represents the composition-dependent thermodynamic response of the system, and the undercooling term represents the kinetic response of the system that is dependent on composition, solidification velocity, and temperature gradient at the solid-liquid interface. During constrained dendrite growth, i.e. when the temperature gradient in the liquid is positive, undercooling at the solid-liquid interface occurs mainly due to solute segregation and capillarity under conventional fusion welding conditions. By applying the dendrite tip temperature solution to austenite (γ) and ferrite (δ), the tip temperature solutions can be written independently as:

$$T_d^\gamma = T_L^\gamma + \Delta T^\gamma$$

and

$$T_d^\delta = T_L^\delta + \Delta T^\delta$$

By solving the dendrite tip temperature solutions for austenite and ferrite independently, a maximum growth temperature criterion can be applied where, for a given alloy chemistry, solidification velocity, and temperature gradient at the solid-liquid interface, the phase with the highest dendrite tip temperature will preferentially grow into the liquid. This condition serves as the basis for so-called interface response functions that have successfully been used to describe stable and metastable phase selection in solidifying austenitic stainless steel weld metals [57-59, 84]. Most often, the dendrite tip temperature solutions for austenite and ferrite are solved as a function of solidification velocity for a given alloy chemistry and temperature gradient. The dendrite tip temperatures are then plotted for both phases as a function of solidification velocity to identify at which range of velocities each

phase should predominate during the solidification sequence. It has been shown that metastable austenite growth can occur when growth kinetics preferentially suppress ferrite growth. The inverse case of metastable ferrite growth is generally not reported for austenitic stainless steel weld metals. As presented by Fukumoto, undercooling due to solute segregation is primarily responsible for metastable austenite growth, where austenite stabilizing elements preferentially suppress ferrite growth more than ferrite stabilizing elements suppress austenite growth [59].

For a given alloy, the critical transition between stable ferrite and metastable austenite formation occurs when the dendrite tip temperature solutions are equal. This condition can be presented as:

$$T_d^\gamma = T_d^\delta$$

By substituting the liquidus temperature and undercooling terms for austenite and ferrite, the same expression can be written as:

$$T_L^\gamma + \Delta T^\gamma = T_L^\delta + \Delta T^\delta$$

Rearranging this equation to separate the thermodynamic and kinetic terms gives the expression:

$$T_L^\gamma - T_L^\delta = \Delta T^\delta - \Delta T^\gamma = K$$

where a constant, K , is included to represent the temperature range where the difference in liquidus temperatures is equal to the difference in undercooling at the dendrite tip. The condition of $K = 0$ represents global equilibrium where there is no undercooling at the solid-liquid interface and the liquidus temperatures are equal. When $K \neq 0$, the difference

in liquidus temperatures is equal to the difference in undercooling between austenite and ferrite. When this condition is satisfied, the dendrite tip temperatures for austenite and ferrite are equal and both phases have the same likelihood to grow into the weld pool for a given solidification velocity and temperature gradient.

Conveniently, the left-hand side of the rearranged dendrite tip temperature equality condition is in the same form as the ΔT_L solidification parameter that was introduced in the last chapter. This provides an opportunity to directly relate dendrite growth theory to the ΔT_L equivalencies that were presented previously to create a predictive primary solidification mode diagram for austenitic stainless steel weld metals.

Development of a Primary Solidification Mode Diagram

As an initial step to develop a predictive primary solidification mode diagram, the Theoretical WRC database was mapped onto a Cr_{eq} - Ni_{eq} composition space using both the ΔT_L and $\Delta T_{L,2}$ equivalencies. The plotted compositions are presented in Figure 28 for both sets of equivalencies. In Figure 28, the color of each data point represents the solidification mode that was predicted via computational thermodynamics, that is, the thermodynamically stable solid phase at the nominal liquidus temperature for each alloy. As seen, a sharp transition between the predicted primary austenite and primary ferrite regions was achieved with both equivalencies compared to the original WRC equivalencies presented in Figure 13. The boundary that separates the primary austenite and primary ferrite compositions represents the condition where $K = 0$. Comparing the ΔT_L and $\Delta T_{L,2}$ equivalencies, the $\Delta T_{L,2}$ equivalencies provide a better delineation between primary

austenite and primary ferrite equilibrium calculations. Therefore, the $\Delta T_{L,2}$ equivalencies which include curvature terms for Cr and Ni will be considered moving forward.

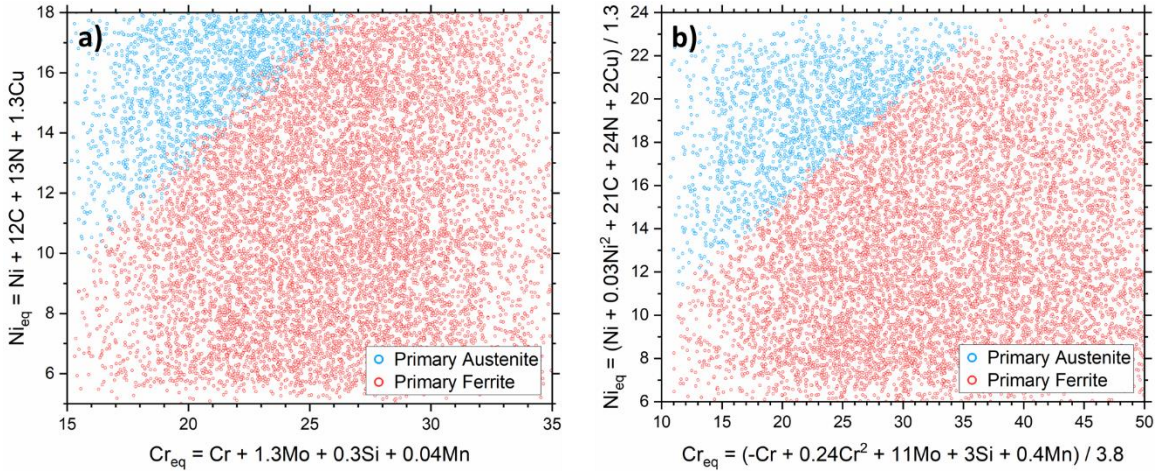


Figure 28: Calculated stable solid phase at the nominal liquidus temperature for each alloy in the Theoretical WRC database; a) plotted with the ΔT_L equivalency expressions; b) plotted with the $\Delta T_{L,2}$ equivalency expressions

Although the equivalency maps presented in Figure 28 nicely separate the equilibrium predictions for primary austenite and primary ferrite solidification, the fact remains that thermodynamic calculations do not match experimental evidence near the primary austenite / primary ferrite transition for austenitic stainless steel weld metals. Therefore, a correction must be applied to the diagram to account for growth kinetics. There are three possible avenues to apply such a correction:

- Plot experimental data onto the solidification mode map and manually draw a solidification mode boundary

- Use multicomponent dendrite growth theory to estimate the undercooling associated with austenite and ferrite growth for a range of compositions near the equilibrium primary austenite / primary ferrite transition to calculate $\Delta T^\delta - \Delta T^\gamma = K$; for this approach, a representative temperature gradient in the liquid and solidification velocity need to be defined to assess a range of undercooling conditions where metastable austenite growth is predicted
- Calculate the equilibrium liquidus temperatures for austenite (T_L^γ) and ferrite (T_L^δ) for a range of compositions that display metastable austenite growth to calculate $T_L^\gamma - T_L^\delta = K$

The first approach is straightforward and will therefore not be discussed here. It can easily be implemented with a suitable dataset of austenitic stainless steel weld metals where the solidification modes and chemical compositions have been characterized for a given set of solidification conditions. This is similar to how the original solidification mode boundaries were constructed for the WRC diagrams [4, 5].

The second two correction methods rely on calibrating the solidification mode diagram by determining the dendrite tip temperature equality constant, K . If K can be determined, it can be used to project a primary austenite / primary ferrite transition line onto the predictive solidification mode diagram. This can be achieved by performing multicomponent dendrite growth simulations or by calculating the stable and metastable liquidus temperatures for a set of known compositions. The former is much more computationally expensive and requires several parameters to be defined that are often assumed to be constant and/or need to be calculated using the CALPHAD approach.

Further, a suitable solidification velocity and temperature gradient would need to be directly measured, inferred through characterization or modeling techniques, or assumed based on data from the literature. The last correction technique is much simpler to implement as stable and metastable liquidus temperatures can readily be calculated using just alloy chemistry data.

It is important to note that the equality constant, K , is a dynamic parameter that depends on both alloy chemistry and solidification conditions. For example, consider a hypothetical stainless steel composition that satisfies the condition where austenite and ferrite have the same dendrite tip temperature for a given solidification velocity. If the solidification velocity is increased or decreased, the amount of undercooling at the solidification front will change for each phase and the equality condition will no longer hold true, i.e. one phase should predominate. Similarly, not all stainless steel chemistries will satisfy the condition where austenite and ferrite have the same dendrite tip temperature for a constant solidification velocity. Therefore, for a predictive solidification mode diagram that covers a wide composition space, limiting K values should be defined that bound chemical compositions between primary austenite solidification and primary ferrite solidification for nominally similar solidification conditions. These bounding K values for austenitic stainless steels should contain all cases of metastable primary austenite growth.

To determine suitable K limits for the predictive solidification mode diagram, ΔT_L was calculated for all chemical compositions within the WRC Appendix II solidification mode database with Mn concentrations less than 3 wt.%. The calculated ΔT_L values were then compared with the experimentally determined solidification mode for each sample.

Figure 29 presents the calculated stable solid phase for each alloy plotted on the WRC-1988 equivalency space and histograms of ΔT_L for various subsets of the data. The histograms in Figure 29 represent the ΔT_L distributions for the full data set, samples where thermodynamic calculations correctly predicted the experimentally determined solidification mode, and samples where thermodynamic calculations and experimental solidification mode data were not in agreement. As seen, the discrepancy between thermodynamic calculations and experimental data was restricted to negative values. Negative ΔT_L values in this case correspond to metastable primary austenite growth.

From this analysis, limits for K can be defined. An upper limit for K can simply be defined by the global equilibrium case where $K = 0^\circ\text{C}$. The lower limit for K is defined by the lowest ΔT_L value where thermodynamic calculations and experimental observations were not in agreement. In this case, the lower limit is approximately equal to $K = -13^\circ\text{C}$. The ΔT_L ranges where thermodynamic calculations and experimental data agree and disagree are not mutually exclusive. Therefore, the ΔT_L range bounded by $-13^\circ\text{C} \leq K \leq 0^\circ\text{C}$ is conservative with respect to the evaluated experimental data. Compositions that fall above $K = 0^\circ\text{C}$ exhibit primary austenite solidification, and compositions that fall below $K = -13^\circ\text{C}$ exhibit primary ferrite solidification. Between those boundaries, primary austenite, primary ferrite, and mixed mode solidification may occur.

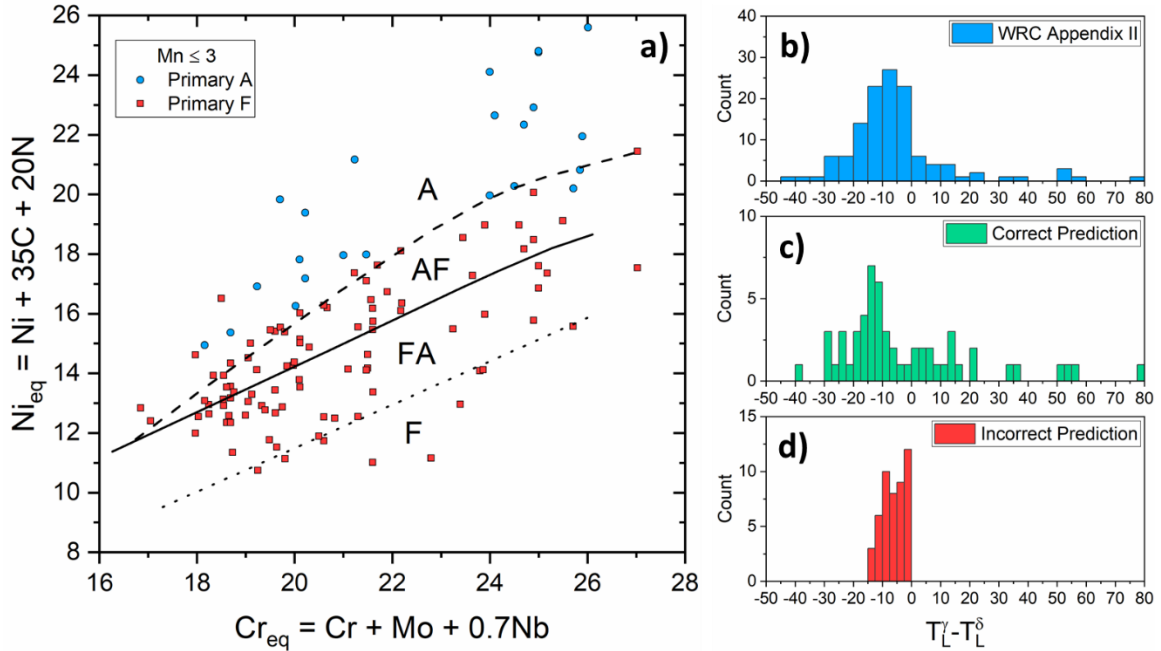


Figure 29: a) Equilibrium phase diagram predictions for the primary solidification mode of each sample in the WRC Appendix II database plotted on the WRC-1988 diagram; b) corresponding ΔT_L histogram for the full data set; c) ΔT_L histogram for samples where the equilibrium phase diagram predictions matched the experimentally observed solidification mode; d) ΔT_L histogram for samples where the equilibrium phase diagram predictions did not match the experimentally observed solidification mode

To construct the boundaries on the new primary solidification mode diagram the Theoretical WRC data was plotted on the $\Delta T_{L,2}$ equivalency space and best-fit linear models were found for subsets of the ΔT_L data. The linear models were constructed using $1^\circ C > \Delta T_L > -1^\circ C$ for $K = 0^\circ C$ and $-12^\circ C > \Delta T_L > -14^\circ C$ for $K = -13^\circ C$. Figure 30 presents the primary solidification mode diagram with the Theoretical WRC database

plotted and colorized by ΔT_L for the region of interest between the bounding K values. The newly defined boundaries are also shown. Two key features are apparent in Figure 30. First, the newly defined boundaries contain the ΔT_L values of interest quite well. Secondly, the boundary lines are nearly parallel and the gradient between the boundary lines is consistent. Therefore, the equivalencies effectively linearized the ΔT_L data in this range. A version of the solidification mode diagram without the datapoints is presented in Figure 31.

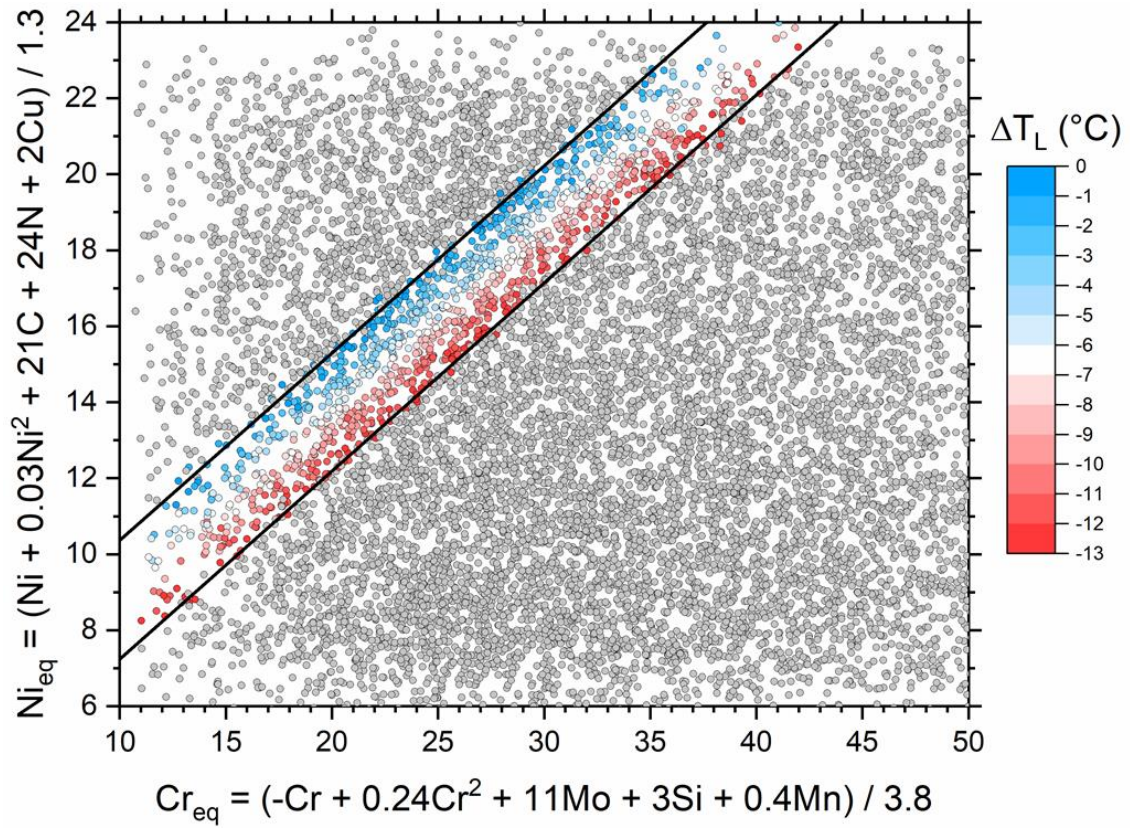


Figure 30: Theoretical WRC database plotted onto the $\Delta T_{L,2}$ equivalency space with data points colorized between $-13^\circ\text{C} \leq \Delta T_L \leq 0^\circ\text{C}$; the upper boundary represents $K = 0^\circ\text{C}$ and the lower boundary represents $K = -13^\circ\text{C}$

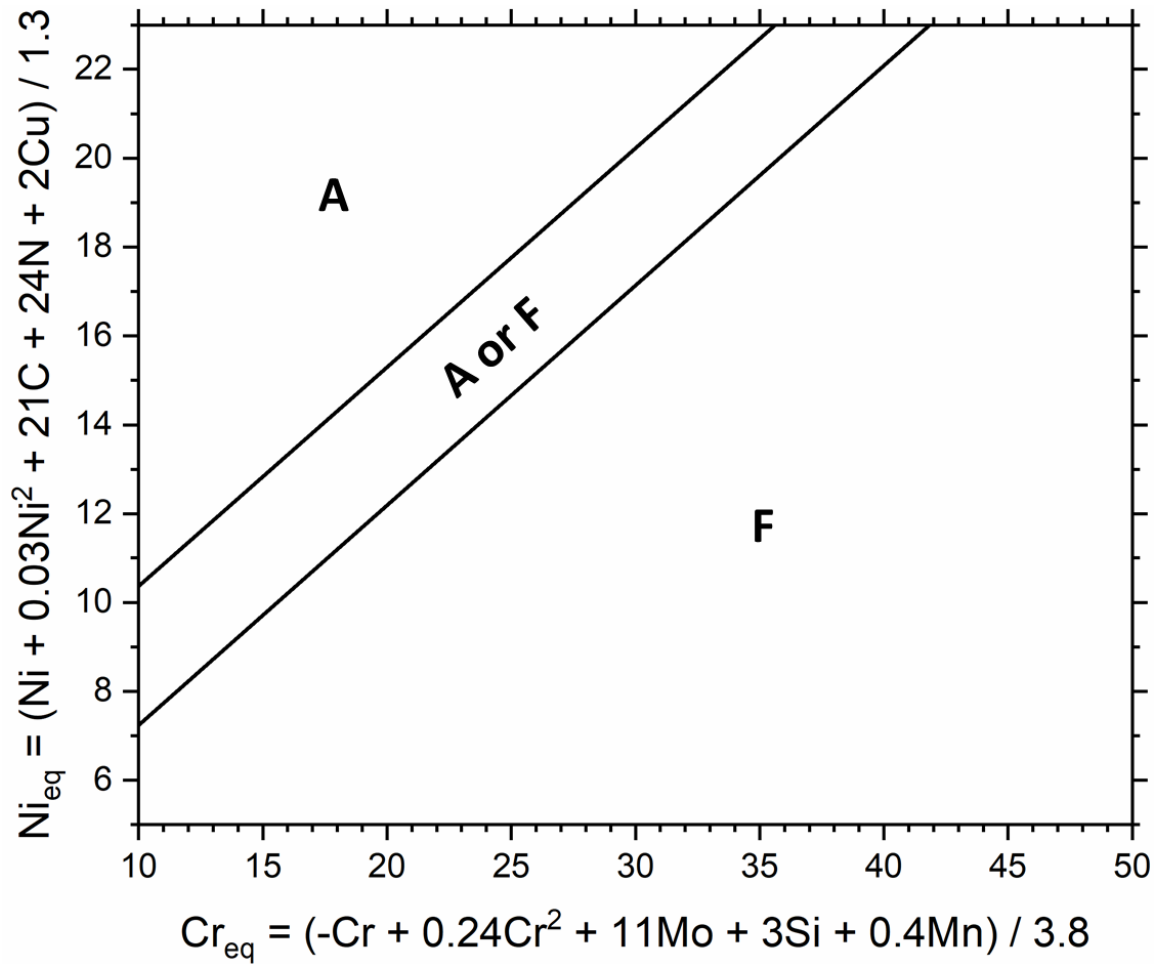


Figure 31: Final primary solidification mode diagram using the $\Delta T_{L,2}$ equivalency expressions

Classification of Alloy Types

Analysis of the ΔT_L data presented in Figure 29 and solidification mode diagram presented in Figures Figure 30 and Figure 31 reveals that austenitic stainless steel weld metal compositions can be classified into four types based on their stable/metastable liquidus temperatures and kinetic response. Schematic representations of each alloy type

are presented in Figure 32 where liquidus temperatures and dendrite tip temperatures are presented for both austenite and ferrite as a function of solidification velocity. Note that the discussion of these alloys types is restricted to steady-state dendritic growth where local equilibrium is maintained at the solid-liquid interface. The alloy types can be classified as follows:

- Type 1: Austenite liquidus temperature is higher than ferrite liquidus temperature; these alloys fall within the A region of Figure 31 where both the thermodynamic response and kinetic response of the alloys promote primary austenite growth
- Type 2: Austenite and ferrite liquidus temperatures are equal; dendrite growth kinetics favor primary austenite growth across all solidification velocities; these alloys are represented by the boundary between the A and (A or F) regions of Figure 31
- Type 3: Austenite liquidus temperature is lower than ferrite liquidus temperature; dendrite growth kinetics support ferrite growth at low solidification velocities and austenite growth above a critical solidification velocity; these alloys fall within the (A or F) region of Figure 31
- Type 4: Austenite liquidus temperature is lower than ferrite liquidus temperature; the difference in liquidus temperatures is sufficiently large enough to prevent austenite growth at all solidification velocities; these alloys fall within the F region of Figure 31

Notice that the boundary between (A or F) and F was not classified. This condition represents a special case of Type 3 alloys where the solidification velocity of the solid-

liquid interface is equal to the critical solidification velocity that separates primary austenite and primary ferrite solidification.

It is also noteworthy that growth-controlled mixed mode solidification can be classified by Type 3 when the welding travel speed is greater than the critical solidification velocity. This can be understood by considering a geometric representation of a steady-state weld pool, where the local solidification velocity of the solid-liquid interface is dependent on its orientation relative to the traveling heat source [65, 85]. The maximum solidification velocity of a steady-state weld pool is limited by the welding travel speed. The local solidification velocity will be reduced if the solidification front normal is not parallel to the travel direction of the heat source. As a result, mixed mode solidification can occur if the welding travel speed exceeds the critical solidification velocity for an austenitic stainless steel chemistry. This velocity-dependent mixed mode solidification behavior has been observed previously [86, 87]. Kou identified mixed mode primary solidification behavior in Type 309L gas tungsten arc weld deposits [86]. Similarly, Lippold found mixed mode primary solidification in Type 304L electron beam welds [87]. In both studies, primary austenite solidification was found along the weld centerline where the solidification velocity was highest, while the bulk of the fusion zone solidified as primary ferrite.

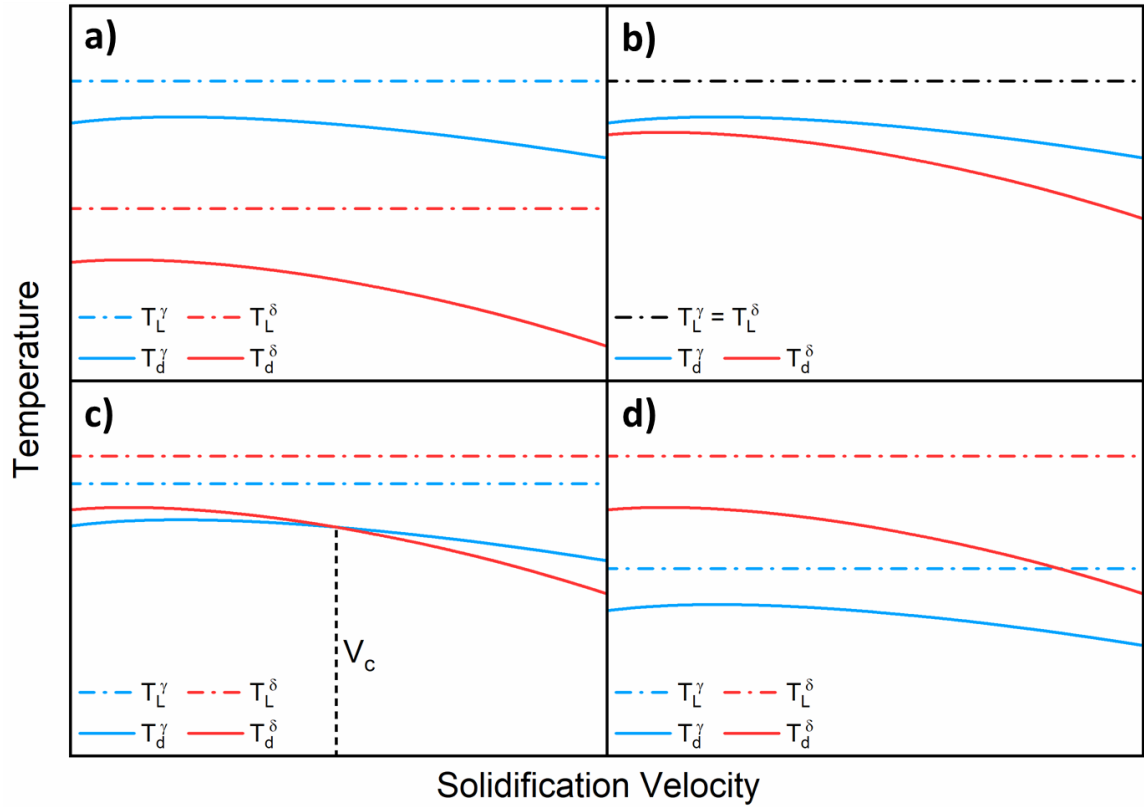


Figure 32: Schematic representation of austenitic stainless steel alloy classifications based on the liquidus temperatures (T_L) and dendrite tip temperatures (T_d) of austenite (γ) and ferrite (δ) as a function of solidification velocity; a) Type 1 alloys showing stable austenite growth; b) Type 2 alloy showing stable austenite growth; c) Type 3 alloy showing stable ferrite growth below a critical solidification velocity (V_c) and metastable austenite growth above V_c ; d) Type 4 alloy showing stable ferrite growth

Use of the Solidification Mode Diagram

The newly developed primary solidification mode diagram presented in Figure 31 has two key characteristics that should be discussed. First, the inclusion of squared terms

for Cr and Ni in the equivalency expressions results in a non-linear mapping of compositions when dilution calculations are performed. On similar predictive diagrams that do not include squared terms for any of the elements (such as the WRC-1998 and WRC-1992 diagrams), dilution calculations between two bounding chemical compositions can be performed by simply plotting the respective Cr_{eq} and Ni_{eq} values on the diagram and drawing a linear relationship between each composition [6]. In the case of the new diagram, the line that connects the endpoints of a dilution calculation will not be linear. Therefore, the dilution estimates along that path need to be calculated and plotted individually. Secondly, the boundaries on the diagram were determined using the WRC Appendix II database. This assumes that the chemical compositions contained within the WRC Appendix II database were accurately measured, solidification modes of the weld deposits were properly characterized, welds were free of any substrate nucleation effects, and the welding conditions for all of the data points were nominally similar. It is entirely possible that the lower boundary that separates the (A or F) and F regions will shift based on the chemical compositions and welding conditions that are being evaluated. For example, increasing the solidification front velocity (i.e. increasing travel speed) should shift the boundary lower on the diagram, or reducing the solute content should shift the boundary to higher values. Therefore, it may be necessary for a given application to tailor the position of the lower boundary on the diagram to account for the alloys and welding processes of interest. The upper boundary that separates the A and (A or F) regions of the diagram should remain constant as it represents the global equilibrium separation between austenite and ferrite. To support future tailoring of the diagram for specific applications,

the parameters presented in Table 2 can be used to draw new boundaries. The boundary equations for the ΔT_L equivalencies that do not include curvature terms (corresponding to Figure 28a) are also included if constructing such a diagram is of interest.

Table 2: Parameters to construct linear boundaries for various K values for the $\Delta T_{L,2}$ and ΔT_L equivalencies

K (°C)	$\Delta T_{L,2}$ Equivalencies			ΔT_L Equivalencies		
	Ni_{eq}/Cr_{eq}	Ni_{eq} Intercept	R^2	Ni_{eq}/Cr_{eq}	Ni_{eq} Intercept	R^2
0	0.493	5.439	0.99	0.747	-1.646	0.95
-1	0.481	5.490	0.99	0.749	-1.907	0.96
-2	0.485	5.150	0.99	0.768	-2.499	0.96
-3	0.481	4.965	0.99	0.759	-2.444	0.96
-4	0.488	4.600	0.99	0.768	-2.789	0.95
-5	0.492	4.301	0.99	0.791	-3.508	0.96
-6	0.482	4.257	0.99	0.788	-3.713	0.98
-7	0.485	3.993	0.99	0.772	-3.477	0.97
-8	0.492	3.561	0.99	0.775	-3.662	0.97
-9	0.491	3.343	0.99	0.792	-4.221	0.97
-10	0.487	3.244	0.99	0.809	-4.780	0.97
-11	0.491	2.876	0.99	0.828	-5.403	0.97
-12	0.493	2.602	0.99	0.826	-5.511	0.98
-13	0.495	2.288	0.99	0.824	-5.635	0.97
-14	0.494	2.066	0.99	0.827	-5.870	0.97
-15	0.497	1.781	0.99	0.839	-6.309	0.97
-16	0.504	1.339	0.99	0.845	-6.621	0.98
-17	0.507	0.995	0.99	0.852	-7.001	0.98
-18	0.502	0.936	0.99	0.866	-7.490	0.98
-19	0.497	0.844	0.99	0.886	-8.165	0.98
-20	0.501	0.496	0.99	0.889	-8.423	0.98

Caution should be exercised when the primary solidification mode diagram is applied to scenarios where base and filler metal compositions, or base metal compositions of dissimilar autogenous welds, fall on opposite sides of the solidification mode boundaries on the diagram. Experimental evidence has shown that there is a path dependence related to the transition point between primary austenite and primary ferrite solidification modes for dissimilar metal stainless steel welds [62, 88, 89]. Specifically, the transition from primary austenite to primary ferrite solidification does not occur at the same chemical composition as the transition from primary ferrite to primary austenite when welding conditions are held constant. Bhadeshia, Tsukamoto, and Fukumoto all demonstrated this effect by performing autogenous dissimilar stainless steel welding experiments where the travel direction of the heat source was perpendicular to a butt weld seam. It was found that primary austenite dendrites could grow across the dissimilar stainless steel junction, whereas primary ferrite could not grow across the junction when the welding direction was reversed. Fukumoto found that the primary ferrite to primary austenite transition agreed with dendrite growth model calculations for ternary Fe-Ni-Cr laser welds across a wide range of solidification velocities, whereas the primary austenite to primary ferrite transition was consistently shifted to higher Cr/Ni ratios [62]. This suggests that a nucleation barrier exists for the transition from metastable primary austenite growth to stable primary ferrite growth. As a result, the growth mode boundary may shift to lower K values on the primary solidification mode diagram when welding from primary austenite compositions to primary ferrite compositions. Similarly, mixed mode solidification may be observed in dissimilar stainless steel welds where the weld metal chemistry would normally solidify as primary

ferrite but a portion of the partially melted zone is fully austenitic. This same effect could also originate from residual macrosegregation in the substrate materials for similar stainless steel welds near the transition boundaries. Note that this behavior is not unique to the new primary solidification mode diagram and should be considered when similar legacy tools are used, i.e., the WRC-1988, WRC-1992, and Suutala diagrams.

An often-overlooked aspect of predicting stainless steel solidification behavior is the uncertainty of weld metal chemical compositions. Provided that knowing the chemical composition of a given stainless steel weld metal is critically important to effectively apply such tools, it seems appropriate to discuss chemical composition uncertainty and how it might influence the use of such a diagram. Certified material test reports for welding consumables and/or base materials are most often used in practice, however, the uncertainty associated with those chemistry measurements is seldomly known and they generally represent the analysis of a large heat of material, not the specific filler or base materials that are being used.

Monte Carlo sampling was performed for a hypothetical stainless steel chemistry to demonstrate how measurement precision can influence the likely position of a data point on the new solidification mode diagram. To do this, a stainless steel chemistry was defined that sits along the boundary between the (A or F) and F regions of the new solidification mode diagram. Typical chemical concentration standard deviation values for each element were then defined based on published product literature for a commercially available arc/spark optical emission spectrometry (OES) system and the concentration ranges of interest [90]. The hypothetical chemical composition and standard deviation values for

each element for three test cases are presented in Table 3. Monte Carlo sampling was then used to randomly generate chemistry data for the hypothetical sample by assuming that the concentration distribution for each element was normally distributed, and that those normal distributions were defined by the values presented in Table 3. A total of 10,000 chemistries were created for each test case. The first test case considered the distributions using the standard deviation values that were defined from the OES product literature [90]. The second and third test cases assumed that the measurement variance for each element in the first test case was doubled and tripled, respectively.

Table 3: Hypothetical stainless steel chemistry and standard deviation values used to perform Monte Carlo sampling for various chemical analysis test cases

	Cr	Ni	C	Mn	Si	Mo	N	Cu
Concentration (wt.%)	20.05	12.17	0.05	1.50	0.50	1.50	0.05	0.10
Case 1 Std. Dev. (wt.%)	0.050	0.037	0.001	0.008	0.003	0.008	0.001	0.001
Case 2 Std. Dev. (wt.%)	0.071	0.052	0.001	0.011	0.004	0.011	0.001	0.001
Case 3 Std. Dev. (wt.%)	0.087	0.063	0.001	0.013	0.004	0.013	0.001	0.001

The data from each Monte Carlo test case are presented in Figure 33. Each iteration from each Monte Carlo test case is represented by a data point on the equivalency space of the new solidification mode diagram. Each data point represents a possible chemistry measurement for the hypothetical stainless steel sample assuming that the imaginary measurement system is performing within the specified levels of precision for each

element. Cr_{eq} and Ni_{eq} distributions are also presented for each test case. As expected, the data for each test case are split 50/50 between the (A or F) and F regions of the diagram since the hypothetical stainless steel composition was defined along the boundary that separates them. As the measurement variance increased, the range of possible Cr_{eq} and Ni_{eq} combinations also increased. Each test case displayed the following approximate equivalency ranges (Cr_{eq} , Ni_{eq}): case 1 (0.9, 0.4); case 2 (1.3, 0.5); case 3 (1.6, 0.7). This data demonstrates that even for a well calibrated instrument that lacks bias, random measurement error can cause individual measurements to deviate from the true value of the sample chemistry, which in turn changes the position of data points on a composition equivalency space. This presents a challenge if resolution is needed near a specific boundary on the diagram. Further, the precision limits set for each test case are likely idealized since the values were produced by an OES instrument manufacturer using homogenous samples with ten successive measurements to produce the reported standard deviation values. Regardless, applying a technique such as the Monte Carlo sampling used here or by simply assessing a suitable confidence interval (e.g., +/- 2 standard deviations) in the Cr_{eq} and Ni_{eq} directions using measured data for a given sample can provide an indication of uncertainty if a composition sits near a transition boundary.

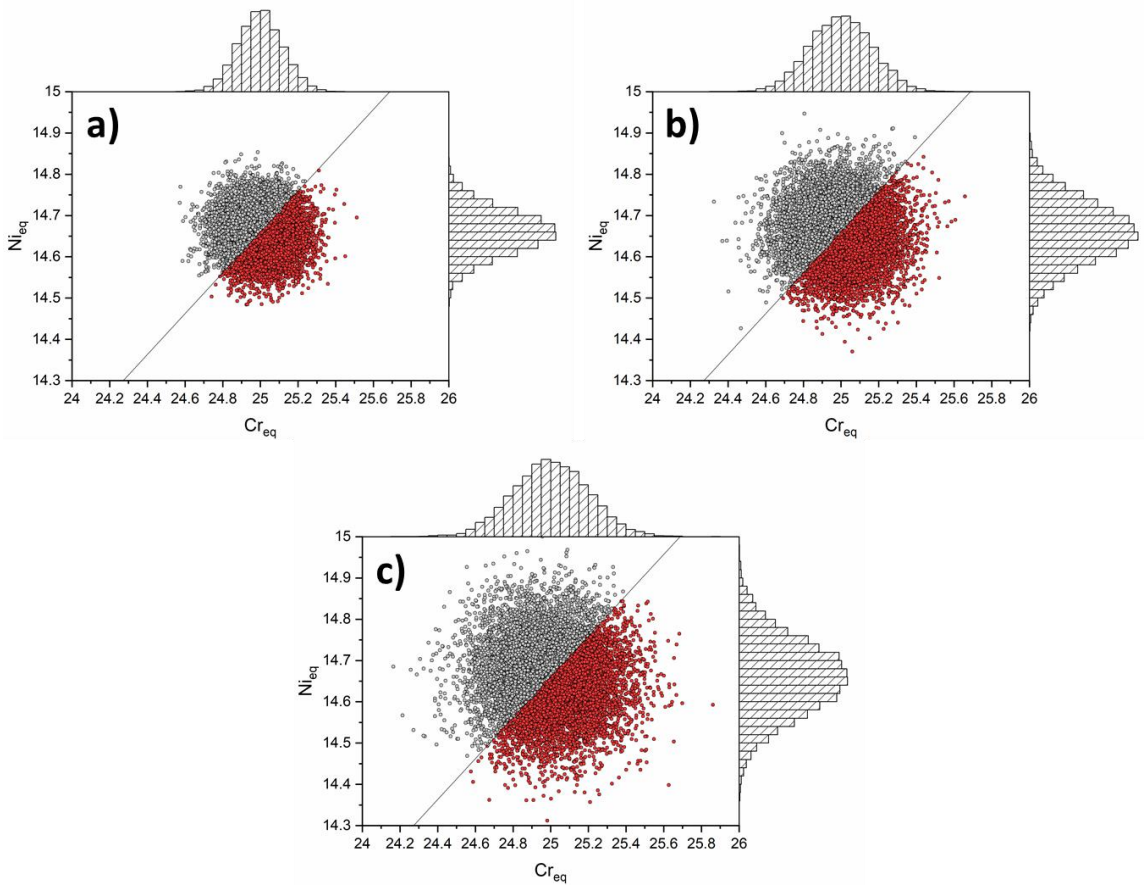


Figure 33: Monte Carlo sampling results showing the effect of random measurement error on the position of chemical compositions projected onto the $\Delta T_{L,2}$ equivalency space; the average chemical composition sits along the boundary between (A or F) and F solidification; a) Case 1 (1x variance); b) Case 2 (2x variance); c) Case 3 (3x variance)

In addition to precision considerations for a given analytical technique at a given laboratory, considerable variability has been reported during interlaboratory testing of stainless steel weldments during a round robin study conducted by the International Institute of Welding (IIW) [91]. Within the IIW study, five weldments were created with

different stainless steel weld metals. Participating laboratories were then asked to measure the FN of each weldment at various locations, perform chemical analysis on slices of each weldment using OES and combustion methods, and predict the FN of each weldment using their preferred technique (such as the WRC-1992 diagram). The chemical analysis results for each weldment from each participating laboratory are plotted on the new primary solidification mode diagram in Figure 34. The effects of interlaboratory variability are readily apparent in Figure 34, where a fairly large range of Cr_{eq} and Ni_{eq} values are calculated for each sample. Farrar discussed that the variability amongst the laboratories in the IIW round robin study was most likely due to chemical inhomogeneity in the weld deposits rather than a fundamental difference in the chemical analysis techniques that were used [91]. While this may be true, even controlled interlaboratory studies using homogenous samples exhibit considerable variability. For example, the reproducibility limits listed in ASTM E1086 (OES) and E1019 (Combustion methods) were used to assess the chemical analysis variability associated with interlaboratory testing of 304 and 316 stainless steels [92, 93]. The reproducibility limits can be used to describe 95% confidence intervals for the 304 and 316 samples which were analyzed by multiple laboratories to develop the standards. If another laboratory were to analyze the same samples using the same methods described in ASTM E1086 and E1019, there would be a 95% probability that the new laboratory's results would fall within the 95% confidence interval for each element. The presented chemical compositions and the upper and lower limits for the 95% confidence intervals for each element were used to calculate bounding equivalency ranges on the new equivalency diagram for the 304 and 316 samples. Figure 35 presents the

position of each alloy on the new diagram as well as error bars in the Cr_{eq} and Ni_{eq} directions that reflect the 95% confidence intervals for the interlaboratory reproducibility data. This analysis was also performed for the same alloys using repeatability limits from E1086 and E1019 for comparison. The repeatability limits represent variability within a single laboratory and are also presented in Figure 35. As seen, the expected variability from the E1086 and E1019 reproducibility limits is qualitatively in alignment with the data presented in Figure 34 from the IIW round robin study. The results are qualitatively comparable in this case because each of the alloys presented in Figures Figure 34 and Figure 35 have differing nominal chemical compositions that would intrinsically result in changes in the expected variability. Furthermore, the chemical analysis presented from the IIW study was taken from weldments, while the E1086 and E1019 analysis was conducted on base materials. The reproducibility 95% confidence intervals presented in Figure 35 correspond to K ranges of approximately 5°C and 10°C in the Cr_{eq} and Ni_{eq} directions, respectively. Clearly, this data shows that if a particular stainless steel chemistry sits near a transition boundary on a predictive diagram, chemical analysis variability can drastically influence the prediction results. A similar assessment was discussed by Kotecki on the use of chemical analysis to predict FN in austenitic stainless steel weld metals [94].

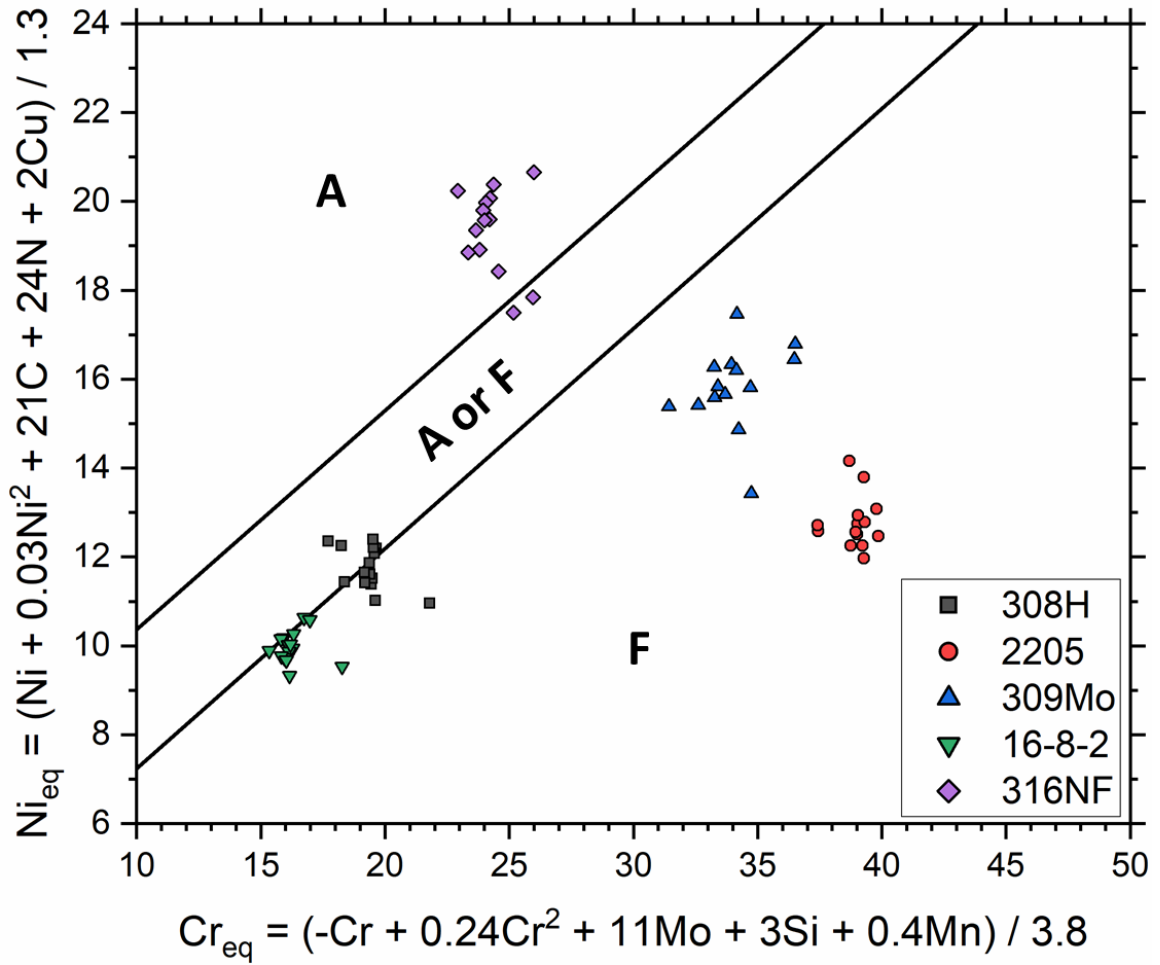


Figure 34: Chemical analysis data from laboratories that participated in an IIW round robin study to measure the chemical composition of five different stainless steel weldments plotted on the $\Delta T_{L,2}$ equivalency space; symbol shapes/colors identify each weldment; matching symbols indicate the reported chemistry values from different laboratories [91]

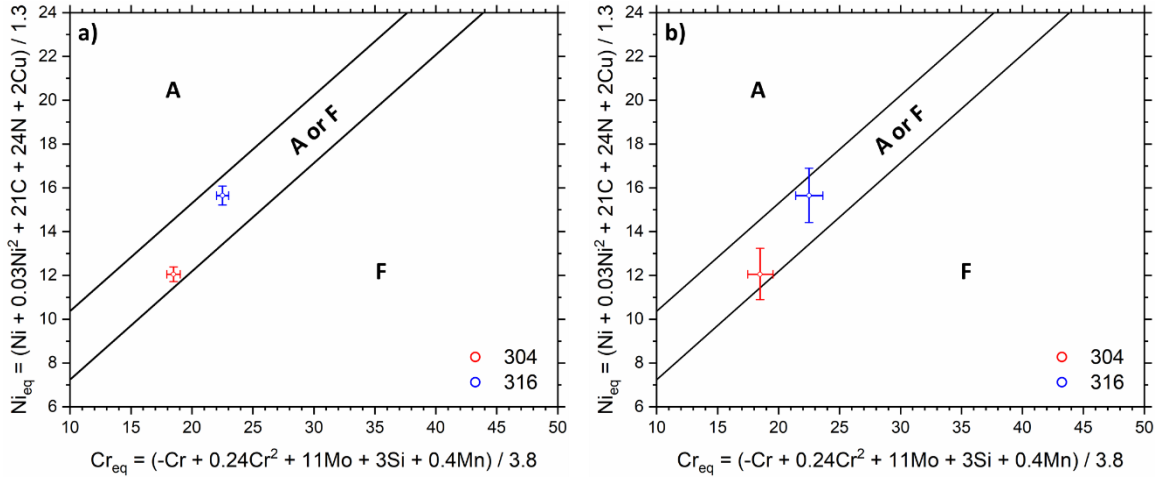


Figure 35: The effect of chemical analysis variability on Cr_{eq} and Ni_{eq} for 304 and 316 stainless steel samples ($\Delta T_{L,2}$ equivalencies); a) single laboratory testing; b) interlaboratory testing; error bars represent the 95% confidence intervals for each sample; 304 chemistry: Fe-18.65Cr-9.63Ni-0.765Mn-0.55Si-0.316Mo-0.33Cu-0.014C-0.096N (wt.%); 316 chemistry: Fe-17.48Cr-12.54Ni-1.66Mn-0.72Si-2.44Mo-0.24Cu-0.014C-0.096N (wt.%)

The data presented in Figures Figure 33, Figure 34, and Figure 35 demonstrate how chemical analysis measurement uncertainty can influence the position of individual weld metal chemistries on the new primary solidification mode diagram. Ideally, the chemical composition of a representative weldment can be accurately determined for a given application. Even when the chemical composition of a representative weldment can be measured, uncertainty still exists due to the precision of the analytical technique, measurement bias that may be associated with a given laboratory, and variability associated with chemical inhomogeneity. Therefore, the predictive ability of such a diagram is

dependent on the user adequately accounting for chemical analysis variability. An obvious best practice would be to take many individual chemistry measurements on a calibrated instrument that has been tested against a reference standard before and/or after the analysis. This applies to any predictive technique where chemical composition is a necessary input parameter. In the event that constraints are placed on both the chemical composition space of interest and the measurement techniques that are used (such as defining acceptable precision limits for a given instrument and requiring that reference standards be used), uncertainty bands could be applied to the transition boundaries directly rather than accounting for the error of single data points.

Conclusions

The CALPHAD-based equivalency expressions derived in Chapter 3 from the ΔT_L parameter have been used to construct a new primary solidification mode diagram for austenitic stainless steel weld metals. The conclusions from this effort can be summarized as follows:

- Through the consideration of dendrite growth theory, a method has been established to directly relate the ΔT_L and $\Delta T_{L,2}$ equivalency relationships to primary solidification mode for austenitic stainless steel weld metals.
- A new diagram, based on the $\Delta T_{L,2}$ equivalencies, was constructed and calibrated using experimental data from the literature. A set of equations were also presented to allow users to tailor boundary positions on the diagram for situations where dendrite growth kinetics differ from those explored here.

- By assessing legacy experimental data and the newly constructed primary solidification mode diagram, a new classification scheme based on the thermodynamic response and kinetic response of austenitic stainless steel weld metals has been proposed. The classifications can be used to understand the occurrence of metastable primary austenite solidification as well as growth-controlled mixed mode solidification.
- The effect of chemical analysis uncertainty on the newly constructed primary solidification mode diagram was also explored through Monte Carlo sampling, experimental interlaboratory test data, and applicable chemical analysis test standards. It has been demonstrated that measurement uncertainty can have a profound effect on the predictive ability of such a diagram. Unfortunately, this is often ignored in the literature. As such, users of the new primary solidification mode diagram, or any other predictive tool that relies on an accurate description of weld metal chemistry for that matter, should exercise caution when compositions fall near boundaries that delineate solidification behavior predictions.

Chapter 5. Experimental Investigation of Newly Developed Primary Solidification Mode Diagram

Introduction

Chapters 3 and 4 explored the use of CALPHAD-based methodologies to develop a new predictive diagram for the primary solidification mode of austenitic stainless steel weld metals. The fundamental basis for the diagram was rooted in equilibrium thermodynamics, which was then correlated with dendrite growth theory to establish a process to calibrate the diagram using experimental data.

To assess the effectiveness and utility of the newly developed diagram, an independent set of welding experiments were carried out on samples with controlled chemical compositions. A gas tungsten arc spot welding procedure was developed to provide a consistent melting and solidification cycle for each sample. The solidification mode of each sample was then characterized to compare back to the solidification mode predictions of the WRC-1992 diagram, primary solidification mode diagram presented in the previous chapter, and multicomponent dendrite growth model predictions. A flow chart depicting the approach can be found in Figure 36.

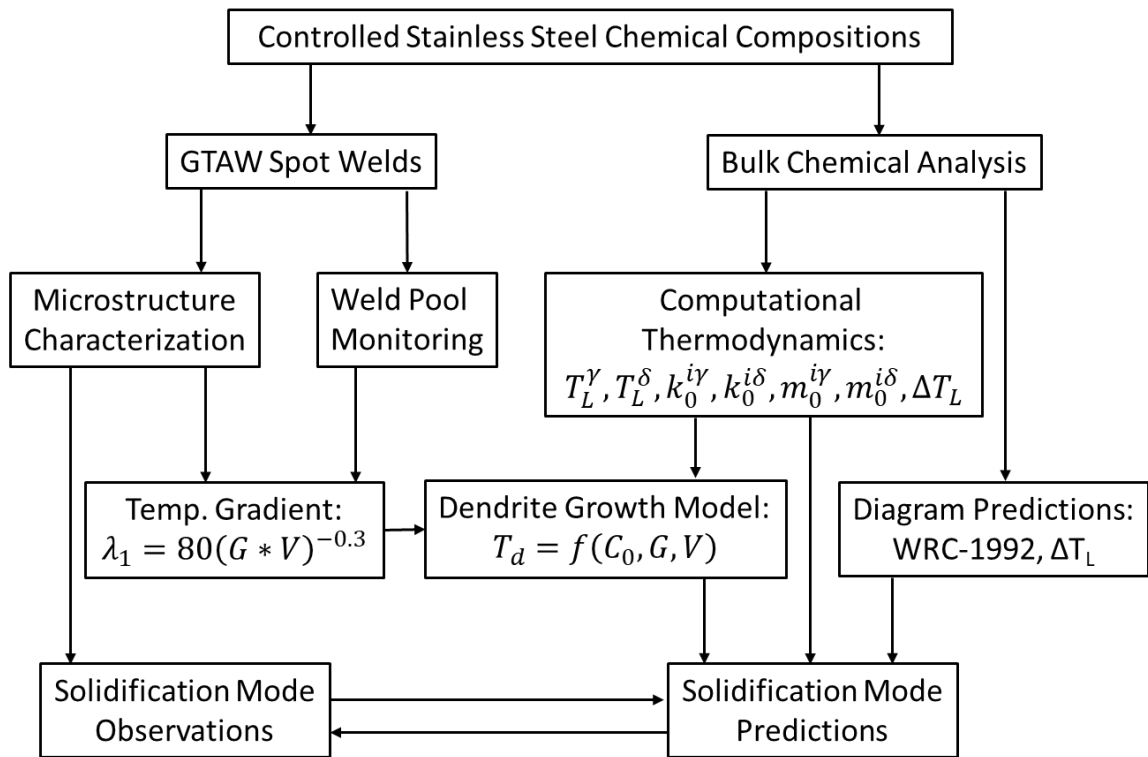


Figure 36: Flowchart for comparing experimental and predicted solidification mode behavior

Experimental Procedures

Materials

In order to investigate the effectiveness of the new primary solidification mode diagram, stainless steel weld metal compositions that span between the A and F boundaries were targeted by creating mixtures of commercially available austenitic stainless steel filler materials. Seven filler materials were selected to create a range of mixtures. Specifically, the following austenitic stainless steel filler wire types were selected: ER308L, ER308LSi,

ER309L, ER309LSi, ER316L, ER316LSi, and ER330. The certified material test reports for each filler wire can be found in Appendix A. The first six filler materials all fall below the (A or F) and F boundary on the new diagram, while 330 stainless steel falls well above the (A or F) and A boundary. By creating mixtures with each of the first six alloys and 330 stainless steel, the chemistry space where the primary austenite and primary ferrite transition occurs was interrogated. Dilution calculations were performed to identify the relative weights of each wire to reach the target compositions using the certified material test reports for each material.

The locations of the targeted compositions on the WRC-1992 and new primary solidification mode diagrams are presented in Figure 37, where distinct vertically oriented clusters of sample chemistries are apparent. Each cluster represents the target dilution levels between 330 stainless steel and one of the other six alloys. Note that the alloys were created and analyzed in an iterative fashion by starting at the upper most mixture for each alloy diluted with 330 stainless steel and working towards the lower ferrite region. Once primary ferrite solidification was identified during the welding experiments, no more samples were created for that given material combination.

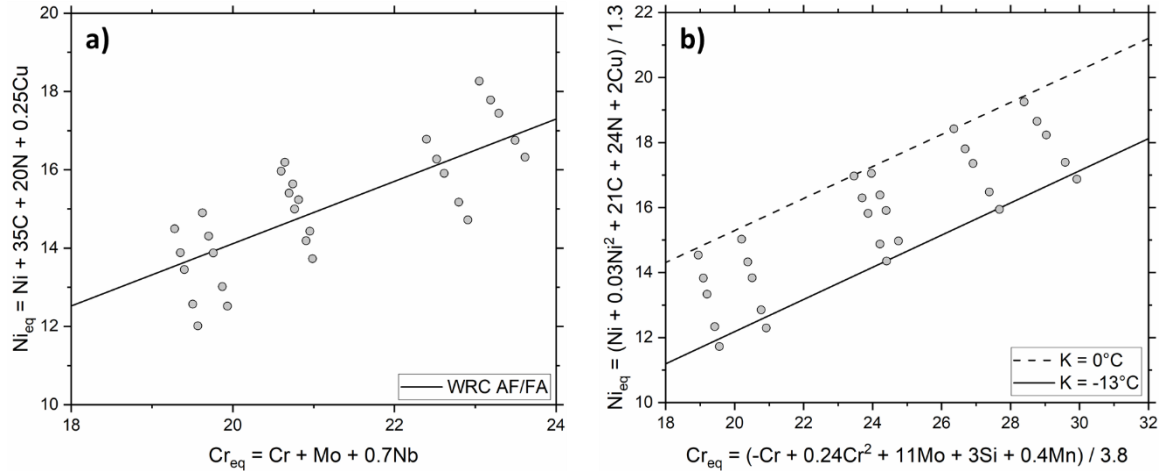


Figure 37: Targeted experimental stainless steel compositions plotted on the a) WRC-1992 diagram, and b) new primary solidification mode diagram ($\Delta T_{L,2}$ equivalencies)

Wires were cut into small segments and weighed to create a total mass of 200g for each targeted chemistry. The wire segments for each mixture were subsequently cleaned in an ultrasonic bath of ethyl alcohol.

Each 200g mixture was then melted in an Arcast Inc. Arc200 cold crucible arc melting furnace with an integrated tilt casting system. All melting and casting were performed in an ultrahigh purity Ar atmosphere. Each mixture was melted in the crucible a total of three times, where the sample was flipped in between each melting cycle to ensure adequate mixing of the parent materials. After the third melting cycle, the tilt casting system was used to pour the molten charge into a Cu mold to form small ingots that were 25 mm in diameter. Following casting, each small ingot was cut into 25 mm x 6.4 mm thick pucks via wire EDM. The EDM recast layer on each puck surface was mechanically removed to expose clean metal. The samples were then thoroughly cleaned with ethyl

alcohol prior to welding. Pictures of the arc melting furnace, crucible with integrated mold, and sectioned samples are presented in Figure 38.

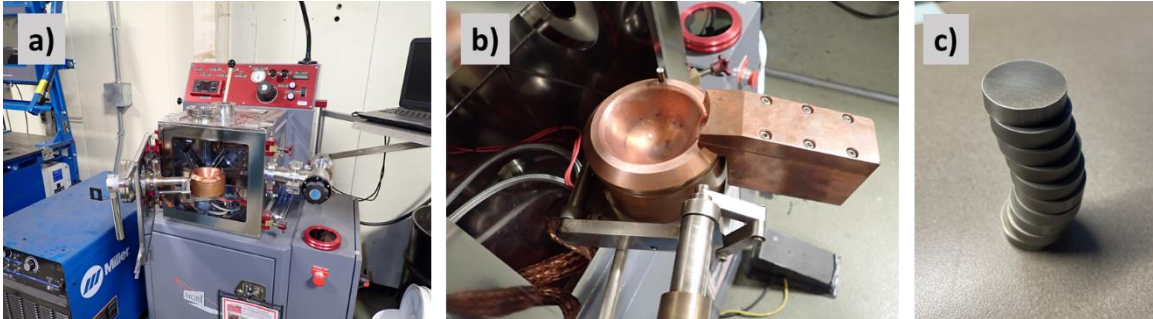


Figure 38: a) Arc melting furnace with integrated tilt casting system; b) water-cooled Cu crucible for melting material with casting mold attachment; c) finished 25 mm dia. x 6.4 mm thick stainless steel samples

Spot Welding Procedure Development

Gas tungsten arc spot welds were used to generate a controlled solidification microstructure on each sample. A stainless steel clamping fixture was used to secure each puck to a thick Cu backing piece as shown in Figure 39. The gas tungsten arc welding torch was then positioned over the center of the exposed puck surface. A Liburdi Dimetrics P300 gas tungsten arc welding system was used with a 1/8" 2% lanthanated electrode (20° included angle, 0.04" blunt tip) operating with DCEN polarity. Gas shielding was provided through a 1" Pyrex gas diffuser with standard grade Ar at a flowrate of 75 cfh.

Welding trials were performed on 304L test samples to determine a suitable set of welding parameters. Welding trials consisted of initiating the arc, stabilizing the weld pool at 150 A and 11.5 V, dwelling for 10 s, and down sloping the current at various rates (5 A/s, 10 A/s, and 20 A/s) to induce solidification. A Xiris Automation welding camera was focused on the spot weld surface to monitor weld pool behavior during the melting and solidification cycles. The welding camera can be seen in Figure 39 positioned above the fixture.

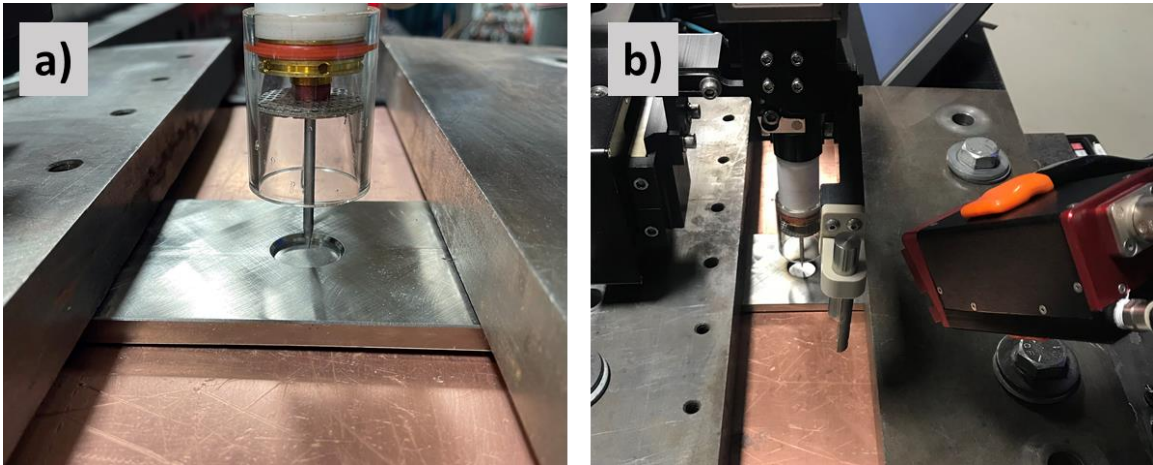


Figure 39: a) spot welding fixture and gas tungsten arc welding torch; b) welding camera positioned to monitor weld pool motion

Significant weld pool oscillations resulted in an unsteady solidification front during each of the controlled downslope trials. Provided that the solid-liquid interface velocity is a key parameter that controls phase selection during the solidification of austenitic stainless steels, the weld pool oscillations were deemed unacceptable for the current study as they could not be sufficiently controlled while the welding current was gradually decreased.

Conversely, simply extinguishing the arc after the 10 s dwell time resulted in a consistently uniform solidification front. Therefore, no downslope was used for the remainder of the investigation.

A second welding camera (Cavitar C300) that utilizes laser illumination was used to measure the solidification front velocity of the weld pool. While the first welding camera provided sufficient clarity to monitor weld pool motion during the downslope trials, it was difficult to track the solid-liquid interface once the arc was extinguished. The second welding camera provided sufficient contrast after the arc was extinguished to track the solid-liquid interface position as a function of time.

Sample Characterization

Chemical analysis was performed on a representative sample from each melt that was taken as close to the spot weld sample as possible using a SPECTROMAXx OES system. A minimum of three measurements were taken from each sample. A 304L stainless steel reference standard was used prior to all measurements to ensure the OES system was functioning properly. A 316L stainless steel reference sample was used for the 330-316L and 330-316LSi compositions. A summary of all chemical analysis results can be found in Appendix B.

Spot weld samples were mounted to expose the top weld pool surface for metallographic analysis. This orientation was selected so the imaging plane approximately coincided with the weld pool velocity measurements that were taken. Samples were prepared using standard metallographic grinding/polishing procedures down to a 0.04 μm

colloidal SiO₂ finish. After polishing, samples were electrolytically etched with a 60% HNO₃ / 40% distilled water solution at 2 V. Etching times varied between 15 to 30 s to reveal the microstructure of the spot welds.

Microstructure characterization was performed using an Olympus GX-51 light optical microscope. Samples were imaged using brightfield and differential interference contrast imaging modes at magnifications ranging from 12.5 to 1000X. It was found that differential interference contrast imaging was particularly useful to identify the primary solidification mode by identifying the location of ferrite relative to the solidification grain boundaries.

Thermodynamic Calculations and Dendrite Growth Simulations

Thermodynamic Calculations

Multicomponent thermodynamic calculations were performed using Thermo-Calc version 2021a with the TCFE11 Steels/Fe-alloys database. The average measured chemical compositions for each sample were used to calculate the stable and metastable liquidus temperatures (T_L) for austenite and ferrite, the equilibrium solidification partition coefficients (k) for all elements in austenite and ferrite, and the liquidus slopes (m) for all elements in austenite and ferrite. These calculations were performed by considering only austenite and liquid or only ferrite and liquid. All other phases were suspended for the thermodynamic calculations.

Dendrite Growth Simulations

Dendrite growth simulations were performed for each alloy using the multicomponent KGT model as described in Chapter 2 [59, 82]. Dendrite tip temperature solutions were developed for austenite and ferrite independently as functions of the initial chemical composition, temperature gradient, and dendrite tip velocity. The chemical composition-dependent variables were captured by the thermodynamic calculations results (T_L , k , and m) mentioned in the previous subsection and assumed to be constant for each sample. The temperature gradient at the solid-liquid interface was inferred by relating it to the measured solidification velocity and primary dendrite arm spacing using the empirical relationship presented by Katayama [95]. The primary dendrite arm spacing was determined through metallographic analysis, and the solidification velocity was determined via spot weld solidification videos using a 304L test sample. Other input parameters were taken from literature [59, 82]. The Gibbs-Thomson coefficient, Γ , for austenite and ferrite were assumed to be equal to $3.2 \cdot 10^{-7} \text{ m} \cdot \text{K}$ and $2.6 \cdot 10^{-7} \text{ m} \cdot \text{K}$, respectively [59]. Solute diffusivity in the liquid was assumed to be constant and equal to $5 \cdot 10^{-9} \text{ m}^2/\text{s}$ for all elements [82]. Cellular undercooling and kinetic undercooling contributions were ignored since they only contribute at low and high solidification velocities, respectively [74].

Results and Discussion

Solidification Front Velocity

The solidification front velocity measurement results from a 304L gas tungsten arc spot weld test sample can be found in Figure 40. Figure 40 also presents individual frames of the spot weld immediately after the arc was extinguished, approximately halfway through the solidification sequence, and at the end of solidification. A recurring issue that occurred while monitoring the solidification front was that debris would be swept into the center of the solidifying weld pool surface. This prevented taking measurements at the terminal stages of solidification. The debris can be seen in Figure 40 at the center of the solidified spot weld. As seen in Figure 40, the solidification front position was linear with respect to time within the measured range. The measured solidification velocity was approximately 3.7 mm/s.

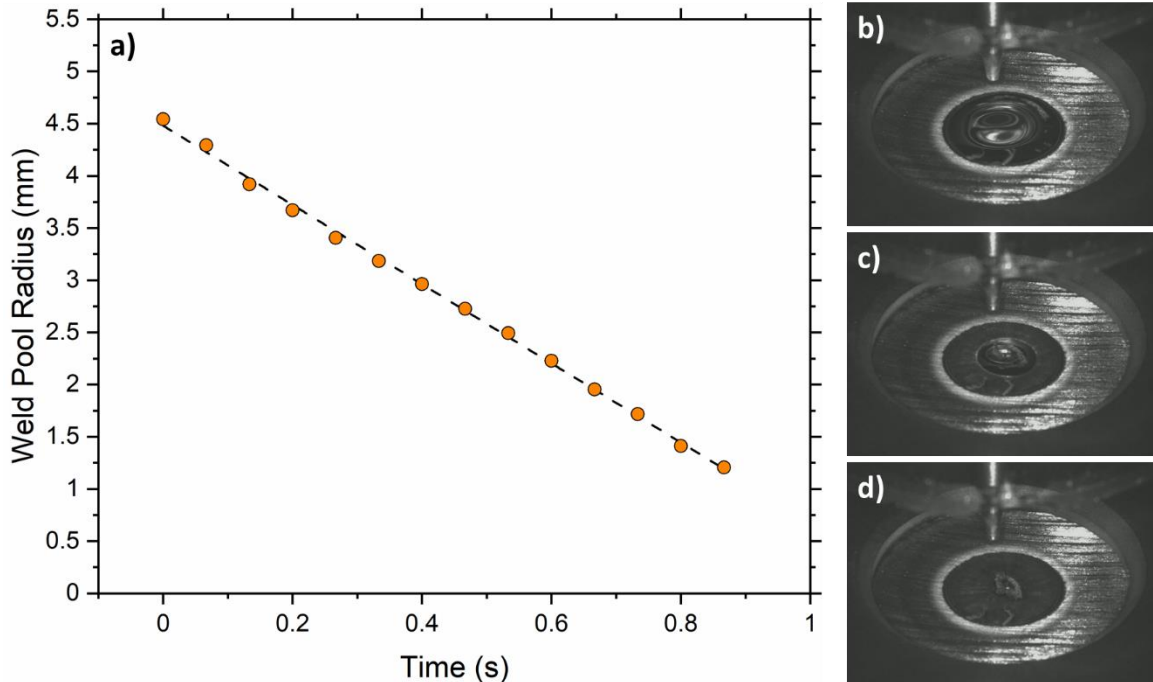


Figure 40: GTAW spot weld solidification front velocity analysis; a) weld pool radius as a function of time; b) image of weld pool immediately after the arc was extinguished; c) image of partially solidified weld pool; d) image of fully solidified weld pool

Microstructure Analysis

The 304L test sample that was used to measure the solidification front velocity in Figure 40 was also used to determine an approximate primary dendrite arm spacing for later dendrite growth modeling. To do so, regions of columnar dendritic grain growth that were oriented parallel to the radial direction of the spot weld were analyzed. A representative micrograph from this exercise can be found in Figure 41.

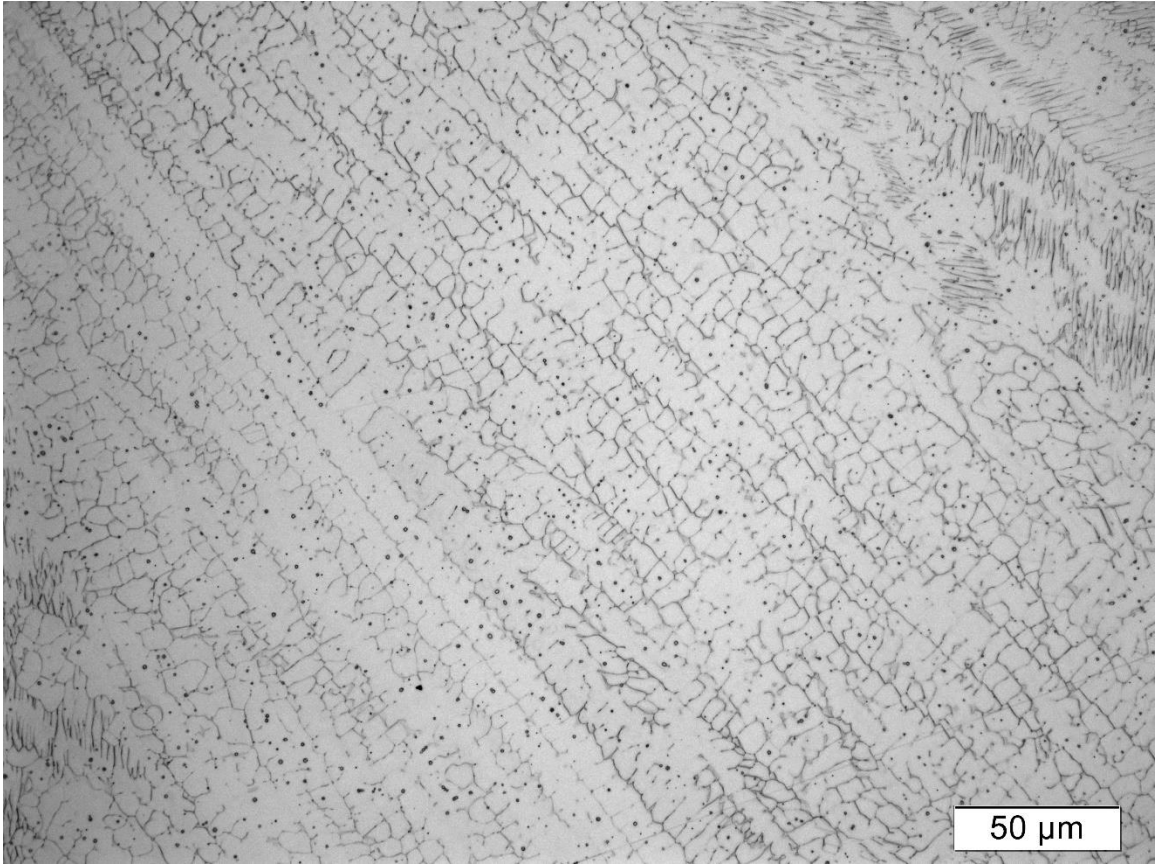


Figure 41: Representative GTAW spot weld microstructure from a 304L test specimen

The 304L test sample exhibited a skeletal ferrite structure that is indicative of primary ferrite solidification, where nearly continuous strips of ferrite were observed along the core of the original solidifying dendrites. Primary dendrite arm spacing measurements were on the order of 10 to 14 μm. Therefore, an approximate average primary dendrite arm spacing was assumed as 12 μm. The temperature gradient at the solid-liquid interface was found using the relationship between primary dendrite arm spacing and solidification conditions presented by Katayama [95]:

$$\lambda_1 = 80(G * V)^{-0.33}$$

where λ_1 is the primary dendrite arm spacing in μm , V is the solidification velocity in m/s , and G is the temperature gradient in the liquid ahead of the solid-liquid interface in $^\circ\text{C/m}$. The temperature gradient ahead of the solidification front was found to be 8.4×10^4 $^\circ\text{C/m}$. The solidification front velocity and temperature gradients found here are in reasonable agreement with similar spot welding experiments and computational heat and fluid flow modeling performed by Babu and Zhang on steels [82, 96].

A distinct change in solidification structure was apparent near the central region of each spot weld. To investigate this region further, a ER308L-ER330 spot weld sample (8L30F13) that exhibited primary ferrite solidification was cross sectioned for metallographic analysis. This analysis revealed that the central region of the spot weld surface contained a combination of columnar dendrites that were growing approximately normal to the weld pool surface and equiaxed dendrites. The columnar dendritic structures were simply extensions of subsurface dendrite growth that were revealed when the samples were analyzed in plan view. Presumably, the equiaxed region at the center of each spot weld was due to the columnar to equiaxed transition. Example micrographs from sample 8L30F13 showing this region can be found in Figure 42, where a mixed morphology zone (MMZ) is identified.

Zhang showed that the temperature gradient at the solidification front of steel gas tungsten arc spot welds continuously decreased after the arc was extinguished and the solidification front progressed, where G decreased by a factor of approximately 2 from the onset of solidification to the end of solidification [96]. In the current study, the solidification velocity was nearly constant within the measurable range. If the temperature

gradient at the solidification front continually decreased as the solid-liquid interface advanced toward the center of the spot weld, the solidification parameter G/V would decrease and move towards stabilizing equiaxed solidification [97]. A more detailed analysis would need to be conducted using an equiaxed dendrite growth model to verify this effect [98, 99].

Additionally, if G continually decreased at a constant V then the length scale of the microstructure (inversely proportional to $G \cdot V$) should continuously increase as the solidification front moved towards the center of the solidifying spot weld. Approximate calculations using Katayama relationship between primary arm spacing and solidification parameters revealed that if G were to decrease by $1/2$, that the primary dendrite arm spacing should increase from $12 \mu\text{m}$ to $15 \mu\text{m}$. This range was within the scatter of primary dendrite arm spacing measurements and no direct correlation could be made with respect to the length scale of the microstructure due to changes in G along the solidification front direction.

Along the outer fusion boundary of some mixed mode and primary ferrite samples there was evidence of localized epitaxial primary austenite nucleation. Figure 42 shows an example of this localized primary austenite formation in sample 8L30F13. Although not investigated here, characterization of the microstructure and solute segregation around the outer edge of the weld pool could be performed to better understand if this localized fusion boundary austenite growth was associated with differences in local solidification conditions, or more likely, macrosegregation in the ingots.

To consistently assess the solidification mode amongst the various samples a circular region of interest (ROI) was identified for optical characterization. As shown in Figure 42, the ROI was defined partway between the edge of the fusion boundary where nucleation effects were occasionally observed and the MMZ region. The ROI region corresponded to the approximate location where the primary dendrite arm spacing analysis was performed and was within the region that interface velocity measurements were taken. Additionally, the outer edge of the ROI was well inside an estimated initial transient regime with respect to solute partitioning in the early stages of solidification. The length of the initial solute transient can be approximated using the equation [100]:

$$5x_c = \frac{5D_L}{kV}$$

where $5x_c$ approximates the length of the initial solute transient, D_L is the solute diffusivity in the liquid, k is the equilibrium solid-liquid solute partition coefficient, and V is the solid-liquid interface velocity. Solute diffusivity in the liquid is on the order of 10^{-9} to 10^{-8} m²/s, and equilibrium partition coefficients are around 0.8 to 1 for substitutional elements and 0.2 to 0.4 for interstitial elements [97]. With the measured solidification velocity, the width of the initial transient would be on the order of tens of microns.

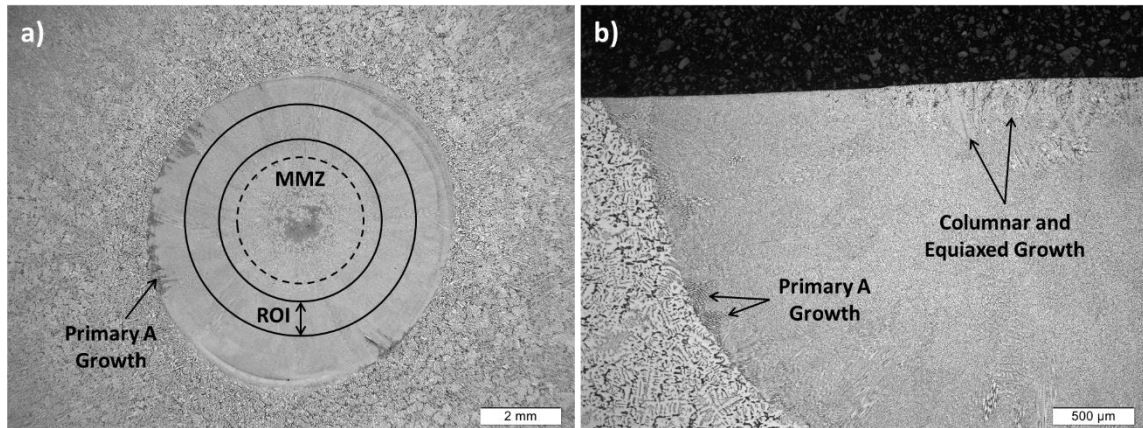


Figure 42: Sample 8L30F13 spot weld; a) plan view micrograph showing MMZ region, localized primary austenite growth along the fusion boundary, and ROI for solidification mode analysis; b) cross section view showing subsurface localized austenite growth along the fusion boundary and the typical columnar and equiaxed grain morphologies that were at the center of each spot weld within the MMZ

Metallographic analysis revealed that most of the spot weld microstructures exhibited primary austenite solidification. Representative micrographs of each solidification mode are presented in Figures Figure 43 through Figure 45. Each sample presented in Figures Figure 43 through Figure 45 came from the ER316L-ER330 series of stainless steel mixtures. As seen, there is a distinctive etching response in the spot welds associated with the active solidification mode. This is most apparent by looking at the mixed mode solidification structure presented in the low magnification micrograph of Figure 44, where regions of primary austenite and primary ferrite growth are indicated. Most of the primary ferrite solidification structures that were characterized exhibited a skeletal ferrite morphology, although lathy ferrite structures were occasionally observed. A summary of the observed experimental solidification modes for each sample can be

found in Appendix B. Low magnification micrographs for each sample are also presented in Appendix C. The experimentally determined solidification modes are also presented on the WRC-1992 and new primary solidification mode diagrams using the target chemical compositions in Figure 46.

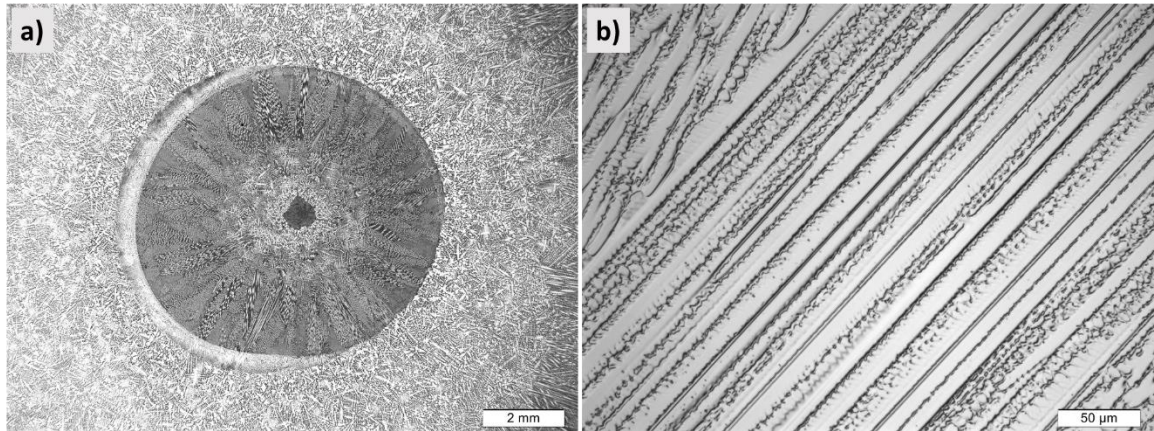


Figure 43: Micrographs from sample 16L30F5 that solidified as primary austenite; a) low magnification; b) high magnification

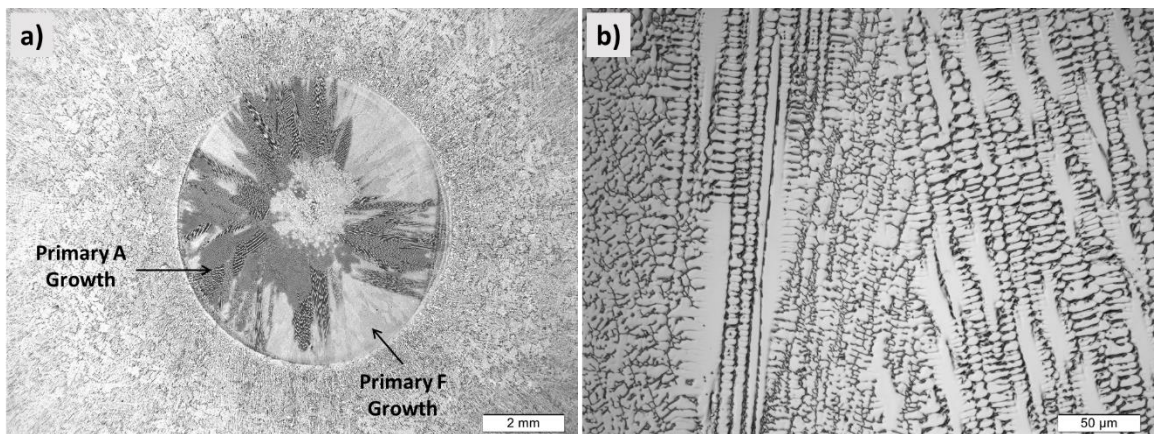


Figure 44: Micrographs from sample 16L30F10 that exhibited mixed mode solidification; a) low magnification; b) high magnification

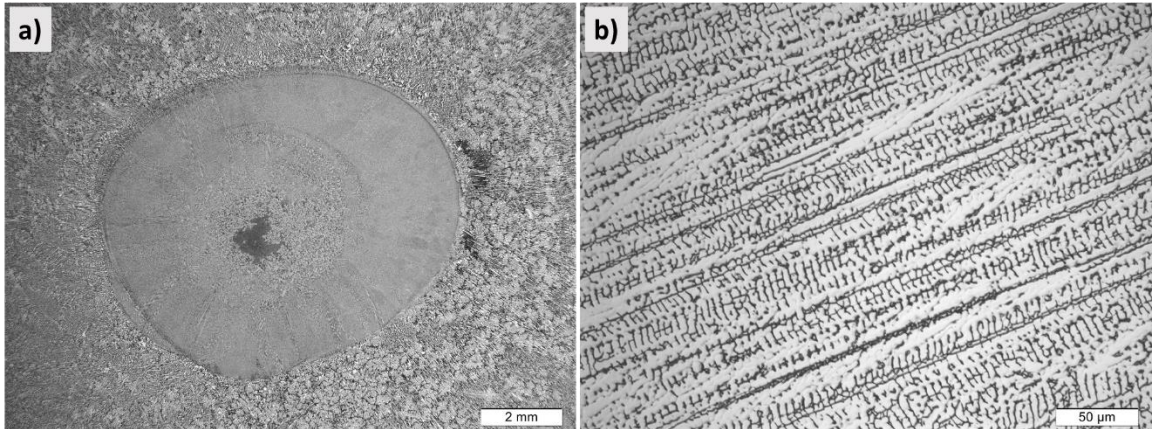


Figure 45: Micrographs from sample 16L30F13 that solidified as primary ferrite; a) low magnification; b) high magnification

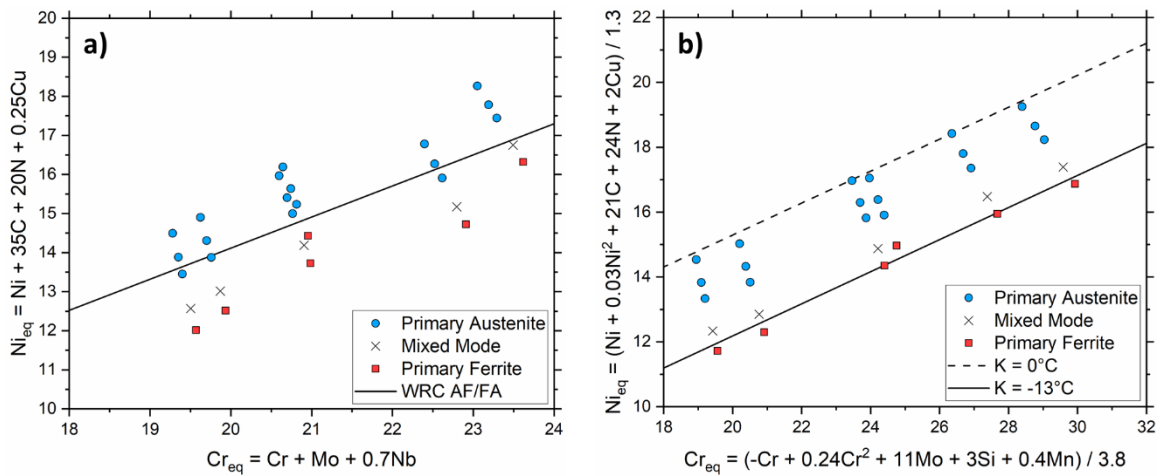


Figure 46: Experimentally determined solidification mode for each sample plotted using the target chemical composition data on the a) WRC-1992 diagram; and b) new primary solidification mode diagram ($\Delta T_{L,2}$ equivalencies)

Chemical Analysis and Measurement Uncertainty

The average chemical concentrations and standard deviation values for each element in each sample were used to perform Monte Carlo sampling to demonstrate the effect of measurement uncertainty on the position of each sample on the WRC-1992 and new primary solidification mode diagram. Similar to the approach presented in Chapter 4, normal distributions were created for each element in each sample that were described by the average measured concentration and standard deviation values that were determined through OES analysis. Each normal distribution was then randomly sampled to create chemical compositions for each sample that fall within the statistical uncertainty for the measurements. A total of 1000 Monte Carlo sampling iterations were performed for each experimental composition. The Monte Carlo sampling results are presented in Figure 47, where the size of each colorized cluster around the average measured chemical composition of each sample is indicative of the measurement uncertainty associated with the OES results that has been propagated onto each equivalency space. The average measured chemical compositions were also used to plot the experimentally determined solidification mode for each sample in Figure 48 for comparisons with Figure 47.

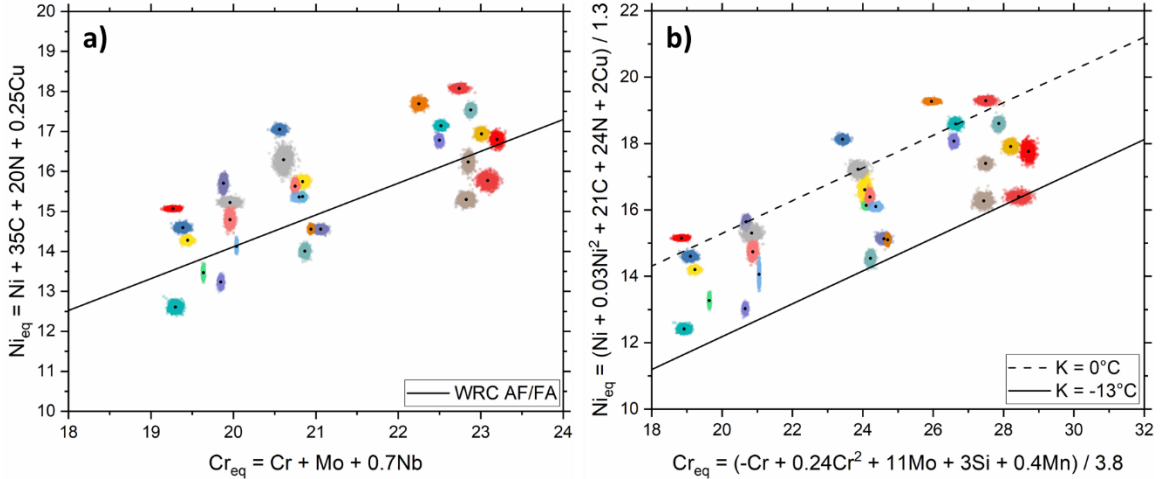


Figure 47: Monte Carlo sampling results showing the effect of chemical analysis uncertainty propagation for each experimental composition on the a) WRC-1992 diagram; and b) new primary solidification mode diagram ($\Delta T_{L,2}$ equivalencies)

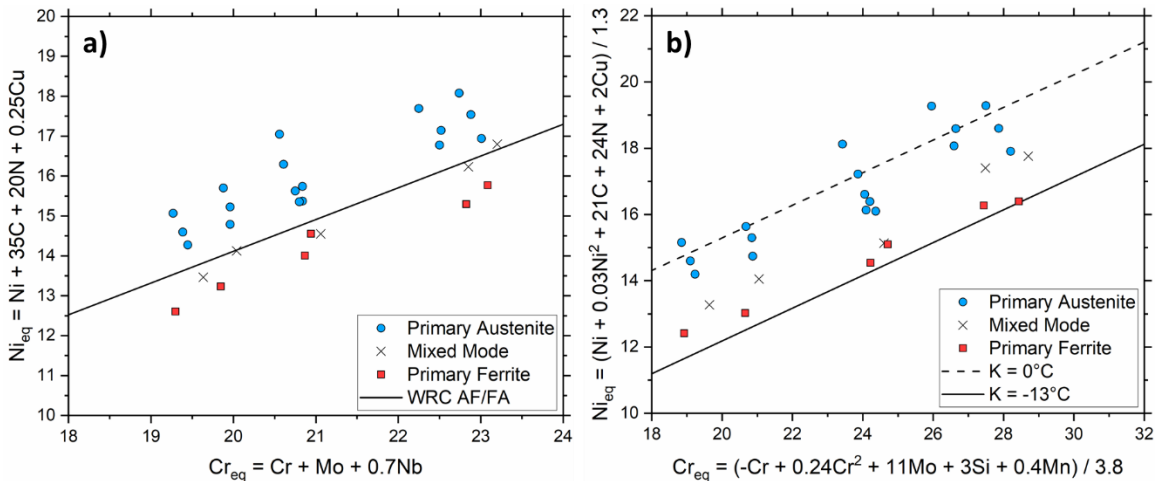


Figure 48: Experimentally determined solidification mode for each sample plotted using average experimental chemical analysis data on the a) WRC-1992 diagram; and b) new primary solidification mode diagram ($\Delta T_{L,2}$ equivalencies)

As seen, uncertainty in chemical analysis has a marked effect on the likely position of each sample on each diagram. This exercise highlights two key aspects of using predictive tools that are reliant on chemical analysis for austenitic stainless steel weld metal solidification behavior.

First, by comparing Figures Figure 46 and Figure 47, differences are observed between the targeted chemical compositions that were developed using certified material test reports and the average chemical compositions that were determined via OES analysis. These discrepancies can originate from four sources:

1. Variability in the precision and accuracy of the analytical instruments that were used between the labs that created the original material test reports and the OES instrument used here
2. Differences between the heat analysis presented on the material test reports and the actual chemistry of the filler materials that were used
3. Experimental error associated with measuring precursor materials to fabricate the small ingots and the melting process
4. Homogeneity of the ingots

While the specific source(s) of the differences between the target compositions and the measured compositions was not determined for this investigation, it highlights that simply relying on material test report data may not be adequate.

Secondly, similar to the analysis presented in Chapter 4, chemical analysis uncertainty can cause the error bars (or Monte Carlo sampling clusters in this case) for a given chemical composition to span across solidification mode boundaries. This is

obviously problematic if an accurate primary solidification mode prediction is required for a given application. Note that this effect is not unique to the primary solidification mode diagrams and is more broadly applicable to tools such as weld metal constitution diagrams and CALPHAD-based solidification simulations. Furthermore, it brings into question empirically derived diagrams where boundaries are constructed based on average chemical composition measurements with no indication of the underlying uncertainty of the experimental data.

Considering Figure 48, both the WRC-1992 and new primary solidification mode diagram perform similarly with respect to predicting the solidification mode of the experimental spot welds using the measured OES data. In this case, it seems that the lower bounding K value for the new primary solidification mode diagram needs adjusted to account for the specific stainless steel compositions and solidification conditions that were studied. As shown in Figure 49, better agreement between the predicted and observed solidification modes for the experimental alloys can be achieved by adjusting the K values between -6°C and -12°C using the equations presented in Table 2. It's not surprising that an adjustment to the diagram was necessary considering that the original boundary that separated the (A+F) and F regions of the new diagram was defined using a minimum ΔT_L from the subset of WRC Appendix II database compositions that exhibited metastable austenite growth. Considering that the necessary shift is in the direction of less negative K values, it cannot be attributed to differences in dendrite growth kinetics since the experimental solidification front velocity is fairly high for traditional fusion welding travel speeds. If the shift was attributable to differences between the dendrite growth kinetics

(i.e., undercooling at the dendrite tips) of the WRC Appendix II data and the experimental alloys, an increase in solidification velocity would push the boundary to more negative K values [59, 64]. A more likely explanation is related to chemical analysis uncertainty within the original WRC Appendix II data, where any variability in the reported compositions would cause the calculated ΔT_L to change based on the performance of the analytical techniques that were used, as shown in Figure 47.

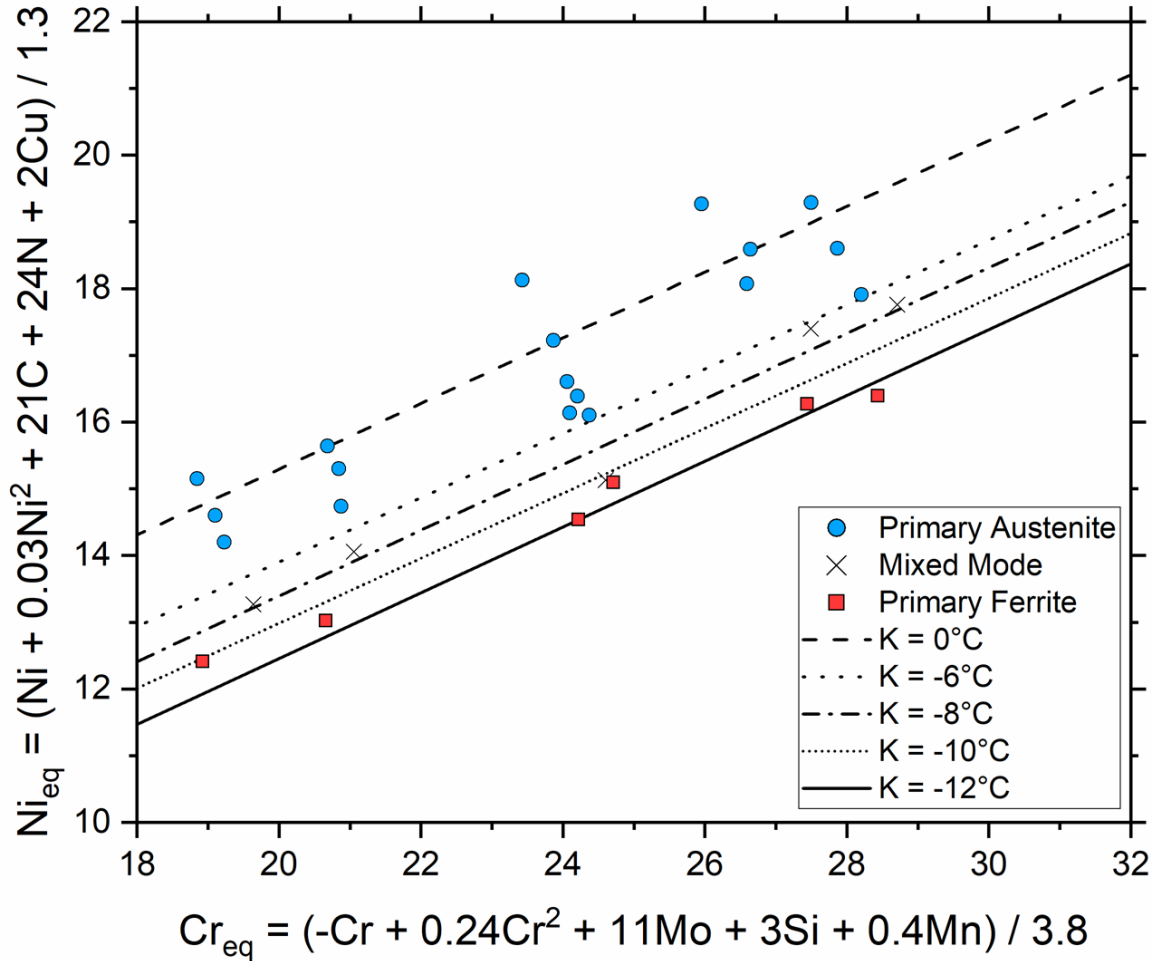


Figure 49: Experimentally determined solidification mode for each sample plotted using experimental chemical analysis data on the new primary solidification mode diagram with various K values ($\Delta T_{L,2}$ equivalencies)

Dendrite Growth Kinetics

Multicomponent KGT model (dendrite tip temperature) solutions were obtained for each of the experimental alloys as a function of solidification velocity using the inferred temperature gradient at the solid-liquid interface and calculated composition-dependent thermodynamic parameters. The dendrite growth model data at the experimentally

determined solidification velocity is presented in Figure 50, where the position of each alloy on the diagram is given by the difference in undercooling for ferrite and austenite on the horizontal axis and difference in liquidus temperatures for austenite and ferrite on the vertical axis. The experimentally observed solidification mode data is also presented.

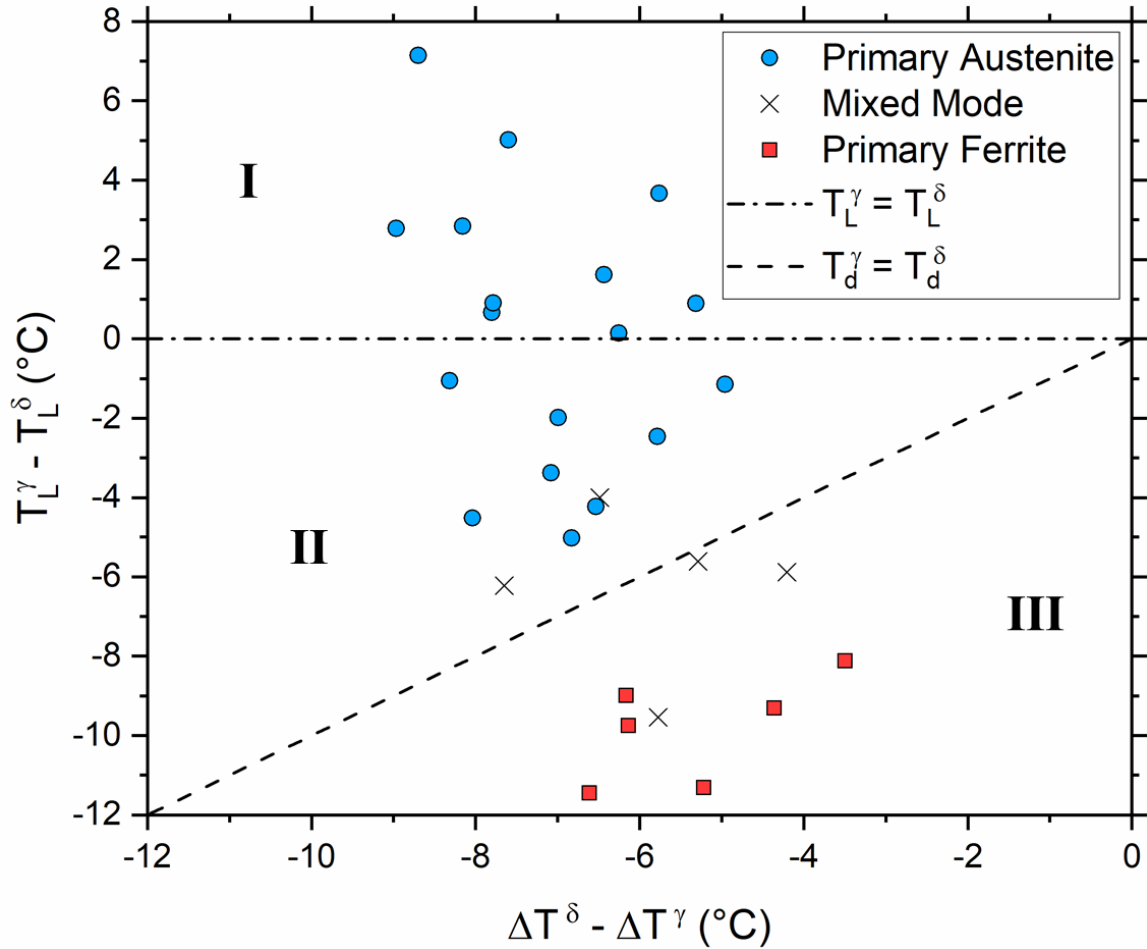


Figure 50: Dendrite growth temperature solutions and experimentally observed solidification modes for the experimental alloys

Two boundaries are also presented in Figure 50 that separate the alloys by their dendrite growth behavior. The upper boundary in Figure 50 represents chemical compositions where austenite and ferrite liquidus temperatures are equal. The lower boundary represents the condition where the dendrite tip temperatures for austenite and ferrite are equal, that is, the difference in liquidus temperatures is equal to the difference in undercooling for austenite and ferrite. Region I of Figure 50 represents stable primary austenite growth where both the thermodynamic and kinetic response of an alloy system promote austenite stability. Region I corresponds to Type 1 austenitic stainless steels in the classification system that was proposed in Chapter 4. Region II represents the regime of metastable primary austenite growth, where the liquidus temperature of austenite is lower than that of ferrite but dendrite growth kinetics favor austenite growth. Region II corresponds to Type 3 alloys from Chapter 4. Finally, Region III represents stable primary ferrite growth, where the ferrite liquidus temperature is sufficiently higher than the austenite liquidus temperature to overcome growth kinetics that favor austenite growth. Region III corresponds to Type 4 alloys from Chapter 4. Note that changes in solidification velocity will cause the data points to translate left or right on the diagram. If the solidification velocity is decreased, the difference in undercooling between ferrite and austenite will decrease and shift the alloys in the positive direction. Conversely, if the solidification velocity is increased the difference in undercooling between austenite and ferrite will also increase, causing a shift in the negative direction towards austenite stability. Therefore, the classification of alloys in Region III (Type 4 alloys) is only applicable up to

a maximum solidification velocity, beyond which, metastable primary austenite solidification is expected when the alloy crosses into Region II (Type 3 alloys).

Figure 50 also demonstrates that, based on dendrite growth kinetics, a range of ΔT_L values should be expected to describe the transition region between primary austenite and primary ferrite on the new predictive primary solidification mode diagram when multiple alloys are considered. Comparing the position of the data on Figure 50 with the chemical analysis data revealed that as Cr_{eq} and Ni_{eq} increased, the difference in liquidus temperatures and undercoolings that satisfied the condition where the austenite and ferrite dendrite tip temperatures were equal shifted to more negative values. In other words, K should be more negative at higher Cr_{eq} and Ni_{eq} values. Based on Figure 50, the range of K values across the analyzed composition space should be approximately $4^\circ C$. Therefore, a variable K correction has been applied to the primary solidification mode diagram and is presented in Figure 51. Although the K range of $4^\circ C$ is consistent with dendrite growth simulations, the actual position of the boundary was chosen to best fit the experimental solidification mode data. Additional solidification mode experiments on alloys near the boundary would be necessary to determine if this estimated location is too low on the diagram. Regardless, this exercise demonstrates the flexibility of the new primary solidification mode diagram.

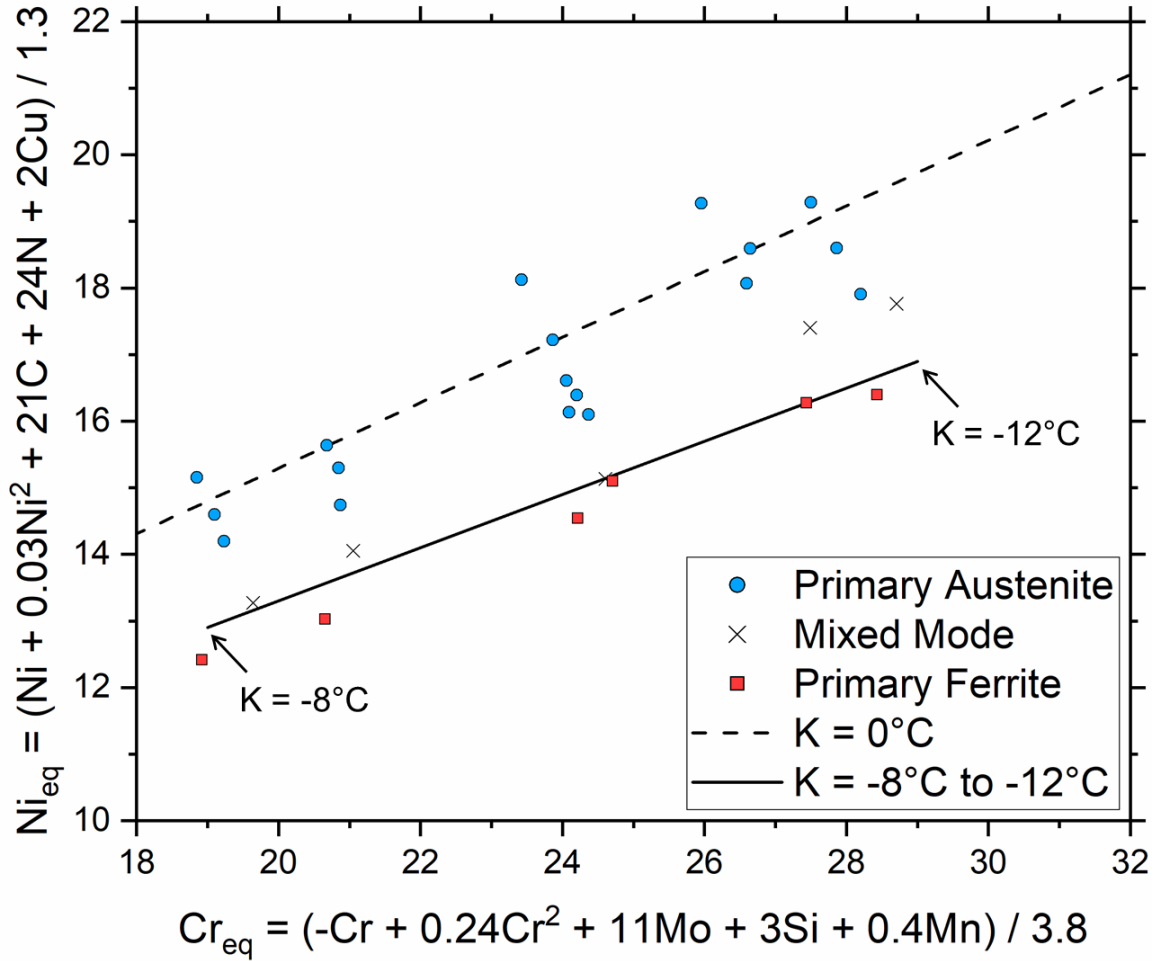


Figure 51: Average experimental compositions plotted on the new primary solidification mode diagram with a variable K correction for the lower growth mode transition boundary

Conclusions

An experimental investigation was performed to assess the performance of a newly developed primary solidification mode diagram for austenitic stainless steel weld metals using an independent dataset across a wide range of Cr_{eq} and Ni_{eq} values. The experimental

investigation was supplemented with solidification mode predictions from the WRC-1992 diagram and dendrite growth model simulations. The conclusions from this effort can be summarized as follows:

- Controlled experimental compositions were effectively created using an arc furnace casting technique by mixing precursor wires of commercially available stainless steel filler materials. This allowed weld metal chemistries to be efficiently targeted that spanned across the primary austenite / primary ferrite solidification transition.
- Using gas tungsten arc spot welding experiments, the weld metal microstructure was controlled under relatively constant solidification conditions. It was found that amperage down sloping was not suitable to produce a stable solidification front within the tested range of welding parameters. Extinguishing the arc after a controlled arc dwell cycle produced a constant solidification velocity within the spot welds. The solid-liquid interface was effectively tracked during the melting and solidification sequences using a through arc welding camera that utilized laser illumination.
- Nucleation effects along the fusion boundary and a transition to equiaxed solidification near the center of the gas tungsten arc spot welds was consistently observed. As such, a method was developed to characterize the solidification mode of the gas tungsten arc spot welds that were explored here in a consistent way. Localized epitaxial austenite growth along the fusion boundary was attributed to solute macrosegregation in the test samples, although additional experiments are required for verification.

- It was found that the predictive ability of the WRC-1992 and new primary solidification mode diagrams were similar. This was particularly true after the new solidification mode diagram was modified using the previously presented K value equations. This exercise demonstrated the utility of the new diagram to formulate corrections for experimental data that are consistent with dendrite growth theory rather than simply drawing arbitrary line locations on a predictive diagram.
- The observed primary solidification modes of the experimental alloys agreed with dendrite growth simulations. Dendrite growth model data suggests that the K values used to define the lower boundary on the primary solidification mode diagram is dependent on chemical composition. Specifically, K values are expected to be more negative at higher Cr_{eq} and Ni_{eq} values to describe the lower boundary on the new solidification mode diagram. This information was used to apply a variable K correction to the primary solidification mode diagram.
- The use of Monte Carlo sampling to propagate chemical analysis uncertainty onto the WRC-1992 and new primary solidification mode diagrams for individual samples was demonstrated. Users of composition dependent predictive diagrams for austenitic stainless steel weld metal solidification behavior need to account for such chemical analysis uncertainty when average compositions fall near a boundary of interest.

Chapter 6. Concluding Remarks and Opportunities for Future Work

Summary

Through this work, it has been demonstrated that computational thermodynamic solidification simulations that rely on equilibrium phase diagram calculations do not accurately describe primary phase selection for austenitic stainless steel weld metals in all cases. Discrepancies exist for alloys with chemical compositions that sit near the intersection of the equilibrium austenite and ferrite liquidus surfaces. More specifically, metastable primary austenite growth is consistently observed for alloy compositions that should solidify as primary ferrite based on equilibrium phase diagram predictions. Metastable primary austenite growth in stainless steel weld metals has traditionally been associated with welding processes that induce high solidification velocities and temperature gradients such as laser welding and electron beam welding. This work, however, demonstrates that metastable primary austenite growth is not unique to high energy density welding processes for chemical compositions that are relevant to commercially available austenitic stainless steel chemistries. In fact, metastable austenite growth is observed in stainless steel weld metals during conventional fusion welding conditions. This was validated through thorough computational thermodynamic assessments of legacy experimental data, randomized stainless steel chemistries, and independent spot welding experiments.

Given the maturity of thermodynamic databases for steels and the integration of solidification models into commercially available computational thermodynamic software packages, one might naturally assume that a thermodynamic solidification simulations (such as those performed with equilibrium or Scheil solidification models) should provide a more accurate prediction for the primary solidification mode of a given austenitic stainless steel weld metal chemistry. This work demonstrates that this is not true for all stainless steel compositions and, unfortunately, the discrepancies between solidification simulations and experimental results are in a non-conservative direction with respect to solidification cracking susceptibility. That is, computational thermodynamic predictions may predict primary ferrite solidification while metastable primary austenite growth may be observed experimentally.

Although discrepancies exist between thermodynamic predictions and experimental evidence for alloys that exhibit metastable primary austenite growth, the utility of using computational thermodynamic calculations to populate the requisite data to construct chemical equivalency relationships and predictive diagrams has been established. A new solidification metric (ΔT_L) has been defined that can be related to dendrite growth theory using stable and metastable liquidus temperature calculations for austenite and ferrite. By defining a suitable set of concentration limits for stainless steel chemistries of interest, computational thermodynamic calculations can be used to populate a database of randomly generated chemical compositions and their ΔT_L values. Populating the data in this way avoids multicollinearity amongst alloying additions that is inherent to many experimental weld metal studies. The database of randomized chemical compositions

within the designed concentration limits can then be used to construct statistical models that describe ΔT_L as a function of chemical composition. In this case, multiple regression has been employed to facilitate the construction of Cr_{eq} and Ni_{eq} expressions. The ΔT_L values from the randomized database can then be projected onto a diagram where the Cr_{eq} and Ni_{eq} expressions serve as the horizontal and vertical axes, respectively. An upper boundary can be defined on the diagram that identifies the equilibrium transition between austenite and ferrite in a multicomponent composition space. With supplemental solidification experiment data, the location of the metastable primary austenite / primary ferrite boundary on the diagram can be defined. This method offers a distinct advantage over a strictly experimental approach because it drastically reduces the number of unique experimental weld metal chemistries that need to be investigated. In the case of a fully experimental approach, a sufficient number of unique weld metal chemistries need to be considered to facilitate statistical model construction and identify the location of transitions on the diagram. Additionally, calibrations of the diagram can provide an indication for how much higher the ferrite liquidus temperature needs to be than the austenite liquidus temperature to offset growth kinetics that favor metastable austenite growth. On the new diagram, this is facilitated by providing tabulated calibration equations for a range of ΔT_L values that can be applied in situations where growth kinetics differ from those explored here. Specifically, this can be useful when typical 300 series stainless steels are welded with solidification velocities greater than what were explored in this investigation but still within the columnar dendritic growth range.

A new classification scheme to describe austenitic stainless steel weld metals has also been proposed. The classification scheme was constructed by considering the liquidus temperatures of austenite and ferrite as well as growth kinetics which consistently favor austenite growth. Using this scheme, four austenitic stainless steel weld metal types were defined within the dendritic growth regime. Type 1 alloys are those which exhibit stable austenite growth. Type 2 alloys describe the specific case where the austenite and ferrite liquidus temperatures are equal and austenite growth is favored. Type 3 alloys are distinguished by stable ferrite growth at low velocities and metastable austenite growth at high velocities. If the welding travel speed for Type 3 alloys exceeds a critical solidification front velocity, growth-controlled mixed mode solidification is possible. Type 4 alloys describe compositions where the ferrite liquidus temperature is sufficiently higher than the austenite liquidus temperature to promote stable ferrite growth across the full range of solidification velocities considered.

Lastly, the effects of chemical analysis uncertainty on the use of predictive solidification behavior diagrams was presented. Chemical analysis uncertainty is often ignored in practice; however, it has been shown that variability should be expected during single laboratory testing and even more so during interlaboratory testing. Building chemical analysis uncertainty into a predictive solidification diagram seems impractical given that accuracy and bias will differ from lab-to-lab. As a result, users of composition based predictive tools should account for chemical analysis uncertainty if solidification behavior predictions are critical for a given application. Two example techniques have been presented here where 95% confidence intervals can be plotted for a given sample or

Monte Carlo sampling can be performed to propagate chemical analysis uncertainty onto a chemical equivalency space. Furthermore, the boundaries on such diagrams are inherently constructed using chemical analysis data that also had some degree of uncertainty. Therefore, one should expect some degree of variability in close proximity to the boundaries.

Future Research Opportunities

Several follow-on investigations have been identified that naturally stem from the work performed here. These opportunities are summarized below.

1. The use of computational thermodynamic calculations to generate a new primary solidification mode diagram has been demonstrated. In the current study, the composition space that was explored closely mirrored the composition space that was used to construct the original WRC-1998 and WRC-1992 diagrams. While the new diagram exhibits some unique features that allow end users to customize boundaries for their given application and provide insight on solidification kinetics, the predictive ability of the WRC and new primary solidification mode diagrams for conventional fusion welding conditions appears to be quite similar. While this validates the approach that was employed here, it slightly diminishes the value of the new diagram. The process, however, provides value for two scenarios. First, this process can be tailored to composition regimes that are not adequately captured by the WRC diagrams such as for high-N or stabilized stainless steel grades. Secondly, the

process could be applied to a more restricted composition space that falls within the existing chemistry limits to potentially improve accuracy. For example, a diagram could be constructed for a fixed material specification where the allowable composition limits span the austenite / ferrite transition.

2. While the chemical concentration limits that were explored in this investigation are relevant to most common austenitic stainless steel weld metal specifications, additional work should be performed to assess the effect of trace elements that may be present but are generally not reported on material test reports. For example, the certificate of analysis for NIST standard reference material 160b (AISI 316) lists that W is present with an average concentration of 0.11 wt.%. A systematic investigation could be conducted to identify maximum concentration limits for trace elements (W, V, Co, etc.) where they become stable with respect to statistical significance during ΔT_L regression analysis and provide an indication for their potency to stabilize austenite or ferrite solidification.
3. Given that the new process to develop a predictive primary solidification mode diagram is reliant on the CALPHAD methodology, uncertainty exists in the thermodynamic Gibbs energy models. In this investigation, the thermodynamic calculation outputs were considered deterministic. However, recent attention has been given to quantifying the uncertainty of thermodynamic models and propagating that uncertainty through the simulation process to quantify confidence [101, 102]. As such, it seems worthwhile to explore the idea of

uncertainty quantification and propagation with respect to the liquidus temperature calculations and how it might influence both the regression model parameters that were used to construct the equivalency expressions and the positions of boundaries on the solidification mode diagram.

4. During the experimental portion of this investigation there was evidence of solute macrosegregation in the small experimental ingots that manifested itself as localized austenite nucleation along the fusion boundary of some gas tungsten arc spot welds. This effect should be explored further using SEM-EDS or EPMA to determine if macrosegregation was indeed associated with the localized austenite formations. If solute macrosegregation is observed, an experiment should be conducted to determine if the observed mixed mode solidification structures change after a homogenization heat treatment of the base material. If the mixed mode structures change to either fully primary ferrite or primary austenite solidification, this will provide evidence that the mixed mode solidification behavior was nucleation-controlled and not growth-controlled.
5. While high-throughput calculations were used to calculate the ΔT_L parameters to eventually derive equivalency expressions, the end result was strictly based on computational thermodynamics and the diagram needed to be calibrated to account for dendrite growth kinetics. It is possible that full multicomponent KGT simulations could be performed in a high-throughput fashion to develop a set of equivalencies and a solidification mode diagram that accounts for

dendrite growth kinetics. Similar to the convention that was used here to derive ΔT_L , the difference in austenite and ferrite dendrite tip temperatures (ΔT_d) at a given set of solidification conditions could be solved as a function of chemical composition. The condition of $\Delta T_d = 0$ would differentiate between metastable primary austenite growth and stable ferrite growth for that set of solidification conditions. If successful, the process could be repeated for multiple solidification velocities to provide a range of diagrams that could be used based on the welding travel speeds that are used for a given application.

6. Lastly, the regression coefficients for Si and Mn introduced some confusion while constructing the Cr_{eq} and Ni_{eq} expressions. Generally, Si is considered a ferrite stabilizer while Mn is considered an austenite stabilizer for austenitic stainless steel weld metals. Regression analysis results using the ΔT_L solidification parameter placed both elements as ferrite stabilizers in the Cr_{eq} expression, suggesting that adding either element to a stainless steel chemistry will decrease the ΔT_L to stabilize ferrite. Since it was demonstrated that solutal undercooling was the primary factor contributing to dendrite growth kinetics, the so-called growth restriction factor (Q) was calculated for a range of stainless steel compositions consistent with those explored in this investigation. Q provides an indication for the amount of undercooling a given solute will contribute during solidification due to solute partitioning at the solidification front. Q for element i is given as: $Q_i = m_i(k_i - 1)c_{o,i}$ [103]. By calculating Q independently for austenite and ferrite for each solute, they can be plotted to

differentiate austenite stabilizers and ferrite stabilizers based on expected solute segregation behavior as presented in Figure 52. In Figure 52, elements which fall above the 1:1 line on the diagram will act as austenite stabilizers while those below will act as ferrite stabilizers. Additionally, the proximity of elements to the 1:1 line provides an indication for the potency for stabilizing either austenite or ferrite. As seen, both Si and Mn appear as austenite stabilizers in this analysis. Clearly, there is a disconnect between the expected behavior, ΔT_L solidification parameter analysis, and Q analysis of Mn and Si. Additional work is needed to assess the source(s) of these discrepancies.

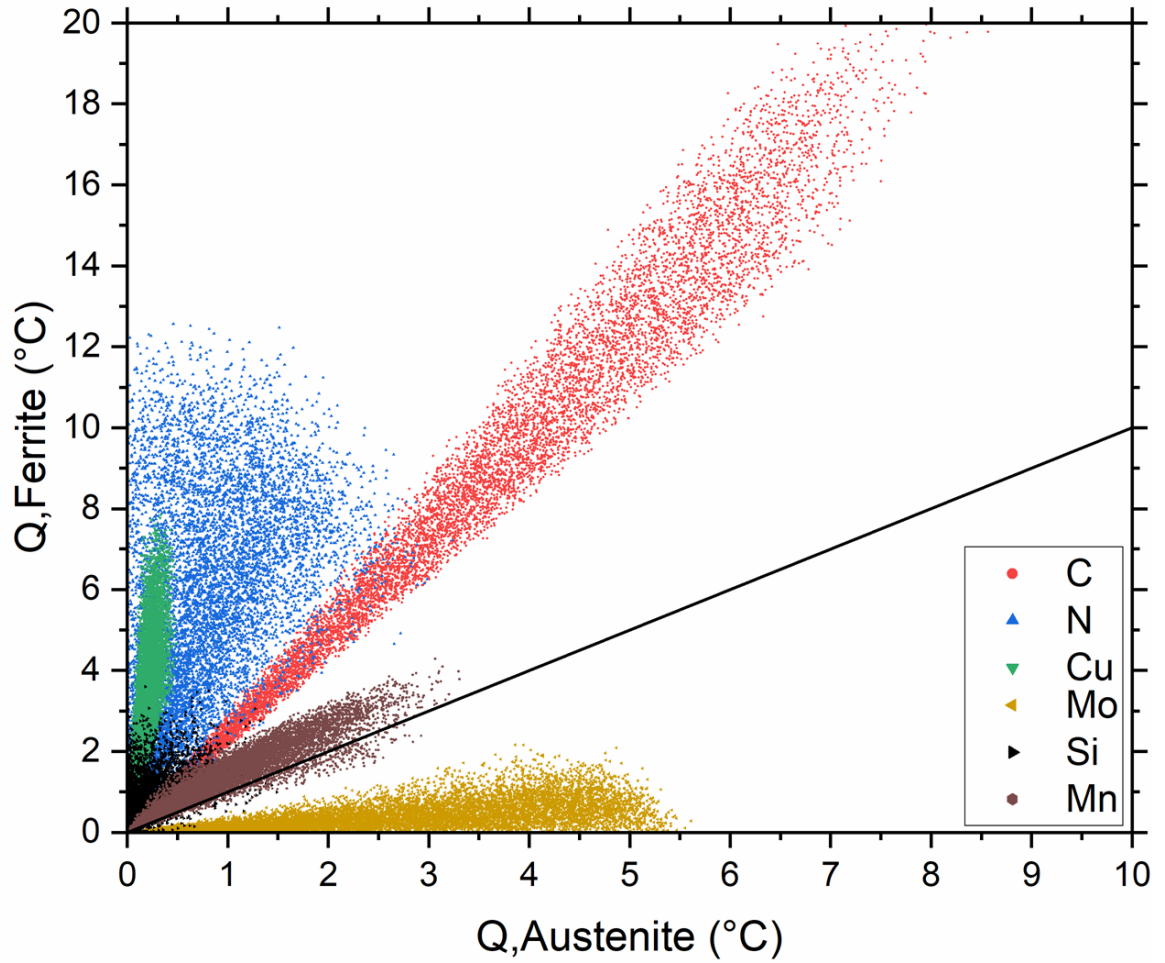


Figure 52: Growth restriction factors for austenite (FCC) and ferrite (BCC) for various solutes in austenitic stainless steels

References

1. ISSF. *Stainless Steel Meltshop Production 2014-2020*. [cited 2021 June 16]; Available from: <https://www.worldstainless.org/statistics/stainless-steel-meltshop-production/stainless-steel-meltshop-production-2013-2019/>.
2. Brooks, J.A. and J.C. Lippold, *Selection of Wrought Austenitic Stainless Steels*, in *Welding, Brazing and Soldering*, D.L. Olson, et al., Editors. 1993, ASM International. p. 0.
3. Lippold, J.C. and D.J. Kotecki, *Welding Metallurgy and Weldability of Stainless Steels*. 2005: Wiley.
4. Siewert, T.A., C.N. McCowan, and D.L. Olson, *Ferrite Number Prediction to 100 FN in Stainless Steel Weld Metal*. *Welding Journal*, 1988. **67**(12): p. 289s-298s.
5. McCowan, C.N., T.A. Siewert, and D.L. Olson, *Stainless Steel Weld Metal: Prediction of Ferrite Content*. *WRC Bulletin 342*, 1989: p. 1-36.
6. Kotecki, D.J. and T.A. Siewert, *WRC-1992 Constitution Diagram for Stainless Steel Weld Metals: A Modification of the WRC-1988 Diagram*. *Welding Journal*, 1992. **71**(5): p. 171-178.
7. Kotecki, D.J., *Ferrite determination in stainless steel welds - Advances since 1974*. *Welding Journal (Miami, Fla)*, 1997. **76**(12): p. 24-s.
8. Lukas, H.L., S.G. Fries, and B. Sundman, *Computational thermodynamics: The Calphad method*. *Computational Thermodynamics: The Calphad Method*. Vol. 9780521868112. 2007. 1-313.
9. Saunders, N. and A.P. Miodownik, *CALPHAD (Calculation of Phase Diagrams): A Comprehensive Guide*. 1998: Elsevier.
10. Hillert, M. and C. Qiu, *A reassessment of the Cr-Fe-Ni system*. *Metallurgical Transactions A*, 1990. **21**(6): p. 1673-1680.
11. Katayama, S., T. Fujimoto, and A. Matsunawa, *Correlation Among Solidification Process, Microstructure, Microsegregation and Solidification Cracking Susceptibility in Stainless Steel Weld Metals*. *Transactions of JWRI*, 1985. **14**(1): p. 123-138.
12. Suutala, N., *Effect Of Solidification Conditions On The Solidification Mode In Austenitic Stainless Steels*. *Metallurgical Transactions A*, 1983. **14**(1): p. 191-197.
13. Elmer, J.W., S.M. Allen, and T.W. Eagar, *Microstructural Development During Solidification of Stainless Steel Alloys*. *Metallurgical Transactions A*, 1989. **20**(10): p. 2117-2131.
14. Brooks, J.A. and A.W. Thompson, *Microstructural Development and Solidification Cracking Susceptibility of Austenitic Stainless Steel Welds*. *International Materials Reviews*, 1991. **36**(1): p. 16-44.

15. David, S.A., J.M. Vitek, and T.L. Hebble, *Effect of Rapid Solidification on Stainless Steel Weld Metal Microstructures and Its Implications on the Schaeffler Diagram*. Welding Journal, 1987. **66**(10): p. 289s-300s.
16. Vitek, J.M., S.A. David, and C.R. Hinman, *Improved Ferrite Number Prediction Model that Accounts for Cooling Rate Effects - Part 2: Model Results*. Welding Journal, 2003. **82**(2): p. 43s-50s.
17. Vitek, J.M., S.A. David, and C.R. Hinman, *Improved Ferrite Number Prediction Model that Accounts for Cooling Rate Effects - Part 1: Model Development*. Welding Journal, 2003. **82**(1): p. 10s-17s.
18. Lippold, J.C., *Solidification Behavior and Cracking Susceptibility of Pulsed-Laser Welds in Austenitic Stainless Steels*. Welding Journal, 1994. **73**(6): p. 129s-139s.
19. Brooks, J.A., A.W. Thompson, and J.C. Williams, *Fundamental Study Of The Beneficial Effects Of Delta Ferrite In Reducing Weld Cracking*. Welding Journal (Miami, Fla), 1984. **63**(3): p. 71-s-83-s.
20. Nagira, T., et al., *In situ observation of solidification crack propagation for type 310S and 316L stainless steels during TIG welding using synchrotron X-ray imaging*. Journal of Materials Science, 2021. **56**(17): p. 10653-10663.
21. Coniglio, N. and C.E. Cross, *Initiation and growth mechanisms for weld solidification cracking*. International Materials Reviews, 2013. **58**(7): p. 375-397.
22. Cross, C.E., *On the origin of weld solidification cracking*, in *Hot Cracking Phenomena in Welds*. 2005. p. 3-18.
23. Kou, S., *Solidification and liquation cracking issues in welding*. JOM, 2003. **55**(6): p. 37-42.
24. Kujanpaa, V.P., *Effects Of Steel Type And Impurities In Solidification Cracking Of Austenitic Stainless Steel Welds*. Metal Construction, 1985. **17**(1): p. 40r-46r.
25. Kujanpaa, V., et al., *Correlation between solidification cracking and microstructure in austenitic and austenitic-ferritic stainless steel welds*. Welding Research International, 1979. **9**(2): p. 55-76.
26. Schaeffler, A.L., *Constitution Diagram for Stainless Steel Weld Metal*. Metal Progress, 1949. **56**(11): p. 680.
27. Lienert, T.J. and J.C. Lippold, *Improved weldability diagram for pulsed laser welded austenitic stainless steels*. Science and Technology of Welding and Joining, 2003. **8**(1): p. 1-9.
28. Jernkontoret, *A Guide to the Solidification of Steels*, 1977.
29. Hammar, O. and U. Svensson, *Influence of Steel Composition on Segregation and Microstructure During Solidification of Austenitic Stainless Steels*. Solidification and Casting of Metals, 1979: p. 401-410.
30. Kujanpaa, V.P. and T.J.I. Moisio. *Effect Of Phosphorus And Sulphur On Solidification Cracking In Austenitic Stainless Steels*. in *Solidification Technology in the Foundry and Cast House*. 1983.
31. Olson, D.L., *Prediction of Austenitic Weld Metal Microstructure and Properties*. Welding Journal, 1985. **64**(10): p. 281s-295s.
32. Bermejo, M.A.V., *Predictive and Measurement Methods for Delta Ferrite Determination in Stainless Steels*. Welding Journal, 2012. **91**(4): p. 113s-121s.

33. Pardoe, I., *Applied regression modeling*. 2020: John Wiley & Sons.
34. Scheil, E., *Bemerkungen zur schichtkristallbildung*. Zeitschrift für Metallkunde, 1942. **34**(3): p. 70-72.
35. DuPont, J.N., *Mathematical modeling of solidification paths in ternary alloys: Limiting cases of solute redistribution*. Metallurgical and Materials Transactions A: Physical Metallurgy and Materials Science, 2006. **37**(6): p. 1937-1947.
36. Chen, Q., et al. *Thermodynamic Calculation and Kinetic Simulation Related to Solidification Process*. in *Modeling of Casting, Welding and Advanced Solidification Processes - XI*. 2006.
37. Kadoi, K. and K. Shinozaki, *Effect of Chemical Composition on Susceptibility to Weld Solidification Cracking in Austenitic Weld Metal*. Metallurgical and Materials Transactions A: Physical Metallurgy and Materials Science, 2017. **48**(12): p. 5860-5869.
38. Ueda, S., et al., *Relationship between Alloy Element and Weld Solidification Cracking Susceptibility of Austenitic Stainless Steel*. ISIJ International, 2019. **59**(7): p. 1323-1329.
39. DuPont, J.N., *Fundamentals of Weld Solidification*, in *ASM Handbook*. 2011, ASM International. p. 96-114.
40. Ogura, T., S. Ichikawa, and K. Saida, *Theoretical Approach to Influence of Nitrogen on Solidification Cracking Susceptibility of Austenitic Stainless Steels: Computer Simulation of Hot Cracking by Solidification/Segregation Models*. Welding International, 2018. **32**(6): p. 436-444.
41. Brody, H.D. and F. M.C., *Solute Redistribution in Dendritic Solidification*. Trans Met Soc AIME, 1966. **236**(5): p. 615-624.
42. Clyne, T.W. and W. Kurz, *Solute Redistribution During Solidification with Rapid Solid State Diffusion*. Metallurgical transactions. A, Physical metallurgy and materials science, 1981. **12 A**(6): p. 965-971.
43. Yamada, W., T. Matsumiya, and B. Sundman, *Development of a Simulator of Solidification Path and Formation of Nonmetallic Inclusions During Solidification of Stainless Steels*. Computer Aided Innovation of New Materials, 1991: p. 587-590.
44. Chen, Q. and B. Sundman, *Computation of Partial Equilibrium Solidification with Complete Interstitial and Negligible Substitutional Solute Back Diffusion*. Materials Transactions, 2002. **43**(3): p. 551-559.
45. Koseki, T., et al., *Numerical Modeling of Solidification and Subsequent Transformation of Fe-Cr-Ni alloys*. Metallurgical and Materials Transactions A, 1994. **25**(6): p. 1309-1321.
46. Crusius, S., et al., *On the Numerical Treatment of Moving Boundary Problems*. Zeitschrift fuer Metallkunde, 1992. **83**(9): p. 673-678.
47. Lee, H.M., et al., *Diffusional Solidification Behavior in 304 Stainless Steel*. Materials Transactions, JIM, 1998. **39**(6): p. 633-639.
48. Hillert, M. and L. Höglund, *Simulation of the Peritectic Reaction in 304 Stainless Steel*. Materials Transactions, JIM, 1999. **40**(6): p. 567-570.

49. Baldissin, D. and L. Battezzati, *Simulation of Diffusional Processes During Solidification in Austenitic Stainless Steels*, in *1st International Conference on Super-High Strength Steels*. 2005, Associazione Italiana di Metallurgia: Rome, Italy.
50. Valiente Bermejo, M.A. and S. Wessman, *Computational Thermodynamics in Ferrite Content Prediction of Austenitic Stainless Steel Weldments*. *Welding in the World*, 2019. **63**(3): p. 627-635.
51. Andersson, J.O., et al., *Thermo-Calc & DICTRA, Computational Tools for Materials Science*. *Calphad: Computer Coupling of Phase Diagrams and Thermochemistry*, 2002. **26**(2): p. 273-312.
52. Porter, D.A. and K.E. Easterling, *Phase Transformations in Metals and Alloys*. 2 ed. 1992: Chapman & Hall.
53. Kou, S., *Welding metallurgy*. 2 ed. 2003: Wiley.
54. David, S.A. and J.M. Vitek, *Correlation between solidification parameters and weld microstructures*. *International Materials Reviews*, 1989. **34**(1): p. 213-245.
55. Tiller, W.A., et al., *The redistribution of solute atoms during the solidification of metals*. *Acta Metallurgica*, 1953. **1**(4): p. 428-437.
56. Mullins, W.W. and R.F. Sekerka, *Morphological Stability of a Particle Growing by Diffusion or Heat Flow*. *Journal of Applied Physics*, 1963. **34**(2): p. 323-329.
57. Kurz, W., *Solidification microstructure-processing maps: Theory and application*. *Advanced Engineering Materials*, 2001. **3**(7): p. 443-452.
58. Kurz, W., *Dendrite Growth in Welding*, in *Mathematical Modelling Of Weld Phenomena 2*, H. Cerjak, Editor. 1995, Institute of Materials: London.
59. Fukumoto, S. and W. Kurz, *Prediction of the δ to γ transition in austenitic stainless steels during laser treatment*. *ISIJ International*, 1998. **38**(1): p. 71-77.
60. Dantzig, J.A. and M. Rappaz, *Solidification*. 2nd ed. 2016: EPFL Press.
61. Fukumoto, S. and W. Kurz, *Solidification phase and microstructure selection maps for Fe-Cr-Ni alloys*. *ISIJ International*, 1999. **39**(12): p. 1270-1279.
62. Fukumoto, S. and W. Kurz, *The δ to γ transition in Fe-Cr-Ni alloys during laser treatment*. *ISIJ International*, 1997. **37**(7): p. 677-684.
63. Bobadilla, M., J. Lacaze, and G. Lesoult, *Influence des conditions de solidification sur le déroulement de la solidification des aciers inoxydables austénitiques*. *Journal of Crystal Growth*, 1988. **89**(4): p. 531-544.
64. Bobadilla, M., J. Lacaze, and G. Lesoult, *Effect of cooling rate on the solidification behaviour of austenitic stainless steels*. *Scandinavian Journal of Metallurgy*, 1996. **25**(1): p. 2-10.
65. Rappaz, M., et al., *Development of microstructures in Fe-15Ni-15Cr single crystal electron beam welds*. *Metallurgical Transactions A*, 1989. **20**(6): p. 1125-1138.
66. Rappaz, M., et al., *Analysis of solidification microstructures in Fe-Ni-Cr single-crystal welds*. *Metallurgical Transactions A*, 1990. **21**(6): p. 1767-1782.
67. Langer, J.S. and H. Müller-Krumbhaar, *Theory of dendritic growth-I. Elements of a stability analysis*. *Acta Metallurgica*, 1978. **26**(11): p. 1681-1687.

68. Kurz, W., B. Giovanola, and R. Trivedi, *Theory of microstructural development during rapid solidification*. Acta Metallurgica, 1986. **34**(5): p. 823-830.
69. Trivedi, R. and W. Kurz, *Dendritic Growth*. International Materials Reviews, 1994. **39**(2): p. 49-74.
70. Hunziker, O., *Theory of plane front and dendritic growth in multicomponent alloys*. Acta Materialia, 2001. **49**(20): p. 4191-4203.
71. Aziz, M.J. and W.J. Boettinger, *On the transition from short-range diffusion-limited to collision-limited growth in alloy solidification*. Acta Metallurgica Et Materialia, 1994. **42**(2): p. 527-537.
72. Aziz, M.J., *Model for solute redistribution during rapid solidification*. Journal of Applied Physics, 1982. **53**(2): p. 1158-1168.
73. Aziz, M.J., *Interface attachment kinetics in alloy solidification*. Metallurgical and Materials Transactions A: Physical Metallurgy and Materials Science, 1996. **27**(3): p. 671-686.
74. Burden, M.H. and J.D. Hunt, *Cellular and Dendritic Growth II*. Journal of Crystal Growth, 1974. **22**(2): p. 109-116.
75. Chen, S.L., et al., *The PANDAT software package and its applications*. Calphad: Computer Coupling of Phase Diagrams and Thermochemistry, 2002. **26**(2): p. 175-188.
76. Ogawa, T. and T. Koseki, *Weldability Of Newly Developed Austenitic Alloys For Cryogenic Service: Part I - High-Nitrogen Stainless Steel Weld Metal*. Welding Journal (Miami, Fla), 1988. **67**(1): p. 8s-17s.
77. Suutala, N., *Effect Of Manganese And Nitrogen On The Solidification Mode In Austenitic Stainless Steel Welds*. Metallurgical transactions. A, Physical metallurgy and materials science, 1982. **13 A**(12): p. 2121-2130.
78. JMP Pro, Version 15.2. SAS Institute Inc., Cary, NC, 1989–2021.
79. Origin, Version 2020b. OriginLab Corporation, Northampton, MA, USA.
80. Valiente Bermejo, M.A., *Influence of the [Creq+Nieq] Alloy Level on the Transition Between Solidification Modes in Austenitic Stainless Steel Weld Metal*. Welding in the World, 2012. **56**(11-12): p. 2-14.
81. Valiente Bermejo, M.A., *A Mathematical Model to Predict δ -Ferrite Content in Austenitic Stainless Steel Weld Metals*. Welding in the World, 2012. **56**(9-10): p. 48-68.
82. Babu, S.S., et al., *Time-resolved X-ray diffraction investigation of primary weld solidification in Fe-C-Al-Mn steel welds*. Acta Materialia, 2002. **50**(19): p. 4763-4781.
83. Brooks, J.A., M.I. Baskes, and F.A. Greulich, *Solidification Modeling And Solid-State Transformations In High-Energy Density Stainless Steel Welds*. Metallurgical Transactions A, 1991. **22**(4): p. 915-926.
84. Kurz, W. and R. Trivedi, *Modern Solidification Theory Applied to Welding*, in *Trends in Welding Research*. 1996: Gatlinburg, TN. p. 115-120.
85. Nakagawa, H., et al., *X-ray Investigations on Solidification Structures in Weld Metal*. Transactions of the Japan Welding Society, 1970. **1**: p. 94-103.

86. Kou, S. and Y. Le, *Effect Of Quenching On The Solidification Structure And Transformation Behavior Of Stainless Steel Welds*. Metallurgical transactions. A, Physical metallurgy and materials science, 1982. **13 A**(7): p. 1141-1152.
87. Lippold, J.C., *Centerline Cracking In Deep Penetration Electron Beam Welds In Type 304L Stainless Steel*. Welding Journal (Miami, Fla), 1985. **64**(5): p. 127. s-136. s.
88. Bhadeshia, H.K.D.H., S.A. David, and J.M. Vitek, *Solidification Sequences In Stainless Steel Dissimilar Alloy Welds*. Materials Science and Technology, 1991. **7**(1): p. 50-61.
89. Tsukamoto, S., H. Harada, and H.K.D.H. Bhadeshia, *Metastable Phase Solidification In Electron Beam Welding Of Dissimilar Stainless Steels*. Materials Science and Engineering A, 1994. **178**(1-2): p. 189-194.
90. SPECTRO, *Application Brief: Analysis of Steel and Cast Iron*.
91. Farrar, J.C.M., *The Measurement Of Ferrite Number (FN) In Real Weldments - Final Report*. Welding in the World, 2005. **49**(5-6): p. 13-21.
92. ASTM E1019-18, Standard Test Methods for Determination of Carbon, Sulfur, Nitrogen, and Oxygen in Steel, Iron, Nickel, and Cobalt Alloys by Various Combustion and Inert Gas Fusion Techniques, ASTM International, West Conshohocken, PA, 2018, www.astm.org.
93. ASTM E1086-14, Standard Test Method for Analysis of Austenitic Stainless Steel by Spark Atomic Emission Spectrometry, ASTM International, West Conshohocken, PA, 2014, www.astm.org.
94. Kotecki, D.J. and Z. Zhang, *Sources Of Variation In Ferrite Number Predictions Vs. Measurements*. Welding Journal, 2013. **92**(6): p. 175S-181S.
95. Katayama, S. and A. Matsunawa, *Solidification Microstructure of Laser Welded Stainless Steels*. International Congress on Applications of Lasers & Electro-Optics, 1984. **1984**(2): p. 60-67.
96. Zhang, W., et al., *Modeling Of Heat Transfer And Fluid Flow During Gas Tungsten Arc Spot Welding Of Low Carbon Steel*. Journal of Applied Physics, 2003. **93**(5): p. 3022-3033.
97. Kurz, W. and D.J. Fisher, *Fundamentals of Solidification*. 1992, Aedermannsdorf, Switzerland; Brookfield, Vt.: Trans Tech Publications.
98. Kurz, W., C. Bezençon, and M. Gäumann, *Columnar To Equiaxed Transition In Solidification Processing*. Science and Technology of Advanced Materials, 2001. **2**(1): p. 185-191.
99. Hunt, J.D., *Steady State Columnar And Equiaxed Growth Of Dendrites And Eutectic*. Materials Science and Engineering, 1984. **65**(1): p. 75-83.
100. Lippold, J.C., *Welding Metallurgy and Weldability*. 2014: Wiley.
101. Lin, Y., et al., *CALPHAD Uncertainty Quantification and TDBX*. JOM, 2021. **73**(1): p. 116-125.
102. Honarmandi, P. and R. Arróyave, *Uncertainty Quantification and Propagation in Computational Materials Science and Simulation-Assisted Materials Design*. Integrating Materials and Manufacturing Innovation, 2020. **9**(1): p. 103-143.

103. Schmid-Fetzer, R. and A. Kozlov, *Thermodynamic Aspects Of Grain Growth Restriction In Multicomponent Alloy Solidification*. Acta Materialia, 2011. **59**(15): p. 6133-6144.

Appendix A. Certified Material Test Reports for Stainless Steel Filler Materials

SS-1224

Inspection Certificate 3.1



METRODE
WELDING CONSUMABLES
A Lincoln Electric Company

Product 308S92 TIG
Size(s) mm 2.4 * 1000
Item No. T308S92-24
Lot/Batch V10528
Product Line TIG Wire
Class AWS A5.9/A5.9M : ER308L
 ISO 14343-A : W 19 9 L

Chemical analysis (%) According to EN10204 3.1

C	Si	Mn	P	S	Cr	Ni	Mo	Cu
0.018	0.40	1.72	0.026	0.012	19.8	9.1	0.03	0.06

Mechanical tests, all weld metal According to EN10204 3.1

Tensile testing							Impact testing	
Cond.	Temp. °C	Rp0.2 MPa	Rm MPa	A4 %	A5 %	Z %	Temp. °C	KV J
AW	23	368	570	49	44	73	-70	123

Ferrite According to EN10204 3.1

FN WRC92
11

Remarks

The product identified above has been manufactured, tested and supplied in compliance with a certified ISO 9001 Quality Assurance Programme.

Company Metrode Products Ltd Hanworth Lane KT16 9LL, Chertsey, Surrey United Kingdom		Printed By Diana Cole Function Customer Care Manager Date 27/OCT/2017	Cert. No. 00437527 <small>ZSL/STANBES.1</small>
---	---	--	---

Figure 53: ER308L material test report

Jun 3, 2003
9:21:31

KAM
Page 1 of 1
No. 200319758

M A T E R I A L C E R T I F I C A T E

Sandvik Materials Technology
P.O. Box 1220, Scranton, PA 18501 PH. (570) 585-7500
Plant Location: 982 Griffin Pond Road, Clarks Summit, PA 18411

Sold To:
WELDERS SUPPLY OF CHARLOTTE
CHARLOTTE NC
Customer Order No: 06588-1
Sandvik Order No: 93884/1
Work Order/Lot: 751190

Ship To:
EPRI NDE CENTER
CHARLOTTE NC
Certification Date: 20030603

AWS A5.9-93, ASME SFA 5.9, ASME Section II, 2001 EDITION, 2002 Addenda

Stainless Steel Welding Wire
Type ER308Si/ER308LSi

Size: .045" X 10 LB. SPOOL
Heat: 457753

Analysis %							
Heat	C	Si	Mn	P	S	Cr	Ni
	.024	.79	2.01	.028	.012	19.87	9.05
	Mo	Cu	*FD	*FS	*FW		
	.40	.19	12	14	11		

*FD = Delta Ferrite (FN) from the DeLong Diagram
*FS = Delta Ferrite (%) from the Schaeffler Diagram
*FW = Delta Ferrite (FN) from ASME Fig. NB 2433.1-1 (WRC 1992 Diagram)

Country Of Origin: United States

The following mechanical test results are typical values representative of this grade of material.

Tensile (psi): 85000

Elongation % : 45

ABS (American Bureau of Shipping) approval has been attained by Sandvik Materials Technology for the following steel grades: ER308, ER308L, ER309, ER309Si, ER309L, ER316L, ER347 CWB (Canadian Welding Bureau) approval has been attained by Sandvik for the following steel grades: ER308L, ER308LSi, ER309L, ER309LSi, ER316L, ER316LSi, ER317L, ER347. Material has been manufactured in accordance with Sandvik Sandvik Materials Technology Quality Manual Revision 5 dated February 6, 2003.

Quality system approved to ISO-9002/ANSI/ASQC Q9002-1994.
Certificate produced in accordance with EN 10204 (DIN 50049) 3.1.B.

The material has not come in contact with mercury or mercury containing compounds and as such is certified mercury free. This is to certify that the contents of this certificate are correct and accurate as contained in Sandvik's records, and that all above test results and operations performed are in compliance with the requirements of the purchase order.

Electronically Generated Certificate-Valid without signature
10 (A5.9 STD VARSPL R10) (15) (KAM)

Figure 54: ER308LSi material test report

Oct 25 07 11:19a
10/25/2007 11:34

Praxair Charlotte
7045986673

7043959876
WASHINGTON ALLOY

P. 2



WASHINGTON ALLOY CO.
A Division of U.S. Alloy Co.

P.O. Box 73909 Puyallup, WA 98373
mail2@washingtonalloy.com
www.weldingwire.com

MATERIAL TEST REPORT

Customer: GENEX/PRAAIR P.O. BOX 9224 DES MOINES IA 50306-9224 US	PO: 10/25 Ship Date: Net Weight:
--	---

Product: ER309L
Dimensions: .035" X 2 LB
Heat #: 7070597309
Specification: AWS A5.9 ER309L 10/04/07 NC 4

C .01	Cr 23	Cu .1	Fe BAL	Mn 1.6	Mo .07	Ni 13.7
P .02	S .001	Si .47				

QUALITY APPROVED
INSPECTOR #4
DATE OCT 25 2007
Washington Alloy
Charlotte, NC 28216-USA

*This certification is provided by Washington Alloy Co. with the expressed understanding that if the product supplied fails
the undersigned and the obligation*

Figure 55: ER309L material test report

**Certified Material Test Report
For Blue Max Electrode**

The Lincoln Electric Company
22801 St. Clair Avenue
Cleveland, Ohio 44117-1199

This is to certify that the following material was all manufactured under one lot control number (Class S3 per AWS A5.01).

The "045" Blue Max MIG 309LSi electrode, Q2 Lot 726F was tested for composition according to the requirements of AWS A5.9 and ASME SFA-5.9. Results obtained are as follows:

%C	ER309Si	ER309LSi	Actual Average Lot Results
	Requirements	Requirements	
Cr	0.12 max 23.0-25.0	0.03 max 23.0-25.0	.02 23.8
Ni	12.0-14.0	12.0-14.0	12.7
Mn	0.75 max	0.75 max	.14
Mo	1.0-2.5	1.0-2.5	2.1
Si	0.65-1.00	0.65-1.00	.86
P	0.03 max	0.03 max	.02
S	0.03 max	0.03 max	.02
N	Not Specified*	Not Specified*	.09
Cu	0.75 max	0.75 max	.06
Nb/Cb	Not Specified*	Not Specified*	.06
Calculated Ferrite Number (from actual composition)	WRC-1992 Not Specified	WRC-1992 Not Specified	13.2
	WRC-Delong Not Specified	WRC-Delong Not Specified	15.9

* Excluded in 0.50% maximum other elements.

We do not use mercury in the design and formulation of our consumable products. In the manufacturing and testing of our products, our equipment meets mercury exclusion requirements. All material in one carton is from one Lot.

Daniaman Koticki
Technical Director for Stainless and High Alloy Product Development
Date: 2004-11-30
Dr. Daniaman Koticki

James T. Hyall
Manager, Special Products, James T. Hyall
Date: 5 DEC 04

Ed Linky
Manager, Quality Assurance, Ed Linky
Date: 12/3/04

*Note: The reprinting of this, revision or fraudulent statements or entries on this document may be punished as a felony under Federal Statutes including Federal Law, Title 18, Chapter 47.

2004 11 24 04

Figure 56: ER309LSi material test report



www.smt.sandvik.com
www.smt.sandvik.com/nalta

Sandvik Materials Technology
Wire & Heating Technology

Scranton
PA USA 18501
670-585-7500

MATERIAL CERTIFICATE

Cert#: 201100094

Page 1
US36504

Plant Location: 982 Griffin Pond Road, Clarks Summit, PA 18411
 Sold To: 498811 Ship To:
 PRAXAIR-CENTRAL-Des Moines PRAXAIR-Charlotte
 DES MOINES IA CHARLOTTE NC
 Customer Order No: 3196004 Certification Date: 20110103
 Sandvik Order No: 27080/9
 Work Order/Lot: 838599

 AWS A5.9-06, ASME SFA 5.9, 2010 EDITION, NO ADDENDA, EN 10204.3.1.B

Stainless Steel Welding Wire

Type ER316/ER316L

Size: .125" X 36"

Heat: 525611

Analysis %							
Heat	C	Si	Mn	P	S	Cr	Ni
	.012	.38	1.68	.021	.012	18.56	12.15
	Fe	Mo	Co	Cu	Al	Sn	Ta
		2.51	.055	.18	.007		.005
	N	*FD	*FS	*FW			
	.031	10	7	9			

- *FD = Delta Ferrite (FN) from the DeLong Diagram
- *FS = Delta Ferrite (%) from the Schaeffler Diagram
- *FW = Delta Ferrite (FN) from ASME Fig. NB 2433.1-1 (WRC 1992 Diagram)

Country Of Origin: United States

The following mechanical test results are typical values representative of this grade of material.

Tensile (psi): 90000

Elongation % : 40

The Heat analysis is an actual Chemistry Analysis.

CWB (Canadian Welding Bureau) approval has been attained

by Sandvik for the following steel grades: ER308L, ER308LSi, ER309L, ER309LSi, ER316L, ER316LSi, ER317L, ER347.

The material has not come in contact with mercury or mercury containing compounds and as such is certified mercury free.

Material has been manufactured in accordance with Sandvik

Sandvik Materials Technology Quality Manual Revision 11

dated November 09, 2009

Quality system approved to ISO 9001:2008.

Certificate produced in accordance with EN 10204 3.1

(Formerly EN 10204 3.1.B)

This is to certify that the contents of this certificate are correct and accurate as contained in Sandvik's records, and that all above test results and operations performed are in compliance with the requirements of the purchase order.

Electronically Generated Certificate-Valid without signature

Figure 57: ER316L material test report



WASHINGTON ALLOY CO.

A Division of U.S. Alloy Co.

7010-G Reames Road Charlotte, NC 28216

mail2@washingtonalloy.com
www.washingtonalloy.com

MATERIAL TEST REPORT

PRODUCT: ER316LSi
SPECIFICATION: AWS A5.9 ER316LSi 9/26/06 NC 1
DIMENSIONS: .023" .045"
HEAT #: DEED447

Actual chemical Analysis

C .012	Cr 18.6	Cu .14	Fe BAL	Mn 1.53	Mo 2.64	N .038
Ni 11.59	P .024	S .002	Si .91			

Typical Mechanical Properties

Tensile Strength	88,000 PSI (MIN)	Elongation	37% (MIN)
Yield Strength	58,000 PSI (MIN)	Charpy Impact	

Remarks:

This certification is provided by Washington Alloy Co. with the expressed understanding that if the product supplied fails to conform the stated specifications, there shall be no personal liability of any kind on the undersigned and the obligation and liability of Washington Alloy Co., with respect to such non-conformance or specification failure, shall be limited to

- a) an obligation to furnish the purchaser, at no additional charge, material that meets the specifications and conformances or*
- b) to refund to the purchaser the full amount of money paid to Washington Alloy Co. for the return of the product in full.*

In no event shall Washington Alloy Co. be liable for consequential damage.

Certification Administrator

Figure 58: ER316LSi material test report



WASHINGTON ALLOY CO.
 A Division of U.S. Alloy Co.
 7010-G REAMES ROAD CHARLOTTE, NC 28216
 mail2@washingtonalloy.com
 www.washingtonalloy.com

Material Test Report

MTR # : 16760

Page : 1 of 1

SOLD TO:

SHIP TO:

DATE	SALES ORDER #	CUST P.O.#	CLASSIFICATION	SPECIFICATION	
05/16/2019			ER330	ER330 AWS A5.9-2012	
LINE #	QTY	ITEM #	ITEM DESCRIPTION	HEAT NO.	LOT NO.
			.035	135938	17C04031

CHEMICAL ANALYSIS

C	Cr	Cu	Mn	Mo	Ni	P	S	Si	N
0.2050	16.0400	0.0300	1.4700	0.0400	34.5700	0.0150	<0.0010	0.5900	0.0215

PHYSICAL PROPERTIES

TENSILE STRENGTH	ELONG.
573000	33

SUPPLEMENTAL INFORMATION

ACCORDANCE WITH EN10204 3.1 (CHEMISTRY ONLY)
 MATERIAL IS FREE OF MERCURY CONTAMINATION
 MC. A1

Certification Administrator

Certification and Limited Warranty - This certifies that the product supplied will meet the requirements of the noted classification and data above. Products supplied in accordance to the Quality Management System of Washington Alloy Company. Results may vary from other particular testing or specific batches, heats or lots.

Figure 59: ER330 material test report

Appendix B. Chemical Analysis Results for Experimental Ingots

Series	Sample	Cr (wt.%)		Mo (wt.%)		Si (wt.%)		Mn (wt.%)		Ni (wt.%)		C (wt.%)		N (wt.%) [†]		Cu (wt.%)		WRC-1992		ΔT_{L2}		Solidification Mode
		Conc.	SD	Conc.	SD	Conc.	SD	Conc.	SD	Conc.	SD	Conc.	SD	Conc.	SD	Conc.	SD	Cr _{eq}	Ni _{eq}	Cr _{eq}	Ni _{eq}	
ER308L + ER330	8L30A1	19.24	0.041	0.028	0.0004	0.36	0.004	1.58	0.011	12.63	0.021	0.037	0.0001	0.056	0.0006	0.08	0.005	19.27	15.07	18.85	15.15	A
	8L30F2	19.36	0.041	0.027	0.0002	0.35	0.003	1.59	0.004	12.25	0.045	0.036	0.0007	0.053	0.0010	0.10	0.010	19.39	14.60	19.10	14.60	A
	8L30F5	19.42	0.030	0.027	0.0002	0.35	0.003	1.60	0.005	11.94	0.018	0.034	0.0005	0.056	0.0020	0.09	0.011	19.45	14.27	19.23	14.20	A
	8L30F10	19.61	0.006	0.026	0.0002	0.34	0.002	1.59	0.005	11.21	0.063	0.032	0.0007	0.055	0.0020	0.14	0.015	19.64	13.47	19.64	13.27	A (F)*
	8L30F13	19.27	0.038	0.026	0.0001	0.38	0.002	1.56	0.013	10.77	0.036	0.021	0.0015	0.055	0.0020	0.07	0.003	19.30	12.61	18.92	12.42	F
ER308LSi + ER330	8LSi30A1	19.51	0.020	0.37	0.003	0.63	0.003	1.98	0.008	12.52	0.023	0.050	0.0020	0.069	0.0040	0.20	0.018	19.88	15.70	20.68	15.64	A
	8LSi30F2	19.59	0.051	0.37	0.004	0.61	0.008	1.98	0.002	12.23	0.031	0.045	0.0010	0.067	0.0009	0.31	0.070	19.96	15.22	20.84	15.30	A
	8LSi30F5	19.58	0.026	0.38	0.001	0.64	0.005	1.99	0.016	11.96	0.059	0.041	0.0004	0.067	0.0050	0.22	0.026	19.96	14.79	20.88	14.74	A
	8LSi30F10	19.65	0.004	0.39	0.001	0.63	0.002	2.01	0.014	11.27	0.047	0.037	0.0010	0.074	0.0010	0.32	0.099	20.04	14.13	21.05	14.06	A / F**
	8LSi30F13	19.45	0.013	0.40	0.002	0.66	0.005	1.98	0.006	10.78	0.040	0.029	0.0011	0.070	0.0020	0.19	0.019	19.85	13.23	20.66	13.03	F
ER309L + ER330	9L30A1	22.12	0.036	0.13	0.001	0.41	0.004	1.66	0.006	15.69	0.010	0.030	0.0020	0.046	0.0003	0.12	0.002	22.25	17.69	25.96	19.27	A
	9L30F2	22.39	0.031	0.13	0.001	0.41	0.003	1.65	0.003	15.24	0.041	0.026	0.0005	0.048	0.0008	0.13	0.025	22.52	17.14	26.64	18.59	A
	9L30F5	22.37	0.020	0.13	0.001	0.41	0.002	1.66	0.005	14.96	0.051	0.027	0.0010	0.042	0.0005	0.12	0.017	22.50	16.78	26.59	18.07	A
	9L30F10	22.72	0.031	0.13	0.001	0.40	0.004	1.65	0.005	14.36	0.011	0.022	0.0030	0.053	0.0009	0.17	0.029	22.85	16.23	27.49	17.40	A (F)*
	9L30F13	22.70	0.045	0.13	0.001	0.42	0.004	1.62	0.009	13.78	0.058	0.017	0.0011	0.045	0.0020	0.12	0.039	22.83	15.29	27.44	16.27	F
ER309LSi + ER330	9LSi30A1	22.56	0.046	0.18	0.001	0.69	0.001	2.15	0.013	15.29	0.034	0.037	0.0008	0.073	0.0005	0.12	0.003	22.74	18.08	27.50	19.29	A
	9LSi30F2	22.70	0.024	0.18	0.001	0.69	0.003	2.17	0.010	14.90	0.056	0.032	0.0004	0.075	0.0020	0.07	0.011	22.88	17.54	27.87	18.60	A
	9LSi30F5	22.83	0.033	0.18	0.001	0.69	0.005	2.16	0.011	14.53	0.056	0.033	0.0010	0.061	0.0004	0.13	0.024	23.01	16.94	28.20	17.91	A
	9LSi30F10	23.01	0.033	0.19	0.001	0.69	0.008	2.17	0.012	14.11	0.070	0.021	0.0006	0.096	0.0020	0.13	0.066	23.20	16.80	28.71	17.76	A (F)*
	9LSi30F13	22.89	0.056	0.19	0.001	0.73	0.006	2.17	0.008	13.54	0.049	0.023	0.0025	0.070	0.0020	0.05	0.001	23.08	15.77	28.43	16.39	F
ER316L + ER330	16L30A1	18.17	0.031	2.39	0.012	0.33	0.004	1.68	0.008	14.23	0.036	0.023	0.0010	0.098	0.0010	0.21	0.011	20.56	17.05	23.43	18.12	A
	16L30F2	18.40	0.033	2.44	0.011	0.34	0.005	1.75	0.003	13.82	0.047	0.032	0.0007	0.037	0.0007	0.24	0.110	20.84	15.74	24.06	16.61	A
	16L30F5	18.35	0.013	2.49	0.010	0.34	0.002	1.73	0.007	13.43	0.015	0.027	0.0010	0.047	0.0006	0.22	0.021	20.84	15.37	24.10	16.14	A
	16L30F10	18.51	0.035	2.55	0.015	0.34	0.004	1.75	0.006	12.84	0.047	0.024	0.0001	0.041	0.0004	0.20	0.017	21.06	14.55	24.60	15.13	A / F**
	16L30F13	18.30	0.023	2.56	0.010	0.35	0.003	1.73	0.010	12.39	0.058	0.019	0.0008	0.045	0.0020	0.21	0.032	20.87	14.00	24.22	14.54	F
ER316LSi + ER330	16LSi30A1	18.19	0.053	2.42	0.014	0.74	0.006	1.58	0.006	14.22	0.028	0.037	0.0050	0.036	0.0008	0.23	0.036	20.61	16.29	23.87	17.22	A
	16LSi30F2	18.28	0.012	2.47	0.013	0.75	0.007	1.58	0.004	13.76	0.058	0.030	0.0003	0.039	0.0020	0.15	0.019	20.75	15.63	24.20	16.39	A
	16LSi30F5	18.27	0.033	2.53	0.007	0.77	0.001	1.57	0.003	13.48	0.031	0.025	0.0006	0.048	0.0010	0.16	0.007	20.80	15.36	24.37	16.10	A
	16LSi30F10	18.34	0.012	2.60	0.002	0.76	0.005	1.57	0.010	12.88	0.032	0.026	0.0007	0.036	0.0009	0.18	0.030	20.94	14.56	24.71	15.10	F

* Mixed mode solidification: predominant mode (minor mode)

** Mixed mode solidification: approximately 50/50 balance between primary modes

† Data for XXXF13 samples is estimated due to abnormally high N readings

Appendix C. Micrographs of Experimental Alloys

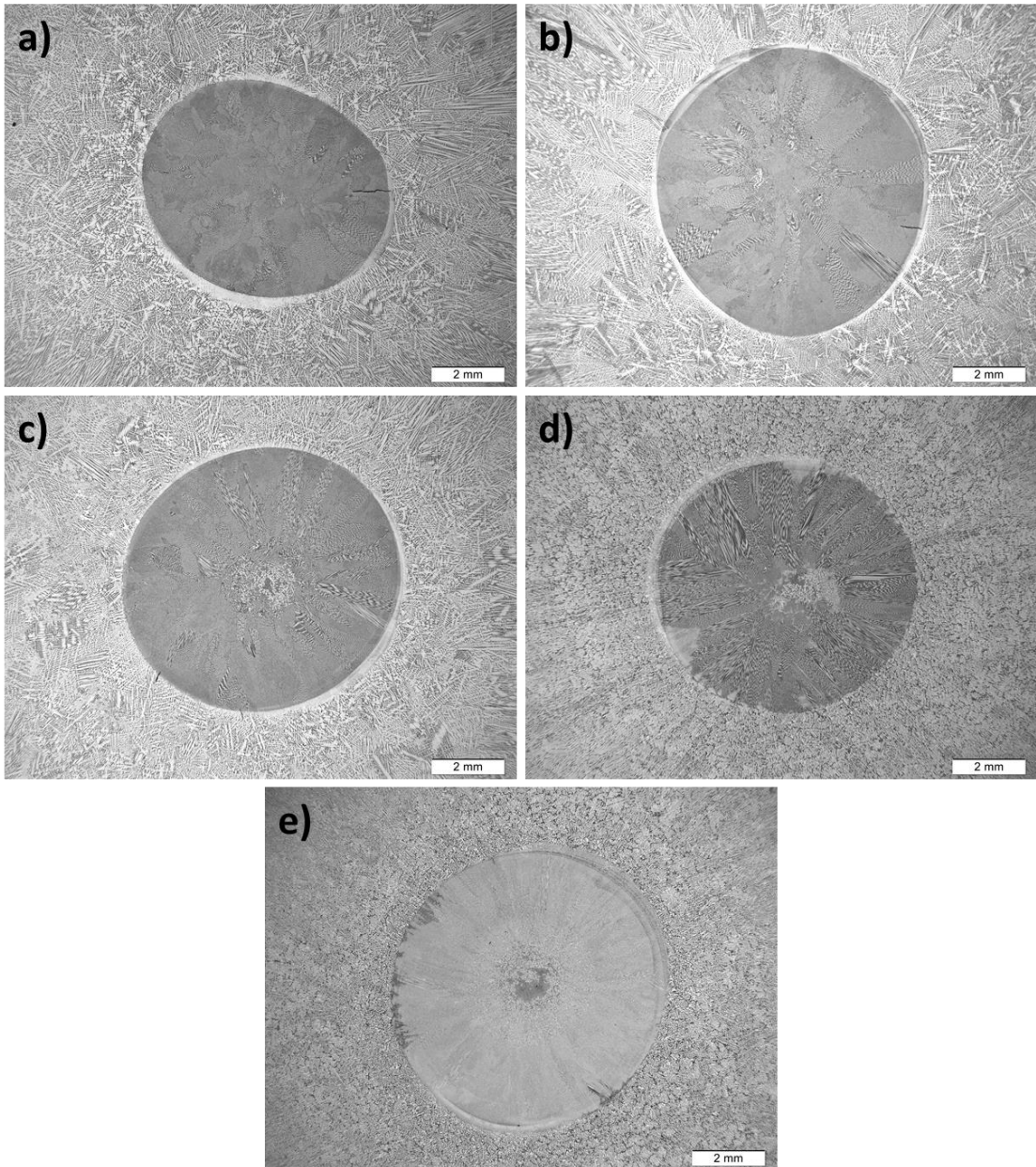


Figure 60:ER308L-ER330 alloys: a) 8L30A1; b) 8L30F2; c) 8L30F5; d) 8L30F10; e)
8L30F13

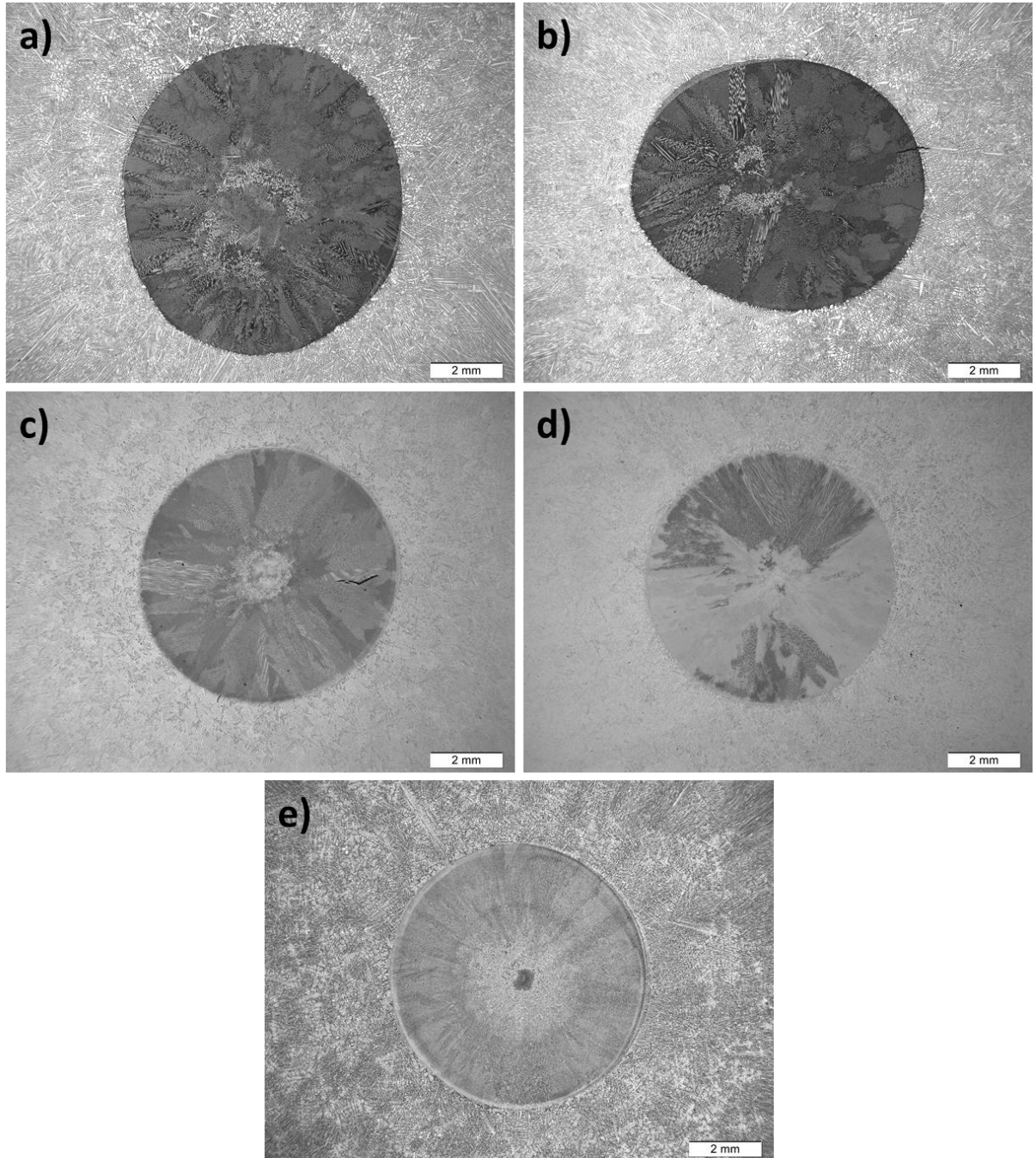


Figure 61: ER308LSi-ER330 alloys: a) 8LSi30A1; b) 8LSi30F2; c) 8LSi30F5; d) 8LSi30F10; e) 8LSi30F13

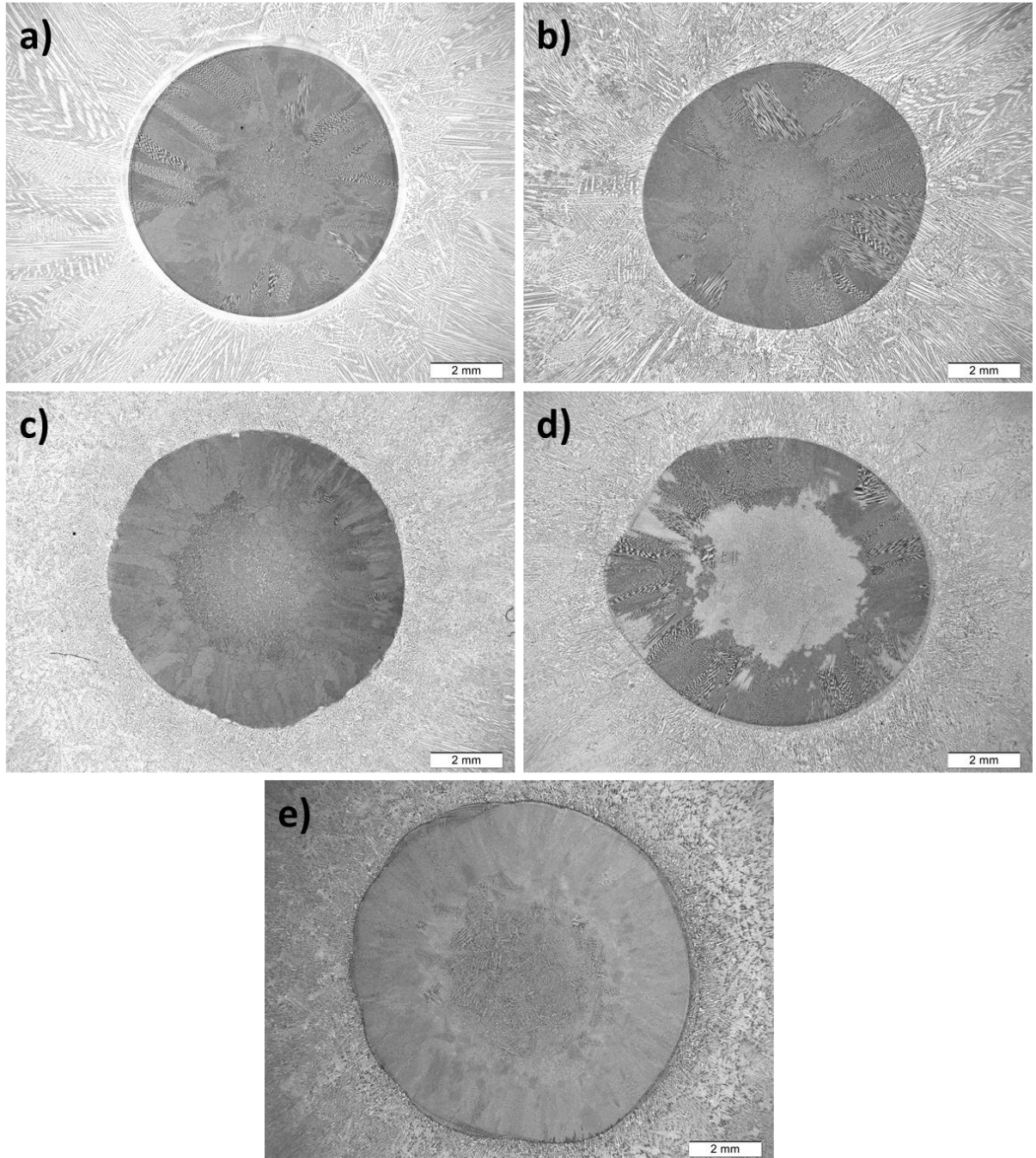


Figure 62: ER309L-ER330 alloys: a) 9L30A1; b) 9L30F2; c) 9L30F5; d) 9L30F10; e) 9L30F13

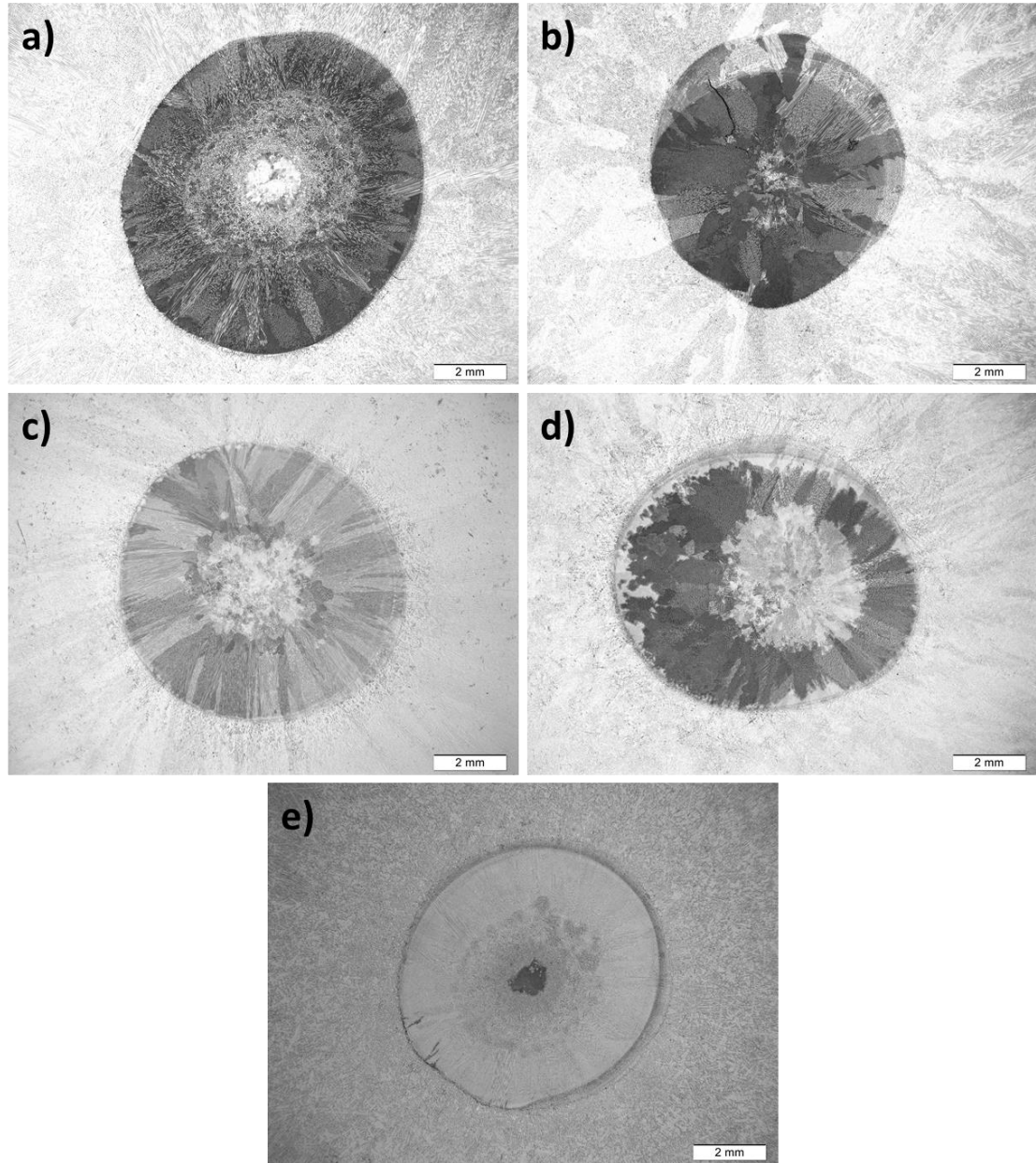


Figure 63: ER309LSi-ER330 alloys: a) 9LSi30A1; b) 9LSi30F2; c) 9LSi30F5; d) 9LSi30F10; e) 9LSi30F13

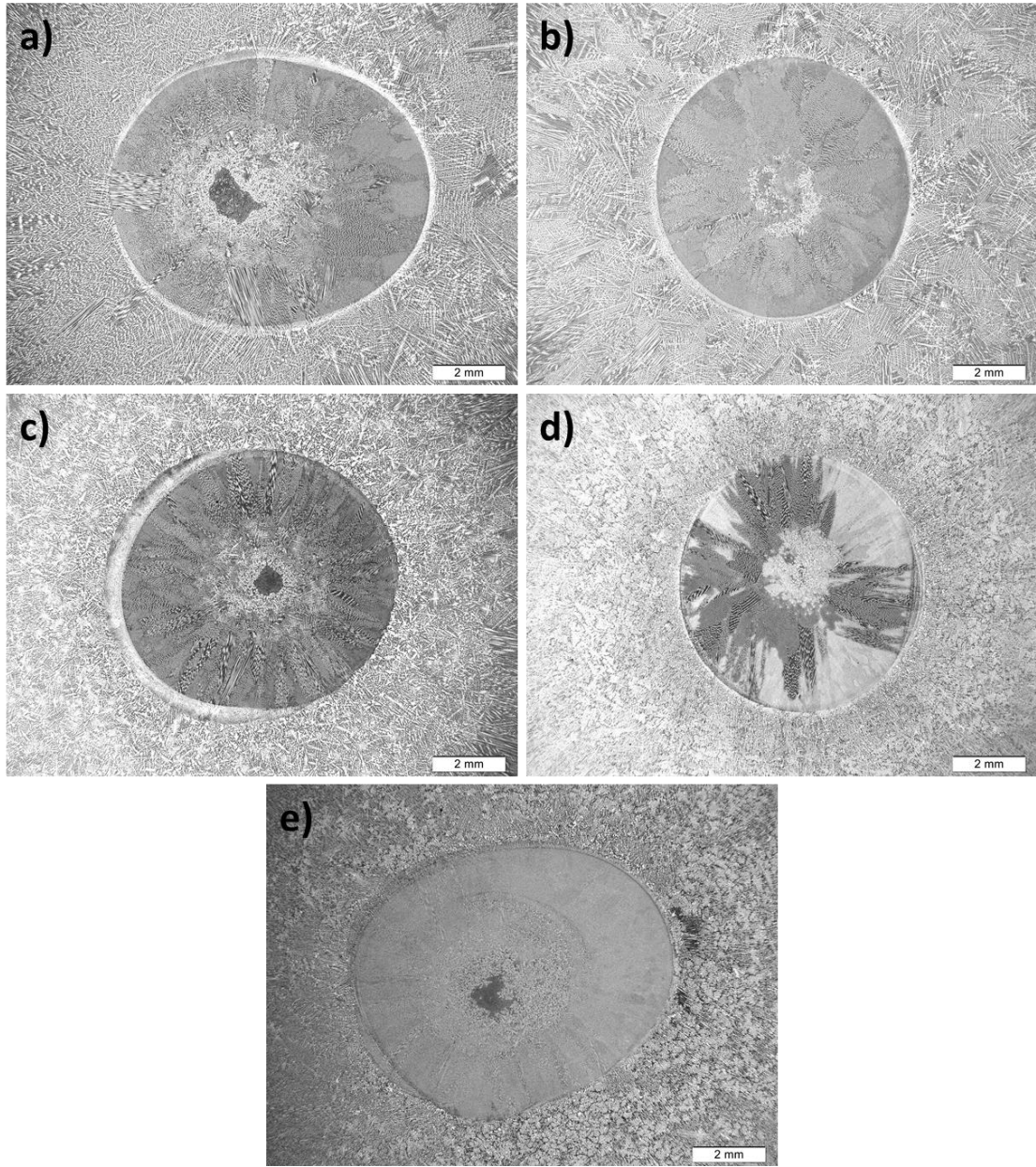


Figure 64: ER316L-ER330 alloys: a) 16L30A1; b) 16L30F2; c) 16L30F5; d) 16L30F10; e) 16L30F13

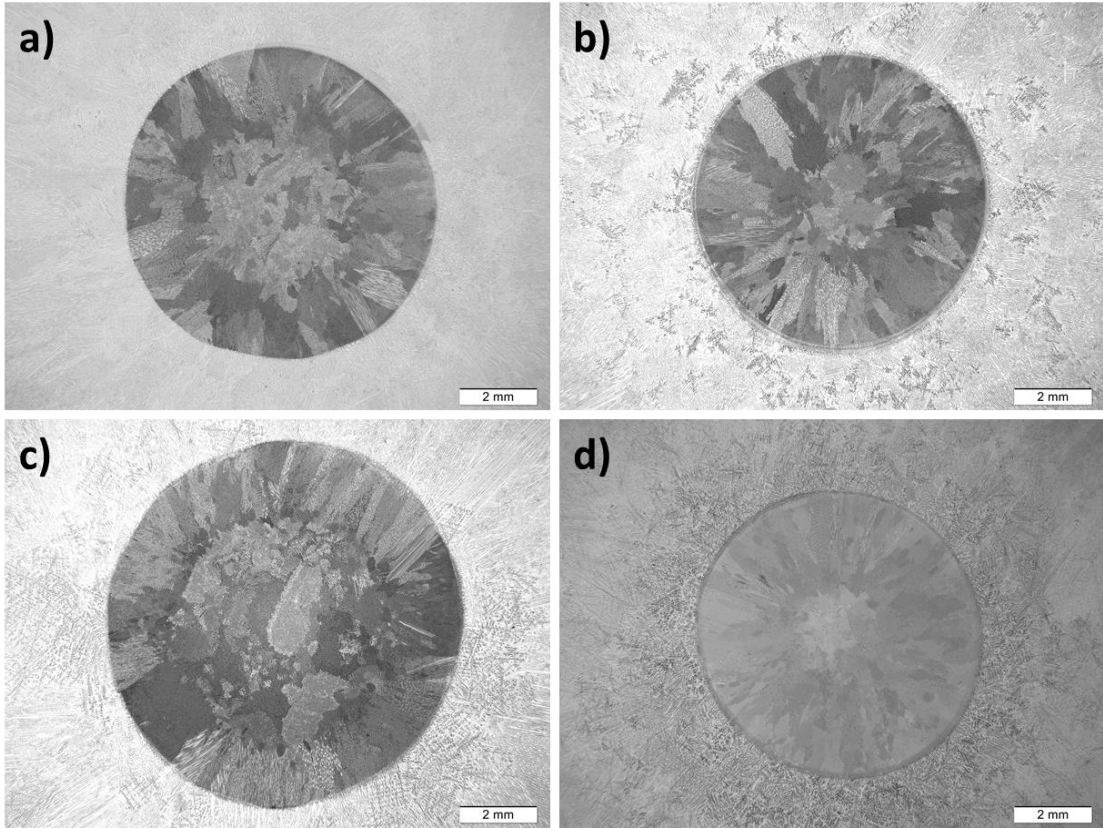


Figure 65: ER316LSi-ER330 alloys: a) 16LSi30A1; b) 16LSi30F2; c) 16LSi30F5; d) 16LSi30F10